WILEY

Modeling curved interfaces without element-partitioning in the extended finite element method

Eric B. Chin [ID] | **N. Sukumar** [ID]

Department of Civil and Environmental Engineering, University of California, Davis, Davis, California

Correspondence
N. Sukumar, Department of Civil and Environmental Engineering, University of California, One Shields Avenue, Davis, CA 95616.
Email: nsukumar@ucdavis.edu

Summary

In this paper, we model holes and material interfaces (weak discontinuities) in two-dimensional linear elastic continua using the extended finite element method on higher-order (spectral) finite element meshes. Arbitrary parametric curves such as rational Bézier curves and cubic Hermite curves are adopted in conjunction with the level set method to represent curved interfaces. Efficient computation of weak form integrals with polynomial integrands is realized via the homogeneous numerical integration scheme—a method that uses Euler's homogeneous function theorem and Stokes' theorem to reduce integration to the boundary of the domain. Numerical integration on cut elements requires the evaluation of a one-dimensional integral over a parametric curve, and hence, the need to partition curved elements is eliminated. To improve stiffness matrix conditioning, ghost penalty stabilization and the Jacobi preconditioner are used. For material interface problems, we develop an enrichment function that captures weak discontinuities on spectral meshes. Taken together, we show through numerical experiments that these advances deliver optimal algebraic rates of convergence with h-refinement ($p = 1, 2, \ldots, 5$) and exponential rates of convergence with p-refinement ($p = 1, 2, \ldots, 7$) for elastostatic problems with holes and material inclusions on Cartesian pth-order spectral finite element meshes.

KEYWORDS

Bézier curves, homogeneous numerical integration method, interface stabilization, level set methods, material interface enrichment, spectral X-FEM

1 | INTRODUCTION

In the finite element (FE) method, meshes must conform to the geometric features of a domain of interest. These geometric features may include voids (holes) in the domain or a material interface (weak discontinuity) that separates two dissimilar elastic materials. Aligning these geometric features with the mesh requires advanced mesh generation tools, and further, higher-order FEs must accurately represent curved features to recover optimal rates of convergence in the FE method. The extended finite element method (X-FEM)[1,2] is a promising approach for decoupling geometry from the FE mesh. Originally conceived as a method to model cracks in a domain without explicitly meshing the cracks,[1] Sukumar et al[3] combined local enrichment in the X-FEM with the level set method[4] to simplify implicit modeling of closed interfaces (holes and bimaterials) in solid mechanics problems. Legay et al[5] applied the X-FEM to higher-order

(spectral) FE meshes to solve hole and material interface problems, revealing new challenges with respect to interface representation, choice of enrichment, and numerical integration. In this paper, we introduce significant improvements to all three of these long-standing issues.

For a material interface that admits a weak (strain) discontinuity normal to the interface, the X-FEM utilizes the partition-of-unity (PU) framework[6] to enrich the displacement approximation in the vicinity of the interface. Between enriched domains and unenriched domains is a transition zone that contains partially enriched (blending) elements. In these blending elements, the product of the enrichment function and the FE basis functions causes higher-order terms in the approximation to be present that cannot be compensated, thereby reducing the rate of convergence of the method.[7] Issues in blending elements with pth-order FEs arise when the extended FE approximation is not able to reproduce a piecewise-continuous pth degree polynomial on both sides of the interface. Initially, modeling material interfaces using the distance function (abs-enrichment) as the enrichment led to presence of blending elements and suboptimal convergence rates.[3] Many remedies in the blending region have been proposed, such as an enhanced strain formulation[7] and the corrected X-FEM.[8] In addition, reducing the polynomial degree of the PU functions has been shown to improve the rate of convergence of the approximation for elements with polynomial degree greater than one.[5,9] However, a simpler approach is to entirely eliminate the presence of blending elements by designing an enrichment function for material interface problems that vanishes in blending elements. This was achieved by Moës et al[10] who demonstrated optimal convergence rates on low-order (bilinear) FE meshes using a modified abs-enrichment (coined as a ridge or hat enrichment) and, more recently, by Soghrati et al,[11,12] wherein a conforming submesh of the cut elements is used to generate the enrichment function.

Another challenge in modeling holes and material interfaces using the X-FEM is the recovery of optimal rates of convergence on higher-order FE meshes. Finite elements with increasing polynomial degree on a fixed mesh (p-refinement) deliver exponential rates of convergence, thereby providing a more accurate solution per degree of freedom (DOF) than realized via mesh refinement (h-refinement). One complicating factor in the implementation of p-refinement is developing a method to reconstruct the location of the interface. Interface reconstruction must be sufficiently accurate to provide optimal rates of convergence and, furthermore, must be robust enough to handle arbitrary interfaces. A popular approach to accomplish this task has been to subdivide elements that are traversed by the interface with higher-order elements whose boundaries are aligned with the interface.[5,9,12] This separates the element domain into subregions on either side of the interface, where the FE approximation is continuous. However, for complicated interface geometries, this approach can be difficult, requiring special considerations for cases with sharp features (eg, corners) on the interface, regions of high curvature on the interface, or the interface entering and exiting an element multiple times. Another issue with pth-order FEs, specific to the material interface problem, is the construction of a suitable enrichment function so that the approximate solution yields the optimal $p + 1$ rate of convergence in the L^2 norm. Cheng and Fries[9] showed that the distance function paired with corrected X-FEM recovers near optimal rates of convergence, but this requires additional DOFs compared to a standard extended FE approach. Close to the optimal rate of 2 in H^1 seminorm for $p = 2$ has been demonstrated by Dréau et al,[13] where local refinement of the enrichment function from Moës et al[10] is used to improve the representation of curved interfaces; however, this method needs the generation of a submesh of the cut elements. In this paper, we adapt the modified abs-enrichment introduced in Moës et al[10] to capture weak discontinuities on higher-order spectral FE meshes.

Computational methods that consider embedded interfaces with Dirichlet or Neumann constraints on them have also been a very active area of research. Typically, these constraints are enforced using either stable Lagrange multipliers, a penalty approach, or Nitsche's method. Another feature of these methods is the use of higher-order elements in the approximation, either through spectral FEs[14] or spline-based methods. There are many approaches that fall within this category—cut finite elements,[15-17] finite cell method,[18-20] immersed boundary method,[21,22] fictitious domain method,[23,24] embedded interface method,[25-27] and also the X-FEM.[28,29] For simplicity, in the remainder of this paper, these methods will be collectively referred to as embedded interface methods. Other methods for handling voids and material interface problems are conformal decomposition methods,[30-34] which use element subdivisions to construct fitted elements to a background mesh, and discontinuous Galerkin approaches.[35,36]

In embedded interface methods, a significant challenge that remains in the modeling of holes or material inclusions is accurate numerical integration.[37] The need is particularly acute when pth-order spectral FE methods are used in conjunction with curved interfaces, such as those described by algebraic curves (eg, a circle or ellipse) as well as parametric curves. An example of a curved integration region is illustrated in Figure 1. The errors due to geometric representation and numerical cubature must be less than the approximation error to realize optimal rates of convergence with mesh refinement—$p + 1$ in L^2 norm, p in H^1 seminorm, and $2p$ in strain energy for pth-order spectral FEs.[38] The need for
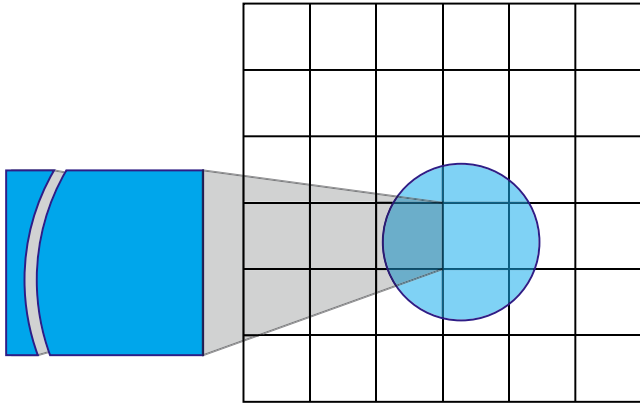
FIGURE 1 Integration over curved (convex and nonconvex) domains [Colour figure can be viewed at wileyonlinelibrary.com]

accurate numerical integration has long been recognized, and many contributions have emerged that address this issue. These papers have implemented methods that can be categorized as follows.

1. Customized cubature rules based on moment fitting.[39,40]
2. Integration on highly refined, linear reconstructions of the interface.[13,28,41]
3. Use of mapped, higher-order FEs.[5,9,29,42-44]
4. A recursive scheme to integrate on hyperrectangles wherein the interface is represented using a height function.[45]
5. Interface reconstruction with tree-based (quadtree and octree) methods and level set functions.[18]

Even though these contributions have allowed accurate integration over curved discontinuities, they all have certain drawbacks. For instance, tree-based methods and level set reconstruction methods involve complex data structures, are involved to implement, and accuracy and efficiency of such methods for general interfaces has not been established. Mapped FEs allow higher-order reconstruction of the interface but require element-partitioning and can only be used on elements that can be mapped to a reference element. Further, this mapping results in a loss of consistency, which limits the polynomials that can be reproduced on the mapped element.[46-49]

This paper introduces three improvements to the X-FEM for modeling holes and inclusions with curved interfaces.

1. Construction of level set function through implicitization of rational Bézier curves and level set zero isocontour reconstruction using adaptively generated cubic Hermite curves.
2. Extending the homogeneous numerical integration (HNI) method introduced in the works of Chin et al[50,51] to accurately and efficiently integrate discontinuous polynomials over domains with curved boundaries.
3. On appealing to the form of the enrichment function proposed by Moës et al,[10] we devise an enrichment function for affine and curved material interface problems that provides optimal convergence rates for bimaterial boundary-value problems on pth-order ($p \geq 1$) FE meshes.

In our implementation of the X-FEM, in addition to the above improvements, we also leverage tools from linear algebra and stabilization techniques that have been widely adopted in embedded interface methods to improve matrix conditioning of system matrices. In particular, we use the ghost penalty term introduced by Burman[52] to improve numerical stability issues caused by voids and a Jacobi preconditioner to improve the condition number of the stiffness matrix for both voids and material interfaces.

Taken together, all these advances provide the means to solve two-dimensional extended FE problems with holes and material inclusions using rectangular elements of arbitrary order with optimal convergence rates. However, even taken separately, each of these advances stands on its own and can be applied to other existing methodologies. For example, the need for accurate numerical integration over arbitrary curved geometry arises not only in embedded interface methods but also in the virtual element method[53] and may have applications in higher-order contact mechanics problems as well.[54] On cut elements, the use of the HNI method eliminates the need for element-partitioning to compute the weak form integrals. The HNI method is applicable to elements with constant Jacobian, since the basis functions are then (a sum of homogeneous) polynomials in the physical coordinates. This limitation notwithstanding, it permits additional flexibility in defining regions of integration, allowing more general interface geometries to be utilized with the X-FEM. In addition, the proposed enrichment function can find use outside the realm of solid mechanics, since it can be used to model arbitrary weak discontinuities. Finally, the use of rational Bézier curves to directly form an exact level set function presents a new

perspective on isogeometric methods,[55] since geometry defined using rational Bézier curves is captured exactly, albeit without using NURBS for the approximation of field quantities.

The remainder of this paper is organized as follows. In Section 2, we present the essentials on the level set method and explain how curved interfaces are reconstructed in a variety of scenarios. Then, in Section 3, we introduce the HNI method and extend it for accurate integration over domains that are bounded by parameterized curves. In Section 4, we present the weak form and extended FE displacement approximation to solve the elastostatic boundary-value problem for holes and material inclusions. In addition, we describe the construction of an improved enrichment function for material interface problems. Conditioning of system matrices is an issue that needs to be addressed in the X-FEM, and in this section, we introduce the ghost penalty term and the Jacobi preconditioner to combat this issue. Following this, implementation details of the HNI scheme within the X-FEM are discussed in Section 5, where we also provide a few verification tests to assess the accuracy of the integration scheme. In Section 6, we present numerical results on benchmark elastostatic problems such as a plate with a hole (circular, elliptical) as well as a plate with complicated holes defined by glyphs, and a two-phase composite with a circular-shaped inclusion. These examples demonstrate the accuracy and capabilities of the method and also showcase instances where the methodology is most effective. Finally, we close with a summary of our main findings in Section 7.

2 | LEVEL SET METHOD

Isocontours of a $(d + 1)$-dimensional function $\varphi(\boldsymbol{x})$ can be used to track the location of geometric interfaces within a d-dimensional domain. This idea forms the basis of the level set method. Generally, in the level set method, the level curve $\varphi(\boldsymbol{x}) = 0$ is selected as the interface location. Further, $\varphi(\boldsymbol{x}) < 0$ and $\varphi(\boldsymbol{x}) > 0$ are used to locate regions of interest within the domain. Herein, we use $\varphi(\boldsymbol{x}) < 0$ to denote the region that lies inside the closed interface and $\varphi(\boldsymbol{x}) > 0$ to denote the region that lies outside the closed interface. Osher and Sethian[4] used this approach to simplify the representation of temporally evolving interfaces whose evolution is described by a hyperbolic equation related to $\varphi(\boldsymbol{x})$. Sukumar et al[3] recognized the power of this approach when coupled with the X-FEM for modeling holes and material interfaces. The coupling of the level set method with the X-FEM is a very attractive approach for solving problems with voids and multimaterials, and it is the procedure we use in this paper.

The level set method allows node and element locations to be easily inferred in the X-FEM. On computing $\varphi(\boldsymbol{x})$ at a node in the FE mesh, we can determine the location of the node relative to the interface. Further, nodal values of $\varphi(\boldsymbol{x})$ can be used to infer elements that are cut by the level set zero isocontour. In cut elements, the element domain has a region inside the interface and a region outside the interface. These regions must exist if some of the nodes of an element are inside the interface and the remaining nodes are outside the interface. This case is illustrated in Figure 2A. However, this method of detecting cut elements is not foolproof, as revealed in Figure 2B. In Figure 2B, all nodes are outside the interface, and the intersection of the element with the zero level set goes undetected. Detection can be improved by evaluating the level set function at additional points in the element, as is done in the work of Fries and Omerović.[43] Evaluating the level set function at additional points in the element increases the likelihood of detection of cut elements and reduces the error caused by missed detection of cut elements.

FIGURE 2 Detecting the intersection of an element with the level set zero isocontour based on nodal values of $\varphi(\boldsymbol{x})$. (A) Some nodes are inside the interface (filled circles) and some nodes are outside the interface (open circles), so the intersection is detected, and (B) all nodes are outside the interface, so the intersection is (erroneously) not detected [Colour figure can be viewed at wileyonlinelibrary.com]
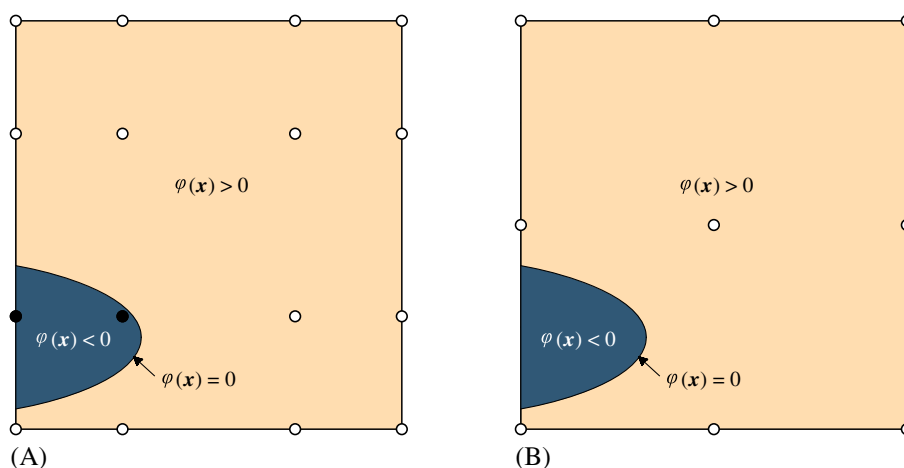
While a level set function simplifies knowing the location of a point with respect to a geometric region, determining the exact location of the curve requires additional information or a method of approximation. The level set method only provides the location of the interface implicitly, through the roots of the equation $\varphi(\mathbf{x}) = 0$. To accurately compute integrals using the HNI method, the location of the interface must be known to high precision (see Section 3). This need is particularly acute when higher-order polynomials are used to approximate field quantities, since optimal convergence of the X-FEM relies on the geometric error being less than the approximation error.

Depending on the source of the level set geometry, there are different methods to explicitly construct the curve $\varphi(\mathbf{x}) = 0$ and/or a corresponding level set function, $\varphi(\mathbf{x})$. In this paper, we consider the following four different origins of the level set geometry.

1. An open or closed convex polygon is used to generate the level set function.
2. An explicitly known conic section is used to construct the level set function.
3. The level set function is generated from a known function whose gradient can also be computed (coined a gradient-augmented level set function by Nave et al[56]).
4. The level set function is not known explicitly and can only be computed when given a specific location in the domain.

The first case is well known, and the level set function and zero isocontour for a polygon can be found in the work of Sukumar et al.[3] Sections 2.1 to 2.3 detail cases 2 to 4.

2.1 | Level sets functions for conic sections

For any given conic, interface reconstruction can be accomplished using its representation as a rational quadratic Bézier curve. Further, this rational quadratic Bézier is easily converted into an implicit equation by considering its barycentric representation, as described by Farin.[57] For a given coordinate $\mathbf{x}$ and Bézier control points $\mathbf{p}_0$, $\mathbf{p}_1$, and $\mathbf{p}_2$, we solve the linear system of equations

$$\tau_0 \mathbf{p}_0 + \tau_1 \mathbf{p}_1 + \tau_2 \mathbf{p}_2 = \mathbf{x},$$
$$\tau_0 + \tau_1 + \tau_2 = 1,$$

for parameters τ_0, τ_1, and τ_2. The value of the level set function is then given by

$$\varphi(\mathbf{x}) = \tau_1^2 - 4 \frac{\tau_0 \tau_2 w_1^2}{w_0 w_2},$$

where w_0, w_1, and w_2 are weights associated with each of the control points. For conic sections in standard form, $w_0 = w_2 = 1$ and

$$\varphi(\mathbf{x}) = \tau_1^2 - 4\tau_0 \tau_2 w_1^2. \tag{1}$$

This provides an exact level set representation of the conic, which is used to determine elements that are cut by the level set zero isocontour. The curve $\varphi(x) = 0$, which is needed to compute integrals using the HNI method, is obtained directly from segments of the Bézier representation of the curve. This method is used to model the elliptical hole in Section 6.3 and to generate the glyphs that appear in Section 6.4. For cubic or higher-degree Bézier curves, elimination techniques[58] can be used to convert from explicit to implicit form, a process called implicitization. Methods of implicitization generally grow in complexity as the polynomial degree increases in the Bézier curve, though simplifications are possible through, for example, methods using moving curves.[59,60]

A level set function, $\varphi(\mathbf{x})$, coincides with the signed distance function if

$$\varphi(\mathbf{x}) = \min_{\mathbf{x}_\Gamma \in \Gamma} \pm \|\mathbf{x} - \mathbf{x}_\Gamma\|, \tag{2}$$

where $\| \cdot \|$ denotes the L^2 norm of its argument and Γ is the domain of the level set zero isocontour. Following the convention introduced earlier in this section, the sign is negative (respectively, positive) when inside (respectively, outside) Γ. For the material interface problem, a level set function that is also the distance function results in a piecewise linear enrichment function in the direction that is normal to the material interface (see Section 4.3.2). While implicitization is an effective technique for transforming a rational quadratic Bézier to a level set representation, the resulting level set

FIGURE 3 Level set functions for a circular interface. The level set intersects the mesh when $\varphi(\boldsymbol{x}) = 0$, defining the circle. Regions where $\varphi(\boldsymbol{x}) < 0$ define the area inside the circle. (A) The level set function, $\varphi(\boldsymbol{x}) = \sqrt{x^2 + y^2} - 0.5$, coincides with the distance function. (B) The level set function, $\varphi(\boldsymbol{x}) = 4x^2 + 4y^2 - 1$, is generated from implicitization of a quadratic Bézier curve [Colour figure can be viewed at wileyonlinelibrary.com]
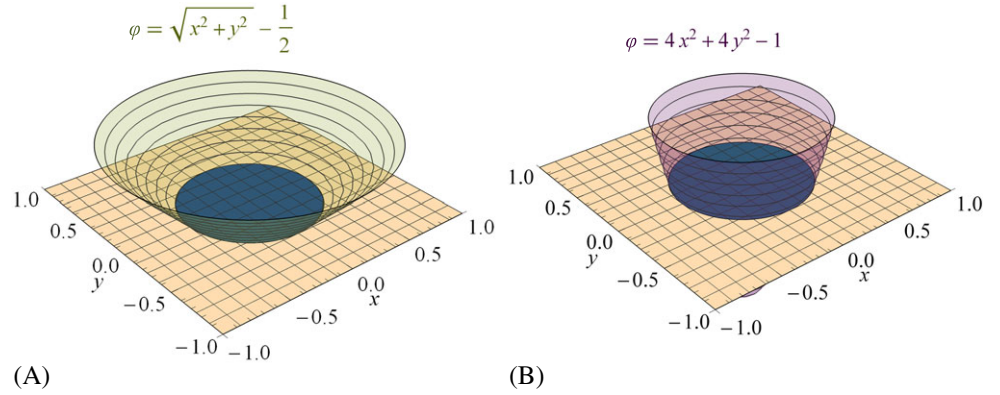
function is not a distance function. For a circle, the signed distance function is

$$\varphi(\boldsymbol{x}) = \|\boldsymbol{x} - \boldsymbol{x}_c\| - a, \tag{3}$$

where $\boldsymbol{x}_c$ is the center of the circle and a is its radius. This level set function is presented in Figure 3A and is used in the circular inclusion example in Section 6.6. For comparison, the level set function for the circle generated through implicitization of the rational Bézier representation using (1) is shown in Figure 3B. Generation of a signed distance function from a parameterized curve can be accomplished using a procedure such as the one described by Benowitz and Waisman.[61]

2.2 | Interface reconstruction with gradient-augmented level sets

When the level set function and its gradient are computable, the level curve $\varphi(\boldsymbol{x}) = 0$ is not known in closed-form and must be approximated. To reconstruct the level set zero isocontour, cubic Hermite functions are used. For $t \in [0, 1]$, a cubic Hermite function has the form

$$\boldsymbol{c}(t) = (2t^3 - 3t^2 + 1)\boldsymbol{p}_0 + (t^3 - 2t^2 + t)m_0\boldsymbol{t}_0 + (-2t^3 + 3t^2)\boldsymbol{p}_1 + (t^3 - t^2)m_1\boldsymbol{t}_1, \tag{4}$$

where $\boldsymbol{p}_0 = \boldsymbol{c}(0)$, $\boldsymbol{p}_1 = \boldsymbol{c}(1)$, $m_0\boldsymbol{t}_0 = \boldsymbol{c}'(0)$, $m_1\boldsymbol{t}_1 = \boldsymbol{c}'(1)$. The construction of the cubic Hermite function simplifies C^1 interpolation of data, since parameters directly correspond to function values and derivative values at the endpoints of the curve. The cubic Hermite function can be used to interpolate a sequence of d-dimensional coordinates, $(\boldsymbol{x}_1, \boldsymbol{x}_2, \ldots, \boldsymbol{x}_n)$. This is accomplished by solving a tridiagonal linear system of equations and results in a C^2 cubic spline interpolant.[62] The cubic spline interpolant is the best interpolation of the sequence in the sense that it (approximately) minimizes curvature over all possible curves that pass through the given coordinates. Assuming the underlying function being interpolated has four continuous derivatives, the L^∞ error of the interpolation is $\mathcal{O}(\bar{h}^4)$,[63] where $\bar{h} = \max_{i=1, \ldots, n-1} \|\boldsymbol{x}_{i+1} - \boldsymbol{x}_i\|$. These properties render the cubic Hermite function to be a very popular choice for interpolating pointwise data.

In the context of the level set method, cubic Hermite functions can be used to reconstruct the zero isocontour of a level set function. If $\varphi(\boldsymbol{x})$ and its gradient are computable, the endpoints ($\boldsymbol{p}_0$ and $\boldsymbol{p}_1$) and tangent directions ($\boldsymbol{t}_0$ and $\boldsymbol{t}_1$) of the curve can be determined. For most typical cases, the initial endpoints of $\boldsymbol{p}_0$ and $\boldsymbol{p}_1$ will intersect the boundary of an element in the mesh. Newton's method is used to identify the intersection of the element boundary with the level curve $\varphi(\boldsymbol{x}) = 0$. When FEs are arranged on a rectangular grid, finding the endpoints of the curve is reduced to a one-dimensional problem, simplifying implementation of Newton's method. For example, when an element edge lies on the line $y = y_c$, Newton iterations are computed via

$$x_{i+1} = x_i - \frac{f(x_i, y_c)}{f_{,x}(x_i, y_c)},$$

and continue until $|f(\boldsymbol{x})| \leq \delta$ or a maximum number of iterations has been reached. Since the zero level set can intersect an edge of an element more than once, multiple initial guesses of x (or y) are used to determine the location of the interface. If a point on the interface is not identified by Newton's method, first a bisection method is used to provide an improved initial guess. Once $\boldsymbol{p}_0$ and $\boldsymbol{p}_1$ are established, the tangent directions ($\boldsymbol{t}_0$ and $\boldsymbol{t}_1$) are perpendicular to the gradient of $\varphi(\boldsymbol{x})$.
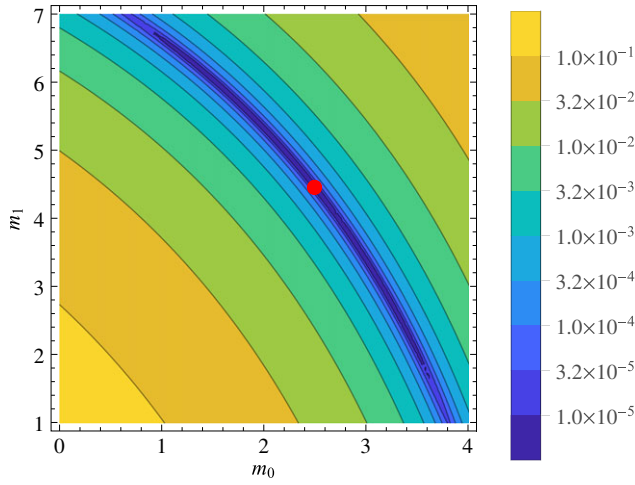
FIGURE 4 Values of the objective function defined in (6) for $\varphi(\boldsymbol{x}) = (x - \frac{1}{2})^2 - y - \frac{1}{2}$. The minimum is the circle located at $m_0 = 2.497$ and $m_1 = 4.454$

The magnitude of the tangent vectors, m_0 and m_1, must still be determined. Ideally, m_0 and m_1 are set such that the cubic Hermite function approximates the zero isocontour as closely as possible. If the Hermite reconstruction is exact, we recover

$$\varphi^2(\boldsymbol{c}(t)) = 0 \quad \forall t \in [0, 1]$$

or, in a weak (integral) sense,

$$\int_0^1 \varphi^2(\boldsymbol{c}(t)) \, dt = 0. \tag{5}$$

Note that this is not a line integral since the speed of the parameter t is not accounted for; however, since any value of the integral in (5) other than zero is immaterial, the integral does not need to be a path integral. To select optimal values for m_0 and m_1, we choose

$$\boldsymbol{m}^* = \underset{\boldsymbol{m} \in \mathbb{R}^2}{\operatorname{argmin}} \, F(\boldsymbol{m}), \tag{6}$$

where $F(\boldsymbol{m}) = \int_0^1 \varphi^2(\boldsymbol{c}(t, \boldsymbol{m})) \, dt$ is the objective function and $\boldsymbol{m} = \{m_0, m_1\}$ is now an unknown in the expression for $\boldsymbol{c}$ given in (4). A similar method to approximate the implicit curve $\varphi(\boldsymbol{x}) = 0$ is used by Dokken[64] and Jüttler and Chalmovianský.[65] Jüttler and Chalmovianský[65] adopt rational Bézier curves to represent the implicit curve approximation. Rational Bézier curves are able to reproduce more shapes, as they can exactly represent genus zero algebraic curves. However, since they are nonpolynomial, they introduce error in the quadrature rule. This numerical optimization problem can be solved using techniques such as Newton's method. However, we sometimes observed the minimum of $F(\boldsymbol{m})$ to lie within a long, nearly flat valley (see Figure 4), similar to the Rosenbrock function.[66] This causes difficulty in attaining the optimal values of $\boldsymbol{m}$ using many standard methods of nonlinear optimization. We found the Broyden-Fletcher-Goldfarb-Shanno (BFGS) algorithm or Newton's method with a reduced step size to yield acceptable results, though other methods may exist that provide additional improvements. The initial guess for m_0 and m_1 is chosen to be magnitude of the gradient at $\boldsymbol{p}_0$ and $\boldsymbol{p}_1$, respectively. The BFGS algorithm is especially appealing since it does not require computing the second derivatives of the level set function, which may not be available.

Once $\boldsymbol{m}^*$ is obtained, if $F(\boldsymbol{m}^*) > 0$, then error exists between the parameterized curve and the level set zero isocontour. We estimate the total error over the path by computing

$$e(\boldsymbol{m}^*) = \sqrt{\int_0^1 \left(\frac{\varphi(\boldsymbol{c}(t, \boldsymbol{m}^*))}{\|\nabla \varphi(\boldsymbol{c}(t, \boldsymbol{m}^*))\|} \right)^2 \left\| \frac{\partial \boldsymbol{c}(t, \boldsymbol{m}^*)}{\partial t} \right\| \, dt}. \tag{7}$$

If $e(\boldsymbol{m}^*) > \epsilon$, where ϵ is a user-defined error tolerance, then the error between the parameterized curve and the level set zero isocontour exceeds the acceptable bound defined by ϵ. This error can be reduced by splitting the cubic Hermite function into two separate cubic Hermite functions, $\boldsymbol{c}_1(t, \boldsymbol{m})$ and $\boldsymbol{c}_2(t, \boldsymbol{m})$. The parameterized curve is split at its midpoint ($t = 0.5$), then Newton's method is used to find a nearby point on the level set zero curve. This point becomes $\boldsymbol{p}_1$ in $\boldsymbol{c}_1(t, \boldsymbol{m})$

and p_0 in $c_2(t, m)$. Optimal m is then computed on $c_1(t, m)$ and $c_2(t, m)$, and $e(m^*)$ is compared to ϵ for both curves. Additional parameterized curves are created until $e(m^*) \leq \epsilon$ for all segments of the curve. With curve refinement based on error of the approximation from the implicit curve (defined by $e(m^*)$), the number of Hermite functions needed to reconstruct the curve is optimized. In other words, curve refinement only occurs where the Hermite function approximation of the zero isocontour is not sufficiently accurate. The effect of ϵ on integration error is examined in Sections 5.1.1 and 5.1.2. Assuming $\varphi(x) \in C^1$, the resulting optimized parametric representation is G^1 continuous since tangent directions match across each approximating function, though the curve speed, $\|c'(t)\|$, may differ.

2.3 | Interface reconstruction with a level set (no gradient)

When only the level set function is computable over a domain discretized by FEs, the FE interpolant can be leveraged to generate an approximation of level set isocontours. This approximation is accurate to the order of the FE approximation. To generate the interface, the level set function itself is first approximated as

$$\varphi^h(x) = \sum_{i \in \mathbb{I}_e} N_i(x)\varphi_i, \tag{8}$$

where $\mathbb{I}_e$ is the index set of nodes belonging to Ω_e ($x \in \Omega_e$), $N_i(x)$ is the spectral FE shape function (see Section 4.2) associated with node i, and $\varphi_i := \varphi(x_i)$ is the nodal value of $\varphi(x)$. This provides a piecewise polynomial approximation of the level set function, and further, a piecewise polynomial approximation of the curve $\varphi(x) = 0$ (ie, $\varphi^h(x) = 0$). We point out that this choice of approximating the level set function is necessary for the material interface problem, since the enrichment function in the X-FEM is formulated in terms of $\varphi^h(x)$ (see Section 4.3.2). In this paper, the level set function is used to directly set the nodal coefficients; however, if a level set function that coincides with the distance function is desired, a technique such as the one outlined in the work of Saye[67] can be used to set nodal values of the level set function. The zero isocontour of $\varphi^h(x)$ is reconstructed using optimized cubic Hermite functions, as described in Section 2.2. Sufficient parametric Hermite curves are placed such that $e(m^*) \leq \epsilon$ for all curves.

3 | HOMOGENEOUS NUMERICAL INTEGRATION METHOD

Lasserre[68] used Stokes' theorem and Euler's homogeneous function theorem to simplify integration over a d-dimensional polytope to integration over the $(d-1)$-dimensional faces of the polytope. The HNI method of Chin et al[50] extends Lasserre's approach to nonconvex regions and is also efficient for weakly singular functions that arise in the X-FEM.[51] In this paper, we further extend the HNI method to regions bounded by parametric curves. This extension is discussed in Section 3.2 and examples illustrating its efficiency in integrating homogeneous functions are presented in Section 3.3.

Let $f(x)$ be a positively homogeneous function of degree q that is continuously differentiable

$$f(\lambda x) = \lambda^q f(x) \quad (\lambda > 0), \tag{9}$$

which satisfies Euler's homogeneous function theorem

$$qf(x) = \nabla f(x) \cdot x \quad \forall x \in \begin{cases} \mathbb{R}^d & \text{if } q > 0 \\ \mathbb{R}^d \setminus \{0\} & \text{if } q < 0. \end{cases} \tag{10}$$

Besides the monomial $x^a y^b$ that is homogeneous with degree $q = a + b$, functions in polar coordinates are also homogeneous: $f(r) = \sqrt{x^2 + y^2} := r$ is homogeneous with degree $q = 1$.

Our objective is to integrate a homogeneous function, $f(x)$, over a domain $V \subset \mathbb{R}^d$ ($d = 2, 3$), ie,

$$I = \int_V f(x)\,dx.$$

For a vector field $\boldsymbol{X}$, Stokes' (divergence) theorem can be stated as

$$\int_V (\nabla \cdot \boldsymbol{X}) f(\boldsymbol{x}) d\boldsymbol{x} + \int_V \nabla f(\boldsymbol{x}) \cdot \boldsymbol{X} \, d\boldsymbol{x} = \int_{\partial V} (\boldsymbol{X} \cdot \boldsymbol{n}) f(\boldsymbol{x}) d\sigma, \tag{11}$$

where ∂V is the boundary of V and $d\sigma$ is the Lebesgue measure on ∂V. For a homogeneous function f and choosing $\boldsymbol{X}$ as the position vector $\boldsymbol{x}$, (11) yields

$$d \int_V f(\boldsymbol{x}) d\boldsymbol{x} + \int_V \nabla f(\boldsymbol{x}) \cdot \boldsymbol{x} \, d\boldsymbol{x} = \sum_{i=1}^m \int_{F_i} (\boldsymbol{x} \cdot \boldsymbol{n}_i) f(\boldsymbol{x}) d\sigma, \tag{12}$$

where $\partial V := \overline{F_1 \cup F_2 \cup \cdots \cup F_m}$. Invoking Euler's theorem given in (10), (12) simplifies to

$$\int_V f(\boldsymbol{x}) d\boldsymbol{x} = \frac{1}{d+q} \sum_{i=1}^m \int_{F_i} (\boldsymbol{x} \cdot \boldsymbol{n}_i) f(\boldsymbol{x}) d\sigma. \tag{13}$$

Equation (13) relates integration of a positively homogeneous function $f(\boldsymbol{x})$ over a domain in $\mathbb{R}^d$ to integration over the domain's $(d-1)$-dimensional boundary.

For the developments in this paper, (13) is sufficient; however, it is worth noting that, for a polytope, (13) can be further reduced and exact integration is realized when f is a homogeneous polynomial.[50] In the remainder of this section, we describe simplifications to (13) that are used in subsequent sections, and we present a few illustrative examples to show the effectiveness of the integration scheme. From this point forward, we assume $V \subset \mathbb{R}^2$ and further that $\partial V = \overline{\partial V_A \cup \partial V_C}$, where ∂V_A is a line segment in one dimension and ∂V_C is a parametric curve.

3.1 | Affine interface

An affine surface can be described as a linear equation, $\boldsymbol{a} \cdot \boldsymbol{x} = b$. The normal of this surface is the normalized gradient of this equation, ie, $\boldsymbol{n} = \boldsymbol{a}/\|\boldsymbol{a}\|$. Substituting into (13), we obtain

$$\int_{F_i} (\boldsymbol{x} \cdot \boldsymbol{n}_i) f(\boldsymbol{x}) d\sigma = \frac{b_i}{\|\boldsymbol{a}_i\|} \int_{F_i \subset \partial V_A} f(\boldsymbol{x}) d\sigma. \tag{14}$$

Therefore, for V bounded by affine interfaces, integration of positively homogeneous functions reduces to integration of $f(\boldsymbol{x})$ on the one-dimensional boundary. Note that this integration can be performed easily and accurately with Gauss quadrature.

3.2 | Parametric interface

We consider parametric curves of the form $\boldsymbol{c}(t)$, where $t \in [0, 1]$ is a parameter such that $\boldsymbol{c}(0)$ and $\boldsymbol{c}(1)$ give the endpoints of $F_i \subset \partial V_C$. The form $\boldsymbol{c}(t)$ is general enough to encompass many types of curves, including Bézier curves (both regular and rational), cubic Hermite curves, and B-spline curves. Substituting into (13), we obtain

$$\int_{F_i} (\boldsymbol{x} \cdot \boldsymbol{n}_i) f(\boldsymbol{x}) d\sigma = \int_0^1 (\boldsymbol{c}_i(t) \cdot \boldsymbol{n}_i) f(\boldsymbol{c}_i(t)) \|\boldsymbol{c}_i'(t)\| \, dt, \tag{15}$$

where $\boldsymbol{c}_i'(t)$ is the derivative with respect to the parameter t, ie, the hodograph of the curve. The normal of $\boldsymbol{c}(t)$ is a normalized vector perpendicular to its hodograph. Substituting this into (15) leads to

$$\int_{F_i} (\boldsymbol{x} \cdot \boldsymbol{n}_i) f(\boldsymbol{x}) d\sigma = \int_0^1 \left(\boldsymbol{c}_i(t) \cdot \left(\boldsymbol{c}_i'(t) \times \boldsymbol{e}_3 \right) \right) f(\boldsymbol{c}_i(t)) dt, \tag{16}$$

where e_3 is the unit vector in the third dimension. This equation reduces integration of positively homogeneous functions over V bounded by parameterized curves to one-dimensional integrals over the parameter t. This integration can be computed using Gauss quadrature, and further, if $c(t)$ and $f(x)$ are polynomial, integration is exact with an appropriate quadrature rule.

3.3 | Integration examples

Several examples of the HNI scheme are demonstrated in the works of Chin et al.[50,51] Herein, we focus on examples relevant to the developments that follow this section.

3.3.1 | Region bounded by a cubic Hermite curve

Consider a biunit square, $\Omega = [-1, 1]^2$, which is cut by a cubic Hermite curve. Since Hermite functions can be represented as Bézier curves, this example also serves to verify our approach for integrating regions bounded by Bézier curves. We consider the integration of two functions over Ω: $f(x) = 1$ and $f(x) = x^2y^4 + x^5y$, which are homogeneous polynomials of degree $q = 0$ and $q = 6$, respectively. The equation for a cubic Hermite curve is given in (4). For this example, we choose the coefficients to be

$$p_0 = \{0.5, -1\}^T, \quad p_1 = \{-0.5, 1\}^T, \quad t_0 = \{0, 1\}^T, \quad t_1 = \left\{ -\frac{1}{\sqrt{2}}, \frac{1}{\sqrt{2}} \right\}^T, \quad m_0 = 3, \quad m_1 = 3\sqrt{2}.$$

We integrate the region to the left of the Hermite curve (see Figure 5 for an illustration). Since the region of integration contains both affine edges and parametric edges, both (14) and (16) are required to compute the integral. For $f(x) = 1$, the integrand is constant over affine edges and is degree 5 over the parametric edge ($c(t)$ is degree 3 and $c'(t)$ is degree 2, which renders their product to be degree 5). Therefore, one Gauss point is needed on the affine edges and three Gauss points are needed on the spline curve. The location of the cubature points are shown in Figure 5A, and the cubature scheme results in machine precision accuracy. For $f(x) = x^2y^4 + x^5y$, more cubature points are needed—4 Gauss points on affine edges and 12 Gauss points on the parametric curve. With this integration scheme (see Figure 5B for an illustration), machine precision accuracy is obtained.

3.3.2 | Region bounded by a conic section

We integrate over the intersection of a biunit square, $\Omega = [-1, 1]^2$ and a conic section. Conic sections are nonpolynomial, but can be represented by rational Bézier curves, so this example serves as a test for integrating rational functions. As in the previous example, we integrate $f(x) = 1$ (degree $q = 0$) and $f(x) = x^2y^4 + x^5y$ (degree $q = 6$). The conic section is defined by the rational quadratic Bézier curve

$$c(t) = \frac{B_{0,2}(t)w_0 p_0 + B_{1,2}(t)w_1 p_1 + B_{2,2}(t)w_2 p_2}{B_{0,2}(t)w_0 + B_{1,2}(t)w_1 + B_{2,2}(t)w_2}$$

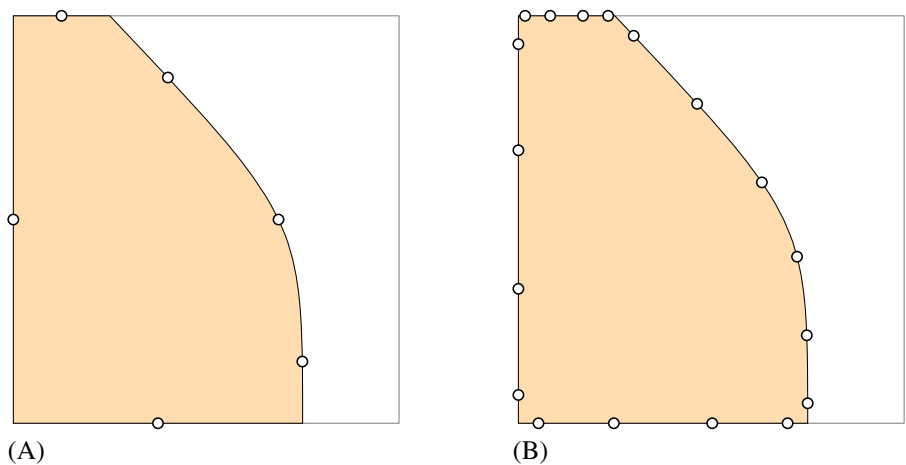**FIGURE 5** Location of cubature points (circles) for machine precision accuracy over a region bounded by a cubic Hermite curve. (A) $f(x) = 1$ and (B) $f(x) = x^2y^4 + x^5y$ [Colour figure can be viewed at wileyonlinelibrary.com]
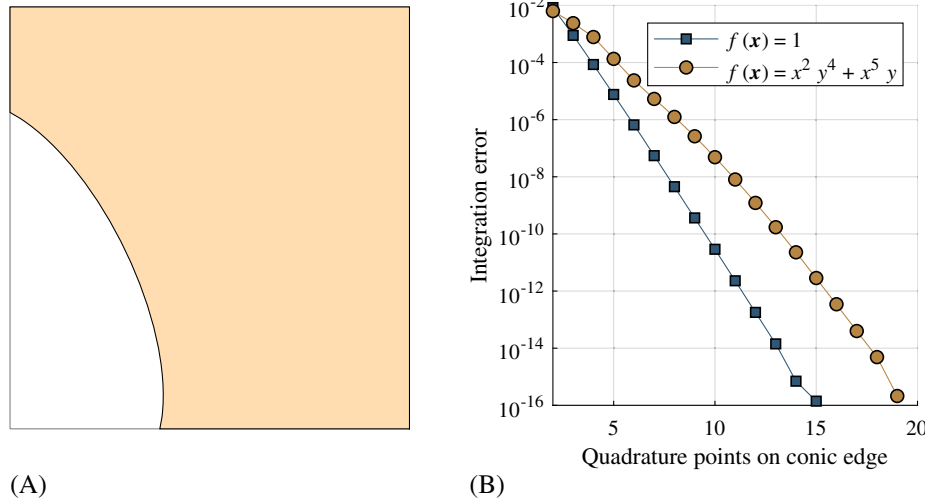
(A)   (B)

FIGURE 6 (A) Integration region bounded by affine edges and a conic section, and (B) integration error over the domain as a function of cubature points on the conic section for two functions, $f(\boldsymbol{x}) = 1$ and $f(\boldsymbol{x}) = x^2 y^4 + x^5 y$ [Colour figure can be viewed at wileyonlinelibrary.com]

for $t \in [0, 1]$. The control points of the curve are $\boldsymbol{p}_0$, $\boldsymbol{p}_1$, and $\boldsymbol{p}_2$; w_0, w_1, and w_2 are weights that control the shape of the conic; and $B_{0,2}(t) = (1 - t)^2$, $B_{1,2} = 2t(1 - t)$, and $B_{2,2} = t^2$ are the Bernstein polynomials of degree two. For this example, we choose control points and weights

$$\boldsymbol{p}_0 = \{-1, 0.5\}^T, \quad \boldsymbol{p}_1 = \{0, 0\}^T, \quad \boldsymbol{p}_2 = \{-0.25, -1\}^T,$$
$$w_0 = 1, \quad w_1 = 0.5, \quad w_2 = 1.$$

This produces an elliptical segment that cuts the biunit square. The region of integration is illustrated in Figure 6A. Since the integrand is not polynomial over the conic interface, one-dimensional Gauss quadrature does not produce an exact result. To investigate cubature convergence, we study the error in integration over the region with varying numbers of cubature points on the conic section. On affine edges, the number of cubature points is held constant at the minimum needed for exact integration. In Figure 6B, we show the relationship between the number of cubature points on the curved section and the relative error in computing the integral. Machine precision accuracy (defined as integration error less than 1×10^{-15}) requires 14 cubature points on the conic section for $f(\boldsymbol{x}) = 1$ and 19 cubature points on the conic section for $f(\boldsymbol{x}) = x^2 y^4 + x^5 y$. Exponential rates of convergence are observed for both functions.

4 | EXTENDED FINITE ELEMENT METHOD

4.1 | Elastostatic boundary-value problem

Consider an inhomogeneous linear elastic body that occupies the domain $\Omega \subset \mathbb{R}^2$, with boundary $\Gamma = \partial\Omega$. The body is composed of two elastically homogeneous materials, and the domain of each material is Ω_1 and Ω_2, such that $\Omega = \overline{\Omega_1 \cup \Omega_2}$. The boundary that defines the material interface between Ω_1 and Ω_2 is denoted by Γ_{mat}. The two materials are assumed to be perfectly bonded at the interface. We point out that only two materials are chosen to simplify the exposition. The body also contains an arbitrary number of voids. The voids occupy the region Ω_{hole} and the boundary of all of the voids is Γ_{hole}. The boundary $\Gamma = \overline{\Gamma_t \cup \Gamma_u \cup \Gamma_{\text{hole}}}$, where these three subsets are disjoint. The boundary subsets Γ_t and Γ_u are where tractions and displacements are imposed, respectively. A schematic of the boundary-value problem is shown in Figure 7.

For the elastostatic boundary-value problem, the governing equations are

$$\nabla \cdot \boldsymbol{\sigma} + \boldsymbol{b} = 0 \quad \text{in } \Omega, \tag{17a}$$

$$\boldsymbol{\sigma} = \mathbb{C}_i : \boldsymbol{\varepsilon} \quad \text{in } \Omega_i, \tag{17b}$$

$$\boldsymbol{\varepsilon} = \nabla_s \boldsymbol{u} \quad \text{in } \Omega, \tag{17c}$$

where $\boldsymbol{u}$ is the displacement field, ∇_s is the symmetric gradient operator, $\boldsymbol{\varepsilon}$ is the small-strain tensor, $\boldsymbol{\sigma}$ is the Cauchy stress tensor, $\boldsymbol{b}$ is the body force per unit volume, and $\mathbb{C}_i$ is the material moduli tensor for a homogeneous, linear elastic
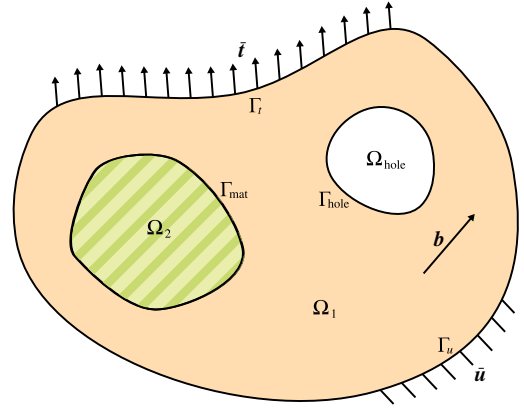
FIGURE 7 Elastostatic boundary-value problem for domain with two distinct linear elastic materials and a hole [Colour figure can be viewed at wileyonlinelibrary.com]

isotropic material in the domain Ω_i ($i = 1, 2$). The essential boundary conditions, traction boundary conditions, and interface conditions are

$$\boldsymbol{u} = \bar{\boldsymbol{u}} \quad \text{on } \Gamma_u, \tag{18a}$$

$$\boldsymbol{n} \cdot \boldsymbol{\sigma} = \bar{\boldsymbol{t}} \quad \text{on } \Gamma_t, \tag{18b}$$

$$\boldsymbol{n} \cdot \boldsymbol{\sigma} = \boldsymbol{0} \quad \text{on } \Gamma_{\text{hole}}, \tag{18c}$$

$$[[\boldsymbol{u}]] = \boldsymbol{0} \quad \text{on } \Gamma_{\text{mat}}, \tag{18d}$$

$$[[\boldsymbol{n} \cdot \boldsymbol{\sigma}]] = \boldsymbol{0} \quad \text{on } \Gamma_{\text{mat}}. \tag{18e}$$

In (18), $\boldsymbol{n}$ is the unit vector that is normal to the indicated boundary and $[[\cdot]]$ is the jump operator that represents the jump in its argument across the interface.

For the constitutive equation (17b) and the interface conditions in (18d) and (18e) to be satisfied when $\mathbb{C}_1 \neq \mathbb{C}_2$, the displacement field must be continuous but the normal strain, namely, $\boldsymbol{n} \cdot \boldsymbol{\varepsilon} \cdot \boldsymbol{n}$, must be discontinuous (weak discontinuity) across Γ_{mat}. This condition is met if the displacement field u_i ($i = 1, 2$) has a discontinuous normal derivative on Γ_{mat}. The presence of a weak discontinuity is met in the standard FE method via meshing the domain and its internal and external boundaries so that Γ_{mat} is the union of element edges in the FE mesh. In the X-FEM, (18d) and (18e) are satisfied on a mesh that does not conform to the material interface by augmenting the standard FE displacement approximation with an enriched contribution (via the PU framework) that is continuous but its normal derivative on Γ_{mat} is discontinuous.[3] The details on the construction of the enrichment function are provided in Section 4.3.2.

Let $\mathbb{U}_i$ ($i = 1, 2$) denote the affine subspace of functions in the Sobolev space $H^1(\Omega)$ whose trace on Γ_u is equal to $\bar{u}_i$ and whose normal derivative on Γ_{mat} is discontinuous. In addition, let $\mathbb{U}_0$ denote the linear subspace of functions in the Sobolev space $H^1(\Omega)$ that vanish on Γ_u and whose normal derivative on Γ_{mat} is discontinuous. The weak form of (17) and (18) is as follows: find $\boldsymbol{u} \in \mathbb{U}_1 \times \mathbb{U}_2$ such that

$$a(\boldsymbol{u}, \delta\boldsymbol{u}) + j(\boldsymbol{u}, \delta\boldsymbol{u}) = \ell(\delta\boldsymbol{u}) \quad \forall \delta\boldsymbol{u} \in \mathbb{U}_0 \times \mathbb{U}_0, \tag{19a}$$

where

$$a(\boldsymbol{u}, \delta\boldsymbol{u}) := \int_\Omega \boldsymbol{\sigma} : \delta\boldsymbol{\varepsilon}\, d\boldsymbol{x}, \quad \ell(\delta\boldsymbol{u}) := \int_\Omega \boldsymbol{b} \cdot \delta\boldsymbol{u}\, d\boldsymbol{x} + \int_{\Gamma_t} \boldsymbol{t} \cdot \delta\boldsymbol{u}\, dS. \tag{19b}$$

In (19), the term $j(\boldsymbol{u}, \delta\boldsymbol{u})$ is a *ghost penalty*[52] stiffness to improve matrix conditioning. This term is defined in Section 4.6.

4.2 | Spectral FE discretization

In the X-FEM, since geometric features such as holes and material interfaces are not represented by the mesh, a simple FE mesh suffices. For applications in solid continua, quadrilateral FEs are preferred to triangular FEs, and Cartesian meshes provide numerous benefits and simplifications as well. From the perspective of the X-FEM, additional advantages include easier implementation for higher-order elements, compatibility with the HNI scheme, which requires basis functions that are a linear combination of homogeneous polynomials, and greatly simplified computation of the ghost penalty stiffness term introduced in Section 4.6. Accordingly, we restrict ourselves to Cartesian FE meshes in the subsequent developments.
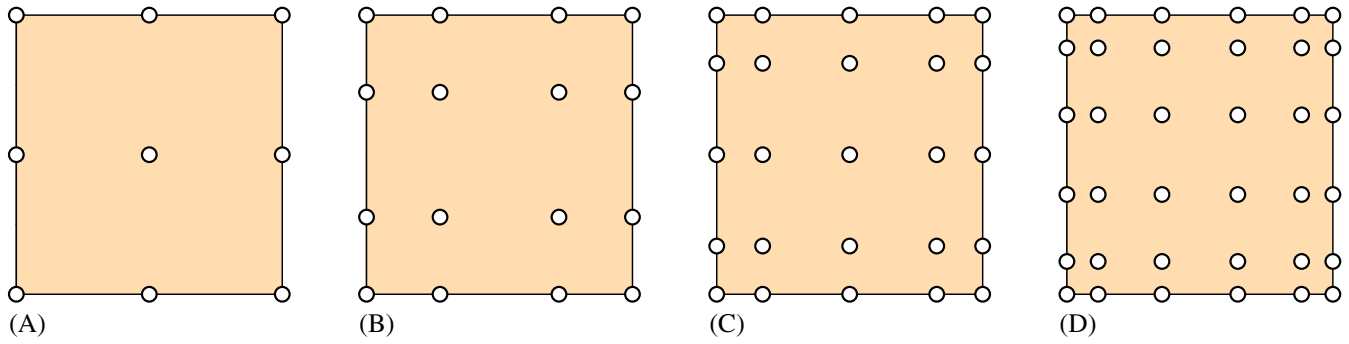
FIGURE 8 Gauss-Lobatto nodes for pth-order spectral elements. (A) $p = 2$, (B) $p = 3$, (C) $p = 4$, and (D) $p = 5$ [Colour figure can be viewed at wileyonlinelibrary.com]

Consider a tessellation $\mathcal{T}$ of the domain $\overline{\Omega \cup \Omega_{\text{hole}}}$ into a Cartesian mesh of M elements. The domain of the eth element of the mesh is Ω_e. On each pth-order FE, we define an index nodal set $\mathbb{I}_e$ with $|\mathbb{I}_e| = (p + 1)^2$. The nodal coordinates are determined by the coordinates of $p + 1$ tensor-product Gauss-Lobatto nodes shifted to the domain Ω_e. If $\Omega_e = [x_a, x_b] \times [y_a, y_b]$, and given the location of one-dimensional Gauss-Lobatto nodes $\{\xi_j\}_{j=1}^{p+1}$, $\{\eta_k\}_{k=1}^{p+1}$, where $\xi_j \in [-1, 1]$ and $\eta_k \in [-1, 1]$, then the nodal coordinates are

$$x_j = \frac{x_b + x_a}{2} + \xi_j \frac{x_b - x_a}{2}, \quad y_k = \frac{y_b + y_a}{2} + \eta_k \frac{y_b - y_a}{2}.$$

The placement of nodes at the Gauss-Lobatto locations for spectral elements of order $p = 2$ to $p = 5$ is illustrated in Figure 8. On moving regularly spaced nodes to the Gauss-Lobatto locations within each element, oscillation in the interpolation of smooth data (Runge phenomenon) is suppressed.[14] A nodal interpolant is formed using tensor-product Lagrange polynomials, which allow polynomials of order p to be reproduced over $\mathcal{T}$. These polynomial interpolants are termed FE shape functions and are typically computed in a canonical element over the domain $\Xi = [-1, 1]^2$. Letting $\boldsymbol{x} := (x, y) \in \Omega_e$ and $\boldsymbol{\xi} := (\xi, \eta) \in \Xi$, the affine transformation from $\boldsymbol{\xi} \mapsto \boldsymbol{x}$ is

$$x(\xi) = \frac{x_b + x_a}{2} + \xi \frac{x_b - x_a}{2}, \quad y(\eta) = \frac{y_b + y_a}{2} + \eta \frac{y_b - y_a}{2},$$

with its inverse map also being affine. In Ξ, the shape function associated with the node at (ξ_j, η_k) has the form

$$N_{jk}(\boldsymbol{\xi}) = \left(\frac{\xi - \xi_1}{\xi_j - \xi_1} \right) \cdots \left(\frac{\xi - \xi_{j-1}}{\xi_j - \xi_{j-1}} \right) \left(\frac{\xi - \xi_{j+1}}{\xi_j - \xi_{j+1}} \right) \cdots \left(\frac{\xi - \xi_{p+1}}{\xi_j - \xi_{p+1}} \right)$$
$$\left(\frac{\eta - \eta_1}{\eta_k - \eta_1} \right) \cdots \left(\frac{\eta - \eta_{k-1}}{\eta_k - \eta_{k-1}} \right) \left(\frac{\eta - \eta_{k+1}}{\eta_k - \eta_{k+1}} \right) \cdots \left(\frac{\eta - \eta_{p+1}}{\eta_k - \eta_{p+1}} \right). \tag{20}$$

These considerations allow for very high-order approximation spaces, and the resulting FE methods are generally referred to as spectral element methods.

4.3 | Enrichment for holes and material interfaces

The X-FEM is an instance of the partition-of-unity finite element method,[6] which provides a means to include known solution characteristics in the approximation space. This is accomplished by augmenting the standard FE space with the product of PU functions and enrichment functions. In this paper, we choose FE basis functions as the PU functions, though other choices with desirable properties are also available.

Even though the X-FEM can be used to model a domain that contains both holes and material interfaces, to simplify the exposition, we treat each problem separately. In Sections 4.3.1 and 4.3.2, we detail the specific enrichment functions used to model holes and material interfaces, respectively.
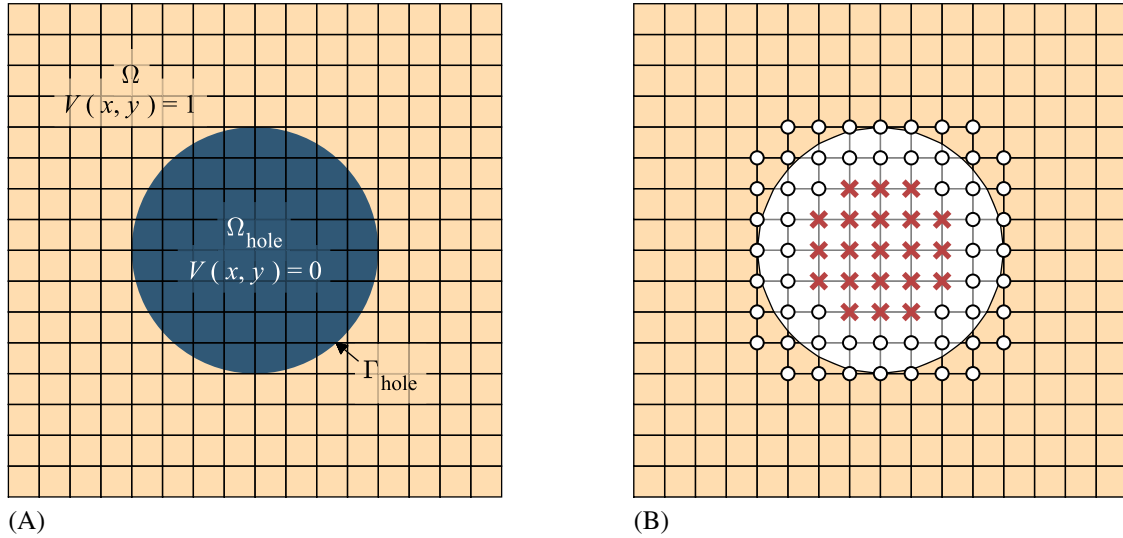
FIGURE 9 Modeling a void with the extended finite element method. (A) Enrichment function for a circular void, and (B) enriched degrees of freedom (DOFs) (circles) and removed DOFs (crosses) in the vicinity of a void for bilinear finite elements [Colour figure can be viewed at wileyonlinelibrary.com]

4.3.1 | Modeling of holes

The location of Γ_{hole} is defined implicitly through the curve $\varphi(\boldsymbol{x}) = 0$, where $\varphi(\boldsymbol{x})$ is a level set function that is greater than zero when $\boldsymbol{x} \in \Omega$, less than zero when $\boldsymbol{x} \in \Omega_{\text{hole}}$, and equal to zero when $\boldsymbol{x}$ is on Γ_{hole}. Level set functions for various scenarios are given in Section 2.

To capture the effect of holes on the FE approximation, we construct an enrichment function based on the level set description of the void geometry as follows:[3,69]

$$V(\boldsymbol{x}) = \begin{cases} 1 & \text{if } \varphi(\boldsymbol{x}) \geq 0 \\ 0 & \text{if } \varphi(\boldsymbol{x}) < 0 \end{cases} \quad \forall \boldsymbol{x} \in \overline{\Omega \cup \Omega_{\text{hole}}}. \tag{21}$$

The enrichment function $V(\boldsymbol{x})$ for the level set function that is illustrated in Figure 3 is plotted in Figure 9A. The choice of either $\varphi(\boldsymbol{x})$ or $\varphi^h(\boldsymbol{x})$ in (21) is valid. Choosing $\varphi(\boldsymbol{x})$ allows the geometry of the hole to be exactly represented, but will yield the same rate of convergence as selecting $\varphi^h(\boldsymbol{x})$.

For an element in which $\Omega_e \cap \Omega_{\text{hole}} \neq \emptyset$, the extended FE approximation of the displacement field $\boldsymbol{u}(\boldsymbol{x}) : \bar{\Omega} \to \mathbb{R}^2$ is[69]

$$\boldsymbol{u}_e^h(\boldsymbol{x}) = \sum_{i \in \mathbb{I}_e} N_i(\boldsymbol{x}) V(\boldsymbol{x}) \boldsymbol{u}_i, \tag{22}$$

where $\boldsymbol{u}_i$ are the nodal displacement DOFs. Based on the location of Γ_{hole} with respect to Ω_e, two cases are possible.

1. $\Omega_e \cap \Gamma_{\text{hole}} = \emptyset$: the entirety of Ω_e is located in Ω_{hole}.
2. $\Omega_e \cap \Gamma_{\text{hole}} \neq \emptyset$: a portion of Ω_e is located in Ω while the remainder is located in Ω_{hole}.

For case 1, $\boldsymbol{u}(\boldsymbol{x})$ is zero in the entire element. For case 2, $\boldsymbol{u}(\boldsymbol{x})$ is discontinuous across Γ_{hole}. Note that, if case 1 occurs, there may exist nodes that have no FE basis function support. An illustration of this scenario is shown in Figure 9B. The DOFs at these nodes (the ones that contain crosses in Figure 9B) are removed during the solution procedure.

4.3.2 | Modeling material interfaces

Similar to the case of modeling holes with the X-FEM, we can leverage the level set method to simplify locating and reconstructing Γ_{mat}. For material inclusions, the level set function, $\varphi^h(\boldsymbol{x})$, is greater than zero when $\boldsymbol{x} \in \Omega_1$, is less than zero when $\boldsymbol{x} \in \Omega_2$, and is equal to zero when $\boldsymbol{x}$ is on Γ_{mat}. In an element that intersects the material interface, ie, $\Omega_e \cap \Gamma_{\text{mat}} \neq \emptyset$,
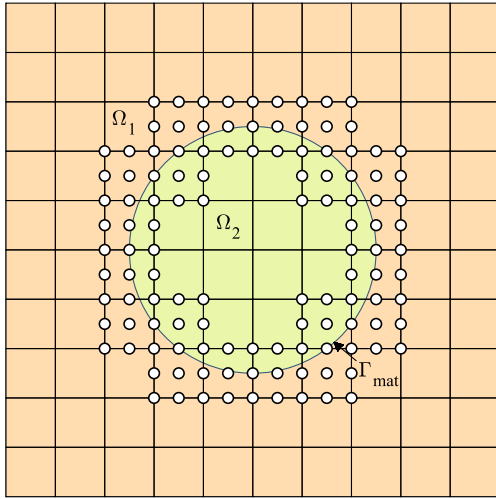
FIGURE 10 Two-phase composite material. Enriched nodes are marked with an open circle [Colour figure can be viewed at wileyonlinelibrary.com]

the extended FE approximation takes the form[3]

$$
\boldsymbol{u}_e^h(\boldsymbol{x}) = \underbrace{\sum_{i \in \mathbb{I}_e} N_i(\boldsymbol{x}) \boldsymbol{u}_i}_{\text{standard FE}} + \underbrace{\sum_{j \in \mathbb{J}_e \subseteq \mathbb{I}_e} N_j(\boldsymbol{x}) \psi(\boldsymbol{x}) \boldsymbol{a}_j}_{\text{enriched contribution}}, \tag{23}
$$

where $\psi(\boldsymbol{x})$ is the enrichment function and $\mathbb{J}_e$ is the index set of nodes belonging to Ω_e whose basis function support intersects Γ_{mat}. A schematic of a two-phase composite (circular interface) that is modeled using a quadratic FE mesh is depicted in Figure 10. In Figure 10, all the enriched nodes are shown as open circles.

To model material interfaces using the X-FEM, the normal strain must admit a jump that satisfies the Hadamard compatibility condition at the interface between two dissimilar isotropic materials. Sukumar et al[3] exploited the level set function to devise an enrichment function $\psi(\boldsymbol{x}) = |\varphi^h(\boldsymbol{x})|$ (henceforth termed the abs-enrichment) that is discontinuous normal to $\varphi^h(\boldsymbol{x}) = 0$; however, this choice of the enrichment function cannot reproduce affine fields on both sides of a rectilinear interface due to the presence of nonzero enrichment in (blending) elements adjacent to the material interface. Moës et al[10] introduced a modification of the absolute value function (hereafter referred to as the modified abs-enrichment)

$$
\psi(\boldsymbol{x}) = \sum_{i \in \mathbb{I}_e} N_i(\boldsymbol{x}) |\varphi_i| - |\varphi^h(\boldsymbol{x})|, \tag{24}
$$

where we recall $\varphi_i := \varphi(\boldsymbol{x}_i)$. In the modified abs-enrichment, the second term is the negative of the enrichment from the work of Sukumar et al.[3] The first term is a smooth field, which guarantees all nodal values of the enrichment function are zero—even nodal values inside an element. Their sum produces a function that is weakly discontinuous across the interface and is a smooth polynomial function elsewhere. This function is nonzero only on elements that intersect Γ_{mat} and yields optimal convergence rates for bimaterial interface problems with bilinear FEs ($p = 1$). However, for higher-order FEs, the approximation space cannot reproduce pth-order polynomials on both sides of the interface (as proved in Section 4.3.3) and optimal rates are not retained using this enrichment.[9]

In one dimension, two desirable features of the material interface enrichment function are as follows:

1. linear, ridge-like variation near the material interface, which is displayed by $|\varphi(\boldsymbol{x})|$, and
2. zero-value outside enriched elements to avoid the effects of blending elements.

If the enrichment function is not affine, the space of polynomial functions that can be reproduced is affected (see Section 4.3.3 for details). The modified abs-enrichment in one dimension for linear and quadratic elements is presented in Figure 12. The abs-enrichment only possesses the first feature, whereas the modified abs-enrichment has both features for $p = 1$ but retains only the second feature for $p \geq 2$.

We seek to reproduce both these features with an enrichment function that is also valid in two- and three-dimensional domains. Note that the modified abs-enrichment reproduces both these features for linear elements in two dimensions and three dimensions. To reproduce this behavior in higher-order elements, we propose an enrichment function similar in
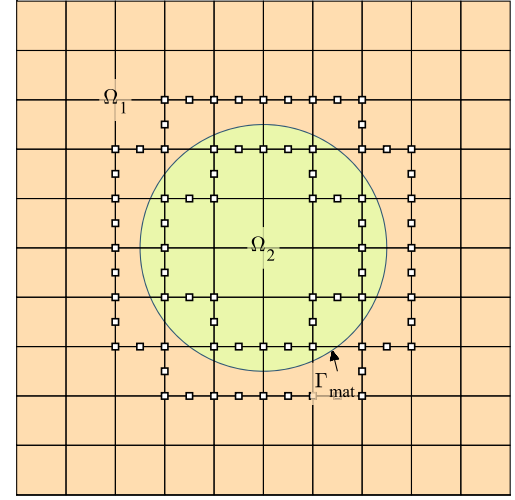
FIGURE 11 Nodes in $\mathbb{I}_{\text{zero}}$ (marked by open squares) on a 10×10 quadratic finite element mesh [Colour figure can be viewed at wileyonlinelibrary.com]

form to the modified abs-enrichment, but different in one crucial respect. Instead of being zero-valued at all nodal values (as is the case with the modified abs-enrichment), we only require nodal values to be zero at nodes on the boundary of the enriched region. In the modified abs-enrichment, zero-value of the enrichment function at nodes is enforced through the first term of (24). We propose a modification to this term, by enforcing zero-value only on the nodes located on the boundary of the enriched region. On a higher-order quadrilateral element, the remaining nodal values are set to the required value to reproduce a bilinear field, based on nodal values at the four corners of the element. A more formal statement of the proposed enrichment function follows.

Over the element tessellation $\mathcal{T}$, let $\mathbb{I}_{\text{enr}}$ be the set consisting of nodes that are enriched, ie, the nodal basis function support of these nodes intersects Γ_{mat} (nodes marked by circles in Figure 10). We define $\mathbb{I}_{\text{zero}}$ as the subset of $\mathbb{I}_{\text{enr}}$ with enriched nodes that belong to elements that do not intersect Γ_{mat} (see Figure 11). The material interface enrichment function is set to zero at these nodes. For a point $\boldsymbol{x} \in \Omega_e$, we define the function

$$g^h(\boldsymbol{x}) = \sum_{i \in \mathbb{I}_e} N_i(\boldsymbol{x})g_i, \tag{25}$$

where g_i are nodal values. For the modified-abs enrichment, $g_i = |\varphi_i|$; however, in the proposed enrichment function, g_i are set by a two-step process.

1. For nodes $i \in \mathbb{I}_{\text{zero}}$, set $g_i = |\varphi_i|$, and for all other nodes set $g_i = 0$.
2. Then, for nodes not at the vertices of the element and in $\mathbb{I}_{\text{enr}} \setminus \mathbb{I}_{\text{zero}}$, set $g_i = \sum_{j=1}^{4} N_j^{(p=1)}(\boldsymbol{x}_i)g_j$, where $N_j^{(p=1)}(\boldsymbol{x})$ are the bilinear FE shape functions and g_j are the element vertex values of g that are set in step 1.

Using (25), we define our material interface enrichment function as

$$\psi(\boldsymbol{x}) = g^h(\boldsymbol{x}) - |\varphi^h(\boldsymbol{x})| \quad \forall \boldsymbol{x} \in \Omega_e. \tag{26}$$

In (26), the second term introduces the ridge with discontinuous derivative at Γ_{mat}, whereas the first term shifts the second term to be zero-valued on the appropriate boundaries and approximates a smoothly interpolated bilinear function elsewhere. In one dimension, our enrichment function is presented in Figure 12. The proposed enrichment function retains a linear ridge shape for $p > 1$ and vanishes on the boundary of the enriched element. Even though Figure 12 illustrates that the proposed enrichment or $p = 2$ matches the modified abs-enrichment for $p = 1$ in one dimension, in two (and higher) dimensions, the two enrichment functions are distinct. In Figure 13, the proposed enrichment function for a circular inclusion over quadratic elements is plotted.

We set the unknown DOFs of g based on bilinear interpolation of the nodal values at the vertices; however, other choices are also possible. For example, one could choose coefficients for g by minimizing the second derivatives of $g(\boldsymbol{x})$ normal to Γ_{mat}, which may improve the approximation, especially in higher-order elements ($p \geq 3$). Finally, we note the shape of the enrichment function is strongly influenced by the nature of $\varphi(\boldsymbol{x})$. The enrichment function should approximate a
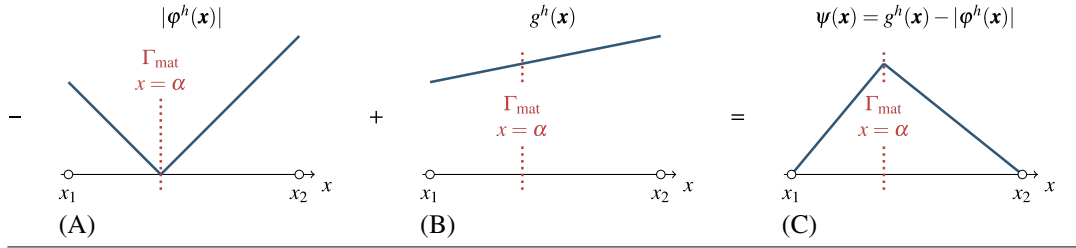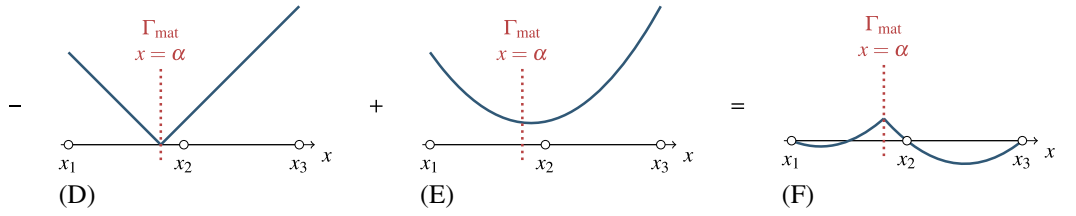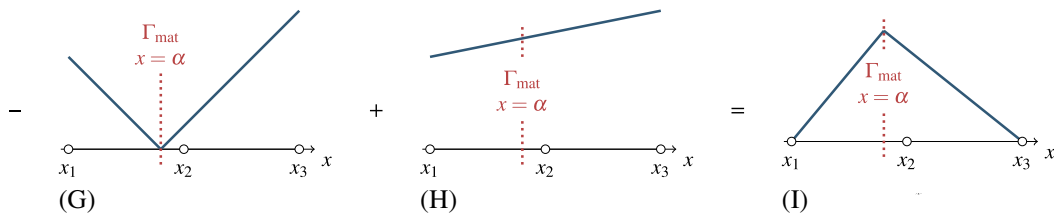
Modified abs-enrichment and proposed enrichment, $p = 1$

$|\varphi^h(x)|$ $\qquad$ $g^h(x)$ $\qquad$ $\psi(x) = g^h(x) - |\varphi^h(x)|$

$-$ (A) $\qquad$ $+$ (B) $\qquad$ $=$ (C)

Modified abs-enrichment, $p = 2$

$-$ (D) $\qquad$ $+$ (E) $\qquad$ $=$ (F)

Proposed enrichment, $p = 2$

$-$ (G) $\qquad$ $+$ (H) $\qquad$ $=$ (I)

FIGURE 12 (A)-(C) Both the modified abs-enrichment and the proposed enrichment over a one-dimensional linear element. (D)-(F) Modified abs-enrichment and (G)-(I) the proposed enrichment over a one-dimensional quadratic element. The enrichment functions are computed as the sum of $-|\varphi^h(x)|$ in (A), (D), and (G) with $g^h(x)$ in (B), (E), and (H). Their sum is shown in (C) for a linear element, in (F) for the modified-abs enrichment on a quadratic element, and in (I) for the proposed enrichment on a quadratic element [Colour figure can be viewed at wileyonlinelibrary.com]

ridge function to recover pth-order polynomial approximation on both sides of the material interface (see the analysis in Section 4.3.3). However, a ridge function is reproduced in (26) only if the level set function is a multiple of the distance function. We investigate the consequences of choosing a level set function that is not the distance function in the section that follows and via an example in Section 6.6.

4.3.3 | Approximation properties for material interface problems

One dimension: In one dimension, the proposed enrichment function reduces to a ridge function (see Figure 12I). For an enriched approximation space, we assert that two arbitrary pth degree polynomials that meet with C^0 continuity at the material interface can be exactly reproduced. However, even in one dimension, it is not readily apparent that this holds, and hence, we now present a proof of this assertion.

Proof. In an enriched element $\Omega_e = [x_1, x_{p+1}]$ with nodes $\mathbb{I}_e = \{1, \ldots, p+1\}$, we define the polynomial

$$u(x) = \begin{cases} u_-(x), & x_1 \leq x \leq \alpha \\ u_+(x), & \alpha < x \leq x_{p+1}, \end{cases} \tag{27a}$$

where

$$u_-(x) = \sum_{k=1}^{p} b_k(x - \alpha)^k + d, \quad u_+(x) = \sum_{k=1}^{p} c_k(x - \alpha)^k + d. \tag{27b}$$

In (27), b_k and c_k ($k = 1, \ldots, p$) are $2p$ (known) coefficients, $\alpha \in \Omega_e$ is the location of the interface, and $d = u_-(\alpha) = u_+(\alpha)$. Note that $u_-(x)$ and $u_+(x)$ are two pth degree polynomials that are equal at $x = \alpha$, but otherwise arbitrary. The
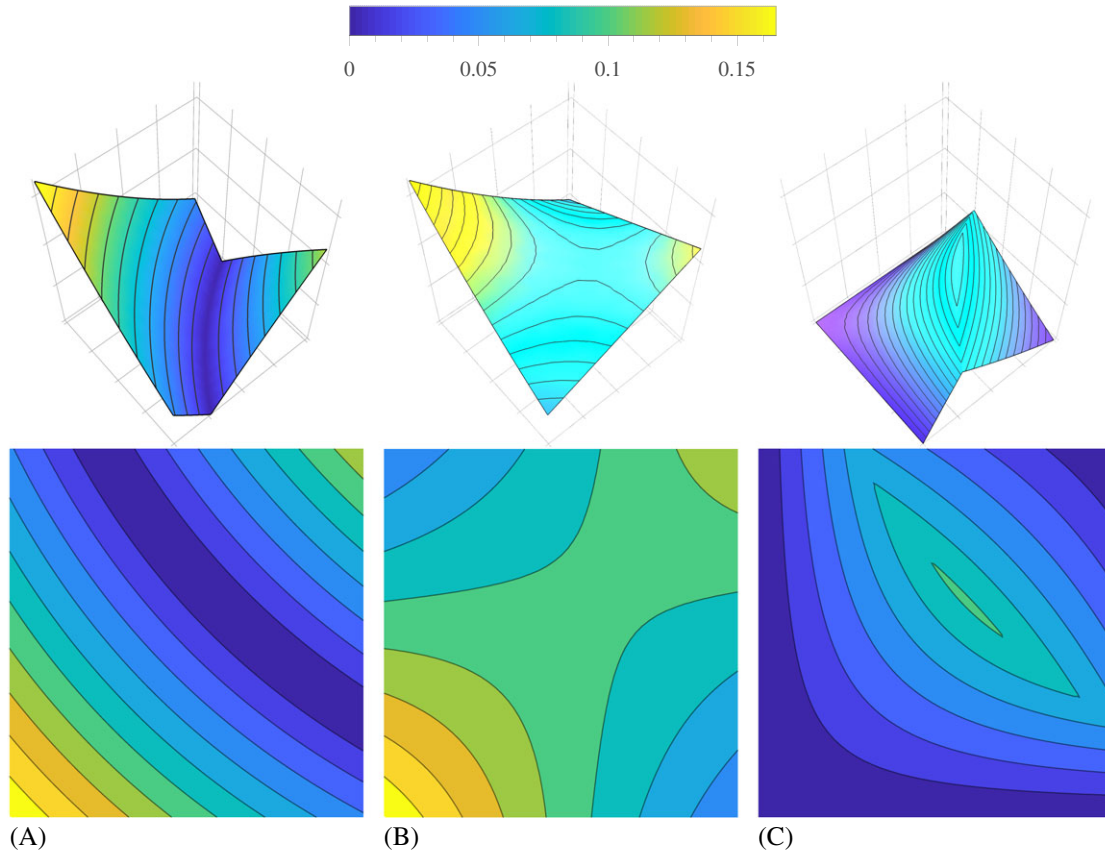
FIGURE 13 Construction of the enrichment function, $\psi(\mathbf{x})$, for the material interface problem on a quadratic finite element mesh ($p = 2$). The plots are on the element domain $\Omega_e = (-0.4, -0.2)^2$, with $\varphi(\mathbf{x}) = \|\mathbf{x}\| - 0.4$. A, $|\varphi^h(\mathbf{x})|$; B, $g(x)$; C, $\psi(\mathbf{x}) = g(x) - |\varphi^h(x)|$

coefficients b_k, c_k, and d provide $2p + 1$ parameters to uniquely define $u_-(x)$ and $u_+(x)$. The polynomials in (27) can also be expressed as

$$u_-(x) = \sum_{k=0}^{p} \tilde{b}_k(x - \alpha)^k + \frac{x - x_1}{\alpha - x_1} \sum_{k=0}^{p-1} \tilde{c}_k(x - \alpha)^k, \quad u_+(x) = \sum_{k=0}^{p} \tilde{b}_k(x - \alpha)^k + \frac{x_{p+1} - x}{x_{p+1} - \alpha} \sum_{k=0}^{p-1} \tilde{c}_k(x - \alpha)^k, \tag{28}$$

where $\tilde{b}_k$ ($k = 0, \ldots, p$) and $\tilde{c}_k$ ($k = 0, \ldots, p-1$) are $2p+1$ coefficients shared between $u_-(x)$ and $u_+(x)$. The coefficients $\tilde{b}_k$ and $\tilde{c}_k$ are related to b_k, c_k, and d as follows:

$$\tilde{c}_k = \frac{(b_{k+1} - c_{k+1})(\alpha - x_1)(x_{p+1} - \alpha)}{x_{p+1} - x_1},$$

$$\tilde{b}_0 = d - \tilde{c}_0, \quad \tilde{b}_k = \frac{c_k(x_{p+1} - \alpha) + b_k(\alpha - x_1)}{x_{p+1} - x_1} - \tilde{c}_k \quad (k = 1, \ldots, p-1), \quad \tilde{b}_p = \frac{c_p(x_{p+1} - \alpha) + b_p(\alpha - x_1)}{x_{p+1} - x_1}.$$

In (28), the first summation of $u_-(x)$ and $u_+(x)$ represents a pth degree polynomial, whereas the second summation is a $(p - 1)$th degree polynomial multiplied by a ridge function,

$$\tilde{\psi}(x) = \begin{cases} \psi_-(x), & x_1 \leq x \leq \alpha \\ \psi_+(x), & \alpha < x \leq x_{p+1} \\ 0, & \text{otherwise}, \end{cases} \tag{29a}$$

where

$$\psi_-(x) = \frac{x - x_1}{\alpha - x_1}, \quad \psi_+(x) = \frac{x_{p+1} - x}{x_{p+1} - \alpha}. \tag{29b}$$

The ridge function is unity at $x = \alpha$ and decreases linearly to zero at $x = x_1$ and $x = x_{p+1}$. Using (29a), (28) can be written as

$$u_-(x) = f_p(x) + \psi_-(x)g_{p-1}(x), \quad u_+(x) = f_p(x) + \psi_+(x)g_{p-1}(x), \tag{30}$$

where $f_p(x)$ and $g_{p-1}(x)$ are polynomials of degree p and $p - 1$, respectively.

The enriched FE approximation in Ω_e is

$$u_e^h(x) = \begin{cases} u_-^h(x), & x_1 \leq x \leq \alpha \\ u_+^h(x), & \alpha < x \leq x_{p+1}, \end{cases} \tag{31a}$$

where

$$u_-^h(x) = \sum_{i=1}^{p+1} N_i(x)u_i + \psi_0\psi_-(x)\sum_{i=1}^{p+1} N_i(x)a_i, \quad u_+^h(x) = \sum_{i=1}^{p+1} N_i(x)u_i + \psi_0\psi_+(x)\sum_{i=1}^{p+1} N_i(x)a_i. \tag{31b}$$

In (31), the constant ψ_0 is the amplitude of the enrichment function at $x = \alpha$, and u_i and a_i are nodal coefficients. Since $\psi(x)$ is an affine function, the second summation in $u_-^h(x)$ and $u_+^h(x)$ is in general a polynomial of degree $p + 1$. To eliminate the coefficient that multiplies x^p, we introduce a constraint on the system

$$\sum_{i=1}^{p+1} \frac{a_i}{(x_i - x_1)\cdots(x_i - x_{i-1})(x_i - x_{i+1})\cdots(x_i - x_{p+1})} = 0. \tag{32}$$

Since a pth-order FE basis uniquely defines a polynomial of degree p and the FE basis constrained by (32) uniquely defines a polynomial of degree $p - 1$, it is possible to choose coefficients u_i and a_i to match the polynomials $f_p(x)$ and $g_{p-1}(x)$. Selecting $u_i := f_p(x_i)$ and $a_i := g_{p-1}(x_i)/\psi_0$, we recover

$$\sum_{i=1}^{p+1} N_i(x)u_i = \sum_{i=1}^{p+1} N_i(x)f_p(x_i) = f_p(x), \quad \psi_0\sum_{i=1}^{p+1} N_i(x)a_i = \sum_{i=1}^{p+1} N_i(x)g_{p-1}(x_i) = g_{p-1}(x), \tag{33}$$

and hence, the assertion is established. □

If the enrichment function $\psi(x)$ is a polynomial of degree greater than 1 (as with the modified abs-enrichment), additional constraints would be required on the coefficients a_i to ensure that the resulting approximation $u_e^h(x)$ is of degree p. However, these additional constraints result in fewer than $2p + 1$ unique coefficients remaining in (31) to define the approximation. As established above, $2p + 1$ parameters are needed to uniquely define the polynomials in (27).

Two dimensions: Having established the connection between the extended FE approximation using the bimaterial enrichment function and the reproduction of arbitrary polynomial functions in one dimension, we now turn to the two-dimensional case. We can gain a better understanding of the enriched approximation space in two dimensions through use of the L^2 minimization procedure used in Section 4.1 in the work of Chin et al.[51] Consider the biunit square $\Omega = [-1, 1]^2$, which contains a weak discontinuity across the interface located along the implicitly defined line $\varphi(\mathbf{x}) = (y - x)/\sqrt{2} - \frac{1}{4} = 0$. We note that $\varphi(\mathbf{x})$ is also a signed distance function from the interface. Let $u(\mathbf{x}) : \Omega \to \mathbb{R}$ be a scalar-valued polynomial of degree two that has a discontinuous derivative across $\varphi(\mathbf{x}) = 0$

$$u(\mathbf{x}) = \begin{cases} -(x - y)^2 + 2(x - y) + \frac{13 + 3\sqrt{2}}{4}, & \varphi(\mathbf{x}) \leq 0 \\ (x - y)^2 - (x - y) + 3, & \varphi(\mathbf{x}) > 0. \end{cases} \tag{34}$$

We seek the best approximation of $u(\mathbf{x})$ using a single quadratic ($p = 2$) extended FE approximation

$$u_e^h(\mathbf{x}) = \sum_{i \in \mathbb{I}_e} N_i(\mathbf{x})u_i + \sum_{j \in \mathbb{J}_e} \psi(\mathbf{x})N_j(\mathbf{x})a_j.$$
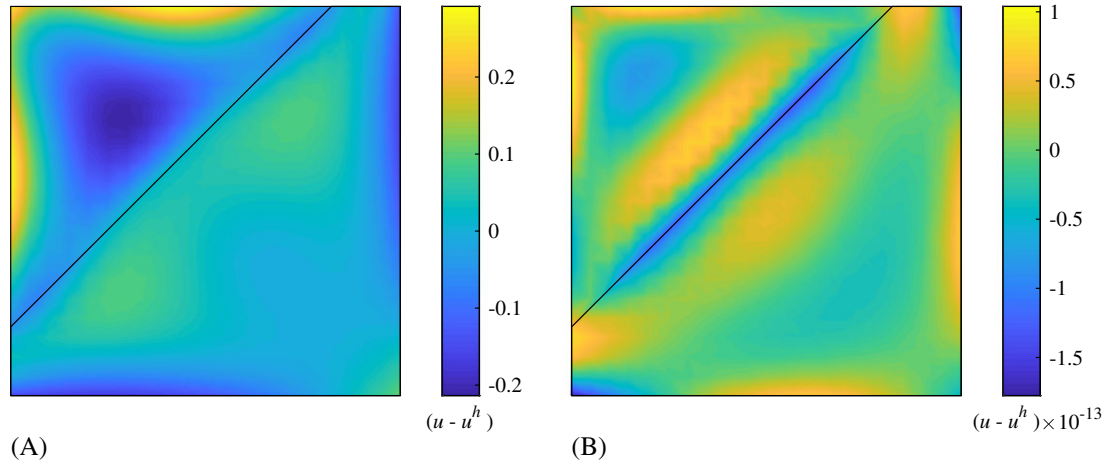
FIGURE 14 Error between $u(\boldsymbol{x})$ and $u_e^h(\boldsymbol{x})$, the best extended finite element approximation to $u(\boldsymbol{x})$ in $\mathbb{U}^h$, with the level set function equal to the signed distance function. (A) Modified-abs enrichment function[10] and (B) proposed enrichment function

Let $\mathbb{U}^h$ be the extended FE space. If $u(\boldsymbol{x}) \in \mathbb{U}^h$, then the best approximation in $\mathbb{U}^h$ should exactly reproduce $u(\boldsymbol{x})$.

The best approximation to $u(\boldsymbol{x})$ is obtained by determining the L^2 projection of $u(\boldsymbol{x})$ on $\mathbb{U}^h$. The coefficients $\boldsymbol{d} := \{\boldsymbol{u}, \boldsymbol{a}\}$ are obtained as the solution of the linear system: $\boldsymbol{Md} = \boldsymbol{f}$, where entries of the mass matrix $\boldsymbol{M}$ and force vector $\boldsymbol{f}$ are

$$M_{ij} = \int_\Omega \tilde{N}_i(\boldsymbol{x})\tilde{N}_j(\boldsymbol{x})\ dA, \quad f_i = \int_\Omega \tilde{N}_i(\boldsymbol{x})u(\boldsymbol{x})\ dA,$$

where $\tilde{N}_i(\boldsymbol{x}) = N_i(\boldsymbol{x})$ for standard DOFs and $\tilde{N}_i(\boldsymbol{x}) = \psi(\boldsymbol{x})N_i(\boldsymbol{x})$ for enriched DOFs. The evaluation of $\boldsymbol{M}$ and $\boldsymbol{f}$ requires integrating weakly discontinuous polynomials. For integration, we split the domain at the location of the interface, then use the HNI method to integrate the polynomials that are present on either side of the weak discontinuity. The error $u - u^h$ using the modified abs-enrichment ranges from about $+0.3$ to -0.2, as shown in Figure 14A. On the other hand, using the proposed enrichment function, $u - u^h$ reduces to $\mathcal{O}(10^{-13})$, which is close to machine precision. Based on these findings, we observe that the enrichment function proposed in (26) can reproduce weakly discontinuous polynomial functions in two dimensions when the level set function matches the signed distance function.

To reveal the consequences of choosing a level set function that is not a signed distance function, we now select

$$\varphi(\boldsymbol{x}) = \left(\frac{y-x}{\sqrt{2}}\right)^2 + 3\left(\frac{y-x}{\sqrt{2}}\right) - \frac{13}{16} \tag{35}$$

to represent the same interface. The function $u(\boldsymbol{x})$ defined in (34) is retained. The spatial error between $u(\boldsymbol{x})$ and $u^h(\boldsymbol{x})$ is displayed in Figure15A for the modified abs-enrichment function and in Figure15B for the new enrichment function. Maximum error using the modified abs-enrichment increases to over 0.35, while maximum error in the best L^2 approximation increases to approximately 0.02 using the proposed enrichment—considerably higher than the $\mathcal{O}(10^{-13})$ error observed when the signed distance function is selected as the level set function.

In the circular inclusion (curved interface) problem in Section 6.6, a nonpolynomial signed distance function is used for the level set function. As a result, some error is introduced due to the (polynomial) FE interpolation of the signed distance function. With h-refinement of the mesh, error in the polynomial approximation of the signed distance function reduces, and therefore, this source of error does not affect the rate of convergence of the method. Additionally, as $h \to 0$, the signed distance function approaches an affine interface, akin to the example in this section. To obtain optimal rates of convergence when solving a boundary-value problem, pth-order polynomial reproduction is sufficient on both sides of the interface. On affine interfaces, this behavior is observed with the proposed enrichment when used in conjunction with a signed distance function. Since pth-order polynomial reproduction on both sides of an affine interface is not retained with the modified abs-enrichment, suboptimal rates of convergence are obtained, as observed in the work of Cheng and Fries[9] and also verified in our own studies.
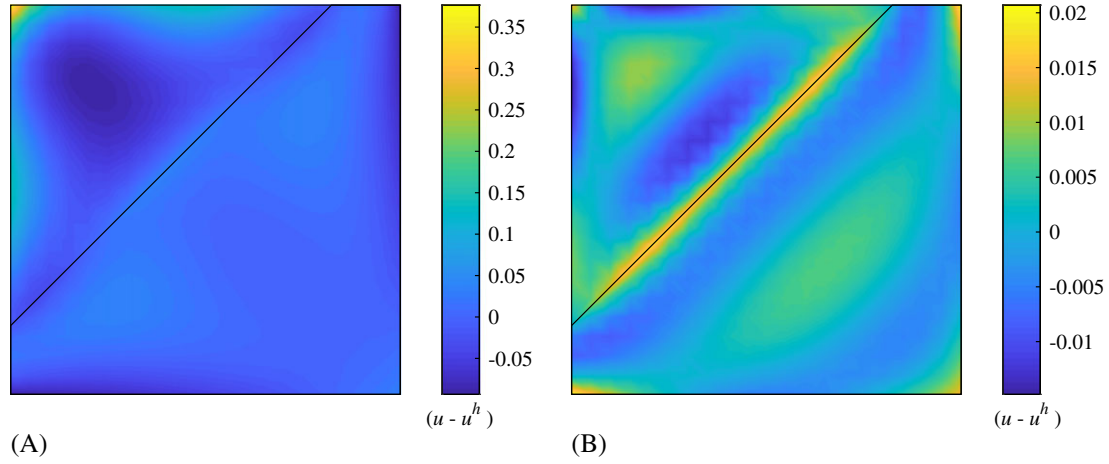
FIGURE 15 Error between $u(\boldsymbol{x})$ and $u_e^h(\boldsymbol{x})$, the best extended finite element approximation to $u(\boldsymbol{x})$ in $\mathbb{U}^h$, with the level set function in (35). (A) Modified-abs enrichment function[10] and (B) proposed enrichment function

4.4 | Discrete equations

For the hole problem, choosing (22) to form the displacement field $\boldsymbol{u}(\boldsymbol{x})$ and the virtual displacement field $\delta\boldsymbol{u}(\boldsymbol{x})$ in (19) and then using the arbitrariness of nodal variations, we obtain the element level quantities

$$\boldsymbol{K}_e = \int_{\Omega_e \cap \Omega} (\boldsymbol{B}_u(\boldsymbol{x}))^T \boldsymbol{D}(\boldsymbol{x}) \boldsymbol{B}_u(\boldsymbol{x})\, d\boldsymbol{x}, \quad \boldsymbol{f}_e = \int_{\Omega_e \cap \Omega} (\boldsymbol{N}_u(\boldsymbol{x}))^T \boldsymbol{b}(\boldsymbol{x})\, d\boldsymbol{x} + \int_{\Gamma_e \cap \Gamma_t} (\boldsymbol{N}_u(\boldsymbol{x}))^T \bar{\boldsymbol{t}}(\boldsymbol{x})\, dS, \tag{36}$$

where Γ_e is the boundary of Ω_e and $\boldsymbol{D}(\boldsymbol{x})$ is the piecewise constant two-dimensional linear elastic constitutive matrix. In addition, $\boldsymbol{N}_u(\boldsymbol{x})$ is the standard element shape function vector and

$$\boldsymbol{B}_\alpha(\boldsymbol{x}) = \left[\boldsymbol{B}_\alpha^1(\boldsymbol{x})\ \boldsymbol{B}_\alpha^2(\boldsymbol{x}) \cdots \boldsymbol{B}_\alpha^{|\mathbb{L}|}(\boldsymbol{x}) \right], \tag{37}$$

where $\alpha = u, \mathbb{L} = \mathbb{I}_e$, and

$$\boldsymbol{B}_u^\ell(\boldsymbol{x}) = \begin{bmatrix} N_{\ell,x}(\boldsymbol{x}) & 0 \\ 0 & N_{\ell,y}(\boldsymbol{x}) \\ N_{\ell,y}(\boldsymbol{x}) & N_{\ell,x}(\boldsymbol{x}) \end{bmatrix}. \tag{38}$$

When $\Omega_e \cap \Omega \neq \Omega_e$, the region of integration does not coincide with the element, and ==standard tensor-product Gauss cubature fails to yield satisfactory results.==

For the material interface problem, choosing (23) to represent $\boldsymbol{u}(\boldsymbol{x})$ and $\delta\boldsymbol{u}(\boldsymbol{x})$ in (19), and using a standard Galerkin procedure, we obtain the following element quantities:

$$\boldsymbol{K}_e = \int_{\Omega_e} \begin{bmatrix} (\boldsymbol{B}_u(\boldsymbol{x}))^T \boldsymbol{D}(\boldsymbol{x}) \boldsymbol{B}_u(\boldsymbol{x}) & (\boldsymbol{B}_u(\boldsymbol{x}))^T \boldsymbol{D}(\boldsymbol{x}) \boldsymbol{B}_a(\boldsymbol{x}) \\ (\boldsymbol{B}_a(\boldsymbol{x}))^T \boldsymbol{D}(\boldsymbol{x}) \boldsymbol{B}_u(\boldsymbol{x}) & (\boldsymbol{B}_a(\boldsymbol{x}))^T \boldsymbol{D}(\boldsymbol{x}) \boldsymbol{B}_a(\boldsymbol{x}) \end{bmatrix} d\boldsymbol{x},$$

$$\boldsymbol{f}_e = \int_{\Omega_e} [\boldsymbol{N}_u(\boldsymbol{x}) \boldsymbol{N}_a(\boldsymbol{x}) \psi(\boldsymbol{x})]^T \boldsymbol{b}(\boldsymbol{x})\, d\boldsymbol{x} + \int_{\Gamma_e \cap \Gamma_t} [\boldsymbol{N}_u(\boldsymbol{x}) \boldsymbol{N}_a(\boldsymbol{x}) \psi(\boldsymbol{x})]^T \bar{\boldsymbol{t}}(\boldsymbol{x})\, dS, \tag{39}$$

where $\boldsymbol{B}_\alpha(\boldsymbol{x})$ for $\alpha = u, a$ is defined in (37), and $\boldsymbol{N}_a(\boldsymbol{x})$ is the element shape function vector for nodes in $\mathbb{J}_e$. Referring to (37), for $\alpha = a$ and $\mathbb{L} = \mathbb{J}_e$, we define

$$\boldsymbol{B}_a^\ell(\boldsymbol{x}) = \begin{bmatrix} (N_\ell(\boldsymbol{x})\psi(\boldsymbol{x}))_{,x} & 0 \\ 0 & (N_\ell(\boldsymbol{x})\psi(\boldsymbol{x}))_{,y} \\ (N_\ell(\boldsymbol{x})\psi(\boldsymbol{x}))_{,y} & (N_\ell(\boldsymbol{x})\psi(\boldsymbol{x}))_{,x} \end{bmatrix}. \tag{40}$$

Weak (strain) discontinuities due to $\psi(\boldsymbol{x})$ and strong discontinuity of $\boldsymbol{D}(\boldsymbol{x})$ across Γ_{mat} result in the integrands in (39) being discontinuous, rendering tensor-product Gauss cubature ill-suited to handle integration.

Assembling element level quantities using the FE assembly procedure, the discrete linear system of equations, $Kd = f$, is obtained. Element-level integration over elements intersected by holes and over discontinuous integrands is conducted using the HNI method, which requires homogeneous integrands. We elaborate on the homogeneous functions that make up these integrands in Section 4.5. Details of the integration procedure are described in Section 5.

4.5 | Homogeneous functions in the X-FEM

The integrands introduced in Section 4.4 consist of vectors and matrices with discontinuous polynomial terms. Since a polynomial is a linear combination of homogeneous monomials, the integrands in (36) and (39) are all compatible with the HNI method provided we subdivide the integration regions into ones that contain continuous integrands.

Specifically, $D(x)$ is a constant in Ω_1 and Ω_2 and is therefore a homogeneous function of degree $q = 0$. The shape functions for a pth-order spectral FE are polynomial functions of degree $q = 2p$. For example, with $p = 2$, the ith shape function can be decomposed to

$$N_i^{p=2}(x) = N_i^{[0]} + N_i^{[1]}(x) + N_i^{[2]}(x) + N_i^{[3]}(x) + N_i^{[4]}(x),$$

where the bracketed superscript refers to the degree of homogeneity of the polynomial. The matrix $B_\alpha(x)$ contains derivatives of the shape functions, which are polynomials of degree $q = 2p - 1$. Since $\psi(x)$ is computed using shape functions, the enrichment function is a linear combination of homogeneous functions. Finally, since $b(x)$ must be integrated over the element, we require the body force to be either a homogeneous function or decomposable into homogeneous functions.

For the integrands in (36) and (39), products of these homogeneous terms of a polynomial are computed. Special care is taken to ensure the product remains homogeneous. This process is simplified by computing $P = a_1 \otimes a_2$, where a_1 and a_2 are vectors containing the homogeneous terms of a polynomial. The matrix P is assigned to a new vector of homogeneous terms via the entries of a Hankel matrix with appropriate values.

4.6 | Conditioning of the stiffness matrix

The extended FE approximation for holes and material inclusions can induce high condition number in the global FE stiffness matrix, which can lead to reduced accuracy when solving the algebraic system of linear equations.[70] The reason for poor matrix conditioning is distinct in the hole problem versus the material inclusion problem. For voids, elements where $\Omega_e \cap \Omega$ is very small compared to Ω_e cause very small regions of support in some DOFs. These ultimately result in modes of deformation with much lower stiffness when compared to others, resulting in an ill-conditioned system of linear equations. In the material inclusion problem, conditioning issues arise when $\Omega_e \cap \Omega_1$ or $\Omega_e \cap \Omega_2$ is very small compared to Ω_e. This causes the approximation space of the enriched DOFs to be similar to the approximation space of unenriched DOFs, causing near linear dependence in the linear system of equations. A summary of methods to improve conditioning in the X-FEM is discussed in the work of de Prenter et al.[71] Two of these methods are implemented in the results presented in Section 6.

1. A Jacobi preconditioner that normalizes the diagonal of the stiffness matrix.[72]
2. An additional term in the weak form called a *ghost penalty*[16,52] that provides coercivity over the computational domain for the hole problem.

A Jacobi preconditioner is a method to improve a badly scaled matrix that is otherwise well conditioned. The implementation of the preconditioner is as follows. For the linear system of equations $Kd = f$, we make the substitution $d = D\tilde{d}$ where D is the inverse of the square root of the main diagonal of K, ie, $D = \text{diag}(K)^{-1/2}$. Rather than solving the original system of equations, we instead solve $\left(D^T K D\right) \tilde{d} = D^T f$, where $\left(D^T K D\right)$ is a modified stiffness matrix with all ones on the diagonal. Examples of the effect of the preconditioner on the condition number of the stiffness matrix are provided in Sections 6.1, 6.2, and 6.5.

The ghost penalty term is designed to eliminate the influence of very small cut elements on the condition number of the stiffness matrix. The term adds an additional stiffness contribution to DOFs that have some support in Ω_{hole}, which minimally changes the FE solution. We establish the set of elements in Ω and the set of cut elements as

$$\mathcal{T}_a = \{ T_i \ : \ T_i \in \mathcal{T}, \Omega_i \cap \Omega \neq \emptyset \}, \quad \mathcal{T}_c = \{ T_i \ : \ T_i \in \mathcal{T}_a, \Omega_i \cap \Omega \neq \Omega_i \},$$
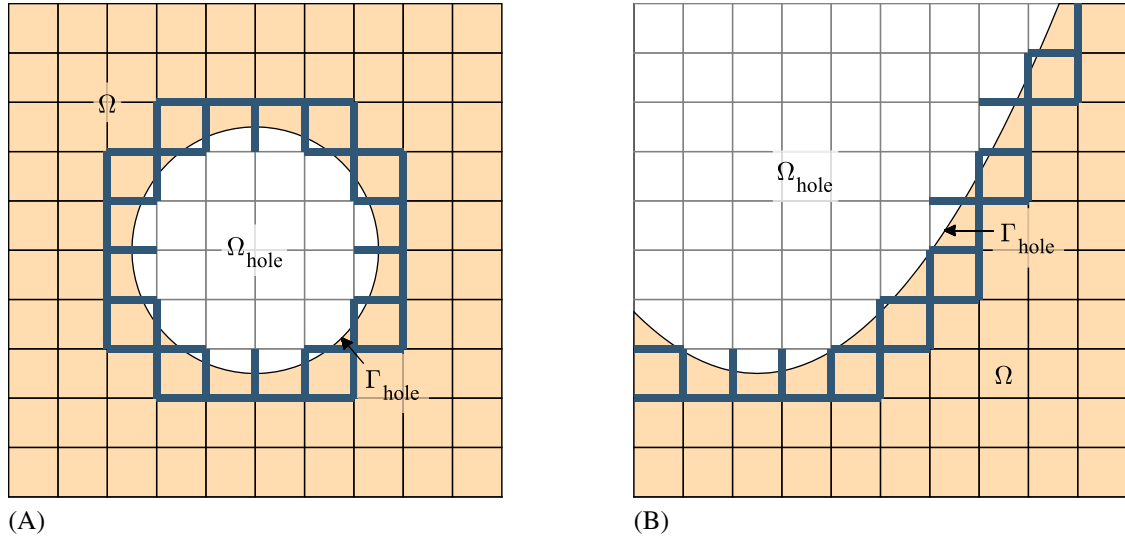
FIGURE 16 Illustrating the set of edges $\mathcal{F}$ on which the ghost penalty stabilization term is computed. Edges in $\mathcal{F}$ are bold. The element tessellation, $\mathcal{T}$, is a 10×10 mesh of square elements [Colour figure can be viewed at wileyonlinelibrary.com]

where T_i is the ith element in $\mathcal{T}$ with domain Ω_i. Additionally, we define a set of edges

$$\mathcal{F} = \left\{ F = T_i \cap T_j \ : \ T_i \in \mathcal{T}_a, T_j \in \mathcal{T}_c \right\}$$

for $i, j = 1, \ldots, M$. The set of edges $\mathcal{F}$ is demonstrated for two domains in Figure 16. Following the work of Sticko et al,[17] the supplemental weak form term in (19) is

$$j(\boldsymbol{u}, \delta\boldsymbol{u}) = \beta \sum_{F \in \mathcal{F}} \sum_{k=1}^{p} \frac{h^{2k-1}}{(2k+1)(k!)^2} \int_F \left[\partial_{\boldsymbol{n}}^k \boldsymbol{u}\right] \left[\partial_{\boldsymbol{n}}^k \delta\boldsymbol{u}\right] dS, \tag{41}$$

where $\boldsymbol{n}$ denotes a unit vector normal to F, $\beta = \gamma(\lambda + 2\mu)$, γ is a parameter that sets the magnitude of the ghost penalty, λ and μ are the Lamé parameters for the material, p is the order of the FE approximation, and h is the average characteristic element length for the two elements connected to F. The bracket $[\cdot]$ is used to represent the difference of its argument evaluated over the elements attached to F. Note the computation of (41) is simplified since we use a Cartesian mesh that is aligned with the Cartesian axes. The ghost penalty contribution penalizes derivative discontinuities over element edges. The effectiveness of the ghost penalty term is evaluated for an example in Section 6.1.

5 | INTEGRATION OF DISCONTINUOUS POLYNOMIALS

Polynomials are integrated accurately and efficiently using Gauss cubature. However, integration accuracy is severely compromised by lack of smoothness (discontinuous or piecewise-continuous polynomials) in the integrand. To improve integration accuracy of discontinuous polynomial integrands that arise in the X-FEM for holes and material discontinuities, we employ the HNI method. For elements with continuous integrands, tensor-product Gauss cubature is used. The HNI scheme requires a three-step approach.

1. Subdivide the element at Γ_{mat} or Γ_{hole} into two regions separated by a curved section that follows Γ_{mat} or Γ_{hole}.
2. Develop a cubature rule for the region in Ω (hole problem) and for both regions for the material interface problem.
3. Carry out cubature using (14) for affine edges and (16) over curved sections.

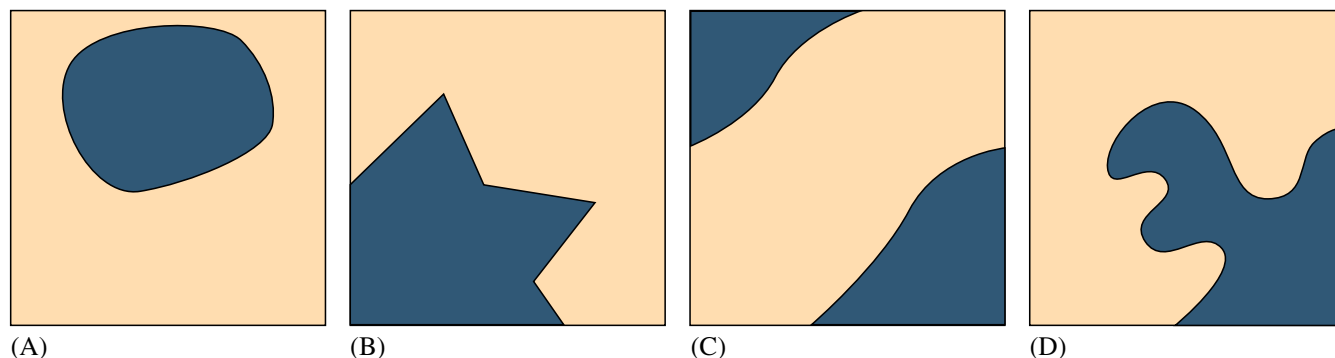We describe the details for each of the three steps in the remainder of this section.

FIGURE 17 Examples of regions on which integration can be performed using the homogeneous numerical integration method without the need for mesh refinement. (A) An element that wholly contains an interface, (B) an element cut by an interface with sharp points, (C) an element cut in multiple locations, and (D) an element cut by a complicated interface with high curvature [Colour figure can be viewed at wileyonlinelibrary.com]

5.1 | Element subdivision and interface reconstruction

To identify elements cut by Γ_{hole} or Γ_{mat}, the level set function is first evaluated at all the nodes. Based on the value of the level set function, the nodes are either assigned as inside the level set geometry, on the level set zero (within a prescribed tolerance close to machine precision), or outside the level set geometry. Elements that have at least one node inside the geometry and at least one node outside the geometry are considered as cut elements. These cut elements are subdivided at the interface (either Γ_{hole} or Γ_{mat}), recovering smooth, polynomial integrands within each subelement. Cubature points lie on the boundary using the HNI method; therefore, within these cut elements, the interface must be obtained in closed form to define the boundary of regions of integration on either side of the interface. Whether the interface is reconstructed exactly or approximately is dependent on how the level set geometry is described. Four methods for representing Γ_{hole} are used in this paper, which are covered in Section 2. For material interface problems, Γ_{mat} is only reconstructed using the procedure described in Section 2.3. This provides consistency with the enrichment function, which is also constructed using the FE interpolant.

The use of the HNI scheme simplifies interface reconstruction, even for very complicated scenarios such as a level set geometry completely contained in a single element, sharp features in level set isocontours, level set curves entering and exiting an element multiple times, or curved regions with high curvature in elements. Scenarios such as sharp corners can occur, for example, when multiple level set functions are used in one element—a scenario the HNI scheme is capable of handling. Examples of these complicated level set functions are illustrated in Figure 17. The process of interface reconstruction is simplified over these complex geometries since element tessellation is not required for purposes of integration. For spectral X-FEM, the ability to correctly account for these types of features is crucial to retaining optimal convergence behavior in the method.

In the following two examples, we numerically investigate the behavior of the interface reconstruction scheme presented in Section 2.2 by computing the area of regions defined as the intersection of a square domain, Ω, and an implicitly defined domain, $\varphi(\boldsymbol{x}) > 0$. Curved portions of the boundary of the region coincide with the zero isocontour of the level set function. In all examples, the zero isocontour is approximated using G^1 interpolatory optimized cubic Hermite functions. The area of the approximated region is determined using the HNI method. Since Hermite functions are polynomial, cubature of the approximate geometry is exact using an appropriate Gauss rule. In the first example, the interfaces $\varphi(\boldsymbol{x}) = 0$ are polynomial curves, and in the second example, the interfaces include a conic section and nonpolynomial curves.

5.1.1 | Example: integration error versus ϵ with polynomial curve interfaces

We wish to compute the area of the region defined as the intersection of a square domain $\Omega = [-1, 1]^2$ and an implicit region defined by $\varphi(\boldsymbol{x}) > 0$, where $\varphi(\boldsymbol{x}) = 0$ is a polynomial curve. A cubic Hermite curve can provide an exact representation for polynomial curves up to degree three. We verify this property in this example and examine the number of iterations needed for convergence using the minimization procedure outlined in Section 2.2. When the degree of a polynomial curve is greater than three, we investigate the convergence properties of the integration error in computing the

p	θ	b_0	b_1	b_2	b_3	Iterations	$e(\boldsymbol{m}^*)$	Integration error
1	$-\frac{3\pi}{4}$	1	-2	0	0	0	7.4×10^{-17}	6.8×10^{-17}
2	$-\frac{\pi}{4}$	$-\frac{3}{4}$	$-\frac{1}{3}$	4	0	3	5.2×10^{-17}	0
3	$\frac{\pi}{6}$	$-\frac{1}{4}$	-1	$\frac{1}{5}$	1	13	1.1×10^{-16}	2.2×10^{-16}

TABLE 1 Iterations to generate the optimal cubic Hermite curve to approximate a polynomial curve, estimated error in the approximation, $e(\boldsymbol{m}^*)$, and integration error in computing the area of the regions partially bounded by the polynomial curve (see Figure 18 for illustrations of the regions)

(A) (B) (C)
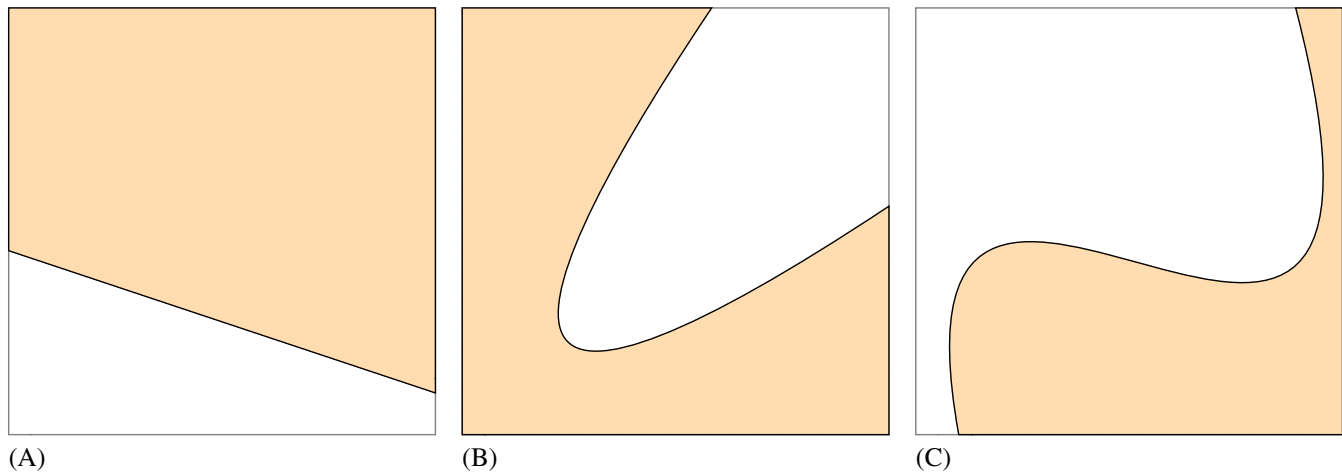
FIGURE 18 Example regions of integration defined as $\Omega \cap \{\varphi(\boldsymbol{x}) > 0\}$, where $\varphi(\boldsymbol{x}) = 0$ is a polynomial curve. (A) $p = 1$, (B) $p = 2$, and (C) $p = 3$ [Colour figure can be viewed at wileyonlinelibrary.com]

area versus increasing cubic Hermite curve approximations to the polynomial curve. To generate a level set isocontour that is a polynomial curve, we choose the level set function

$$\varphi(\boldsymbol{x}) = \sum_{k=0}^{p} b_k \bar{x}^k - \bar{y}, \qquad (42)$$

where $\bar{x} = x \cos \theta + y \sin \theta$, $\bar{y} = -x \sin \theta + y \cos \theta$, and θ is the counterclockwise angle of rotation from x to $\bar{x}$.

For $p \leq 3$, we select values of θ and b_k that correspond to linear, quadratic, and cubic curves, then generate the cubic Hermite function that minimizes the objective function in (6). In the minimization procedure, the BFGS algorithm is used to approximate the Hessian of the objective function. Using this optimized cubic Hermite spline, we then compute the estimated error $e(\boldsymbol{m}^*)$ in (7) and the error in computing the area of intersection of $\Omega = [-1, 1]^2$ and $\varphi(\boldsymbol{x}) \geq 0$. Values of $e(\boldsymbol{m}^*)$, error in area calculation, and number of iterations to convergence for the values of θ and parameters b_k tested are presented in Table 1. Illustrations of the three regions defined by the level set functions are provided in Figure 18. The linear curve is reproduced exactly, with no iterations required. This is expected since the curve is uniquely defined by its endpoints. The quadratic and cubic curves require 3 and 13 iterations, respectively, to arrive at the optimal curve. For both curves, both $e(\boldsymbol{m}^*)$ and integration error are near machine precision. These results reveal that the cubic Hermite function can exactly reproduce these curves.

Cubic Hermite parametric curves cannot reproduce polynomial curves that are degree $p > 3$. However, multiple cubic Hermite curves can be used to reduce the error of the approximation, as measured by $e(\boldsymbol{m}^*)$. We select two implicit polynomial curves to test: one quartic and one quintic. The level set function follows the form of (42), and the coefficients and θ are listed in Figure 19A for the quartic curve and in Figure 20A for the quintic curve. For five different values of ϵ (10^{-4}, 10^{-6}, 10^{-8}, 10^{-10}, and 10^{-12}), we tabulate the number of cubic Hermite curve segments required and the error in computing the area of the region of integration. The regions of integration, distribution of cubic Hermite curves for $\epsilon = 10^{-8}$, integration error versus ϵ, and integration error versus the number of curve segments are presented in Figure 19 and in Figure 20 for the quartic curve and quintic curve, respectively. The distribution of Hermite parametric curves along the implicitly defined boundary is not equal since additional Hermite curves are placed adaptively in regions where $e(\boldsymbol{m}^*) > \epsilon$. In these two examples, integration error and ϵ are approximately equal, revealing the relationship between $e(\boldsymbol{m}^*)$ and integration error. The rate of convergence with additional curve segments ranges between $R = 5$ and $R = 6$. This is an improvement when compared to C^2 cubic Hermite splines, which have a convergence rate of $R = 4$.

| p	θ	b_0	b_1	b_2	b_3	b_4
4	$\frac{\pi}{3}$	$-\frac{1}{8}$	1	$\frac{1}{4}$	$-\frac{1}{2}$	2

(A)
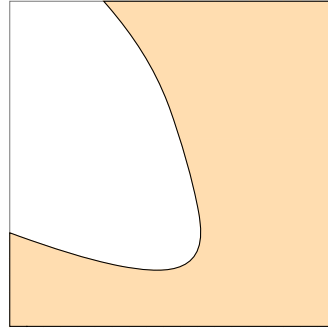
(B)
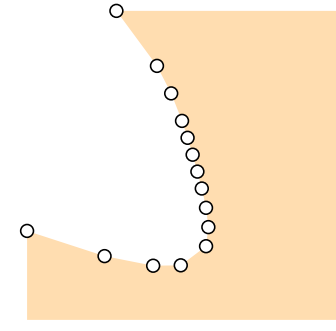
(C)

FIGURE 19 Computing the area of a region bounded by a quartic polynomial curve of the form (42). (A) Coefficients of the polynomial, (B) region of integration defined as $\Omega \cap \{\varphi(\boldsymbol{x}) > 0\}$, (C) cubic Hermite curve endpoints for $\epsilon = 10^{-8}$, (D) integration error in computing the area of the region versus ϵ, and (E) integration error in computing the area of the region versus number of curve segments [Colour figure can be viewed at wileyonlinelibrary.com]
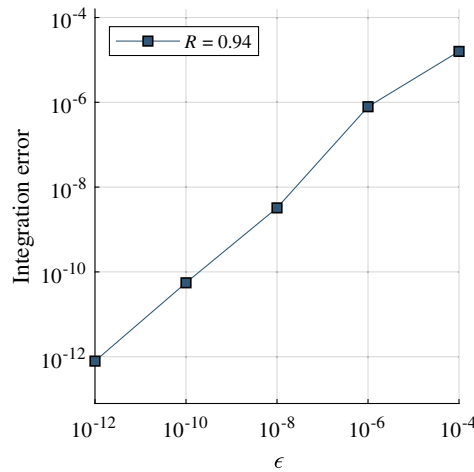
(D)
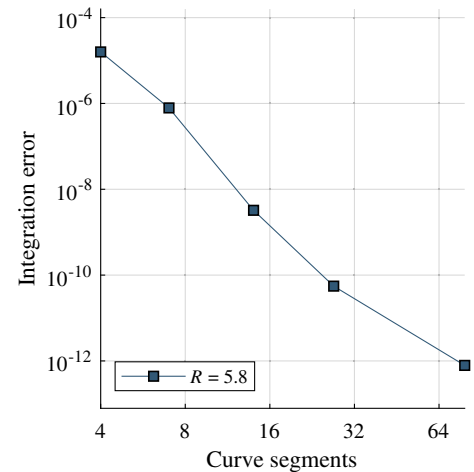
(E)

5.1.2 | Example: integration error versus ϵ with other interfaces

In this example, we compute the area of the regions pictured in Figure 21, which consist of squares cut by a propeller (Figure 21A), a circle (Figure 21B), and a sine wave (Figure 21C). The location of Ω and the level set functions that are used to generate the curved portion of the boundary are listed in Table 2. For the circular region, the curved interface is a conic section and for the propeller and the sine wave, the curved interface is a trigonometric function. Since polynomial curves such as the cubic Hermite function cannot reproduce these curved interfaces, we instead measure how the parameter ϵ and the number of curves used to approximate the interface compare to the error in measuring the area of the region. Note that rational Bézier curves can reproduce conic sections exactly (see Section 2.1), but they cannot reproduce nonpolynomial curves. As in the previous example, five values of ϵ are selected: 10^{-4}, 10^{-6}, 10^{-8}, 10^{-10}, and 10^{-12}. We plot integration error versus the parameter ϵ and integration error versus the number of cubic Hermite functions used to approximate the level set zero isocontour in Figure 22. We observe from Figure 22A that the parameter ϵ and the integration error in computing the area of the region are approximately equal. In addition, Figure 22B shows that the integration error with increasing curve segments converges at a rate of $R = 5.6$ for the propeller example to a rate of $R = 6.5$ for the sine wave example.
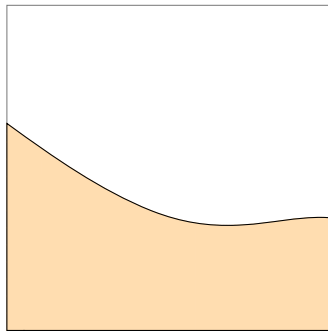
5.2 | Cubature rule with the HNI method
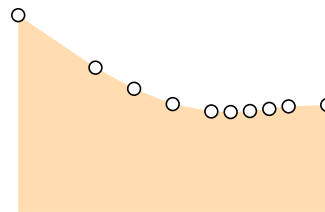
We desire a cubature rule of the form

$$\int_{\Omega_e} h(\boldsymbol{x})\, d\boldsymbol{x} \approx \sum_{i=1}^{nq} h(\boldsymbol{x}_i) w_i, \tag{43}$$

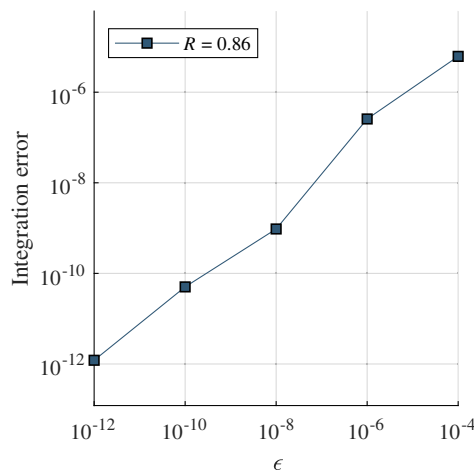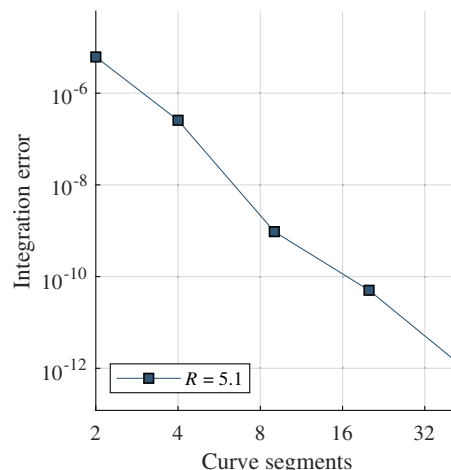| p	θ	b_0	b_1	b_2	b_3	b_4	b_5
5	$\frac{\pi}{4}$	$-\frac{1}{2}$	-1	1	-2	3	-4

(A)

(B)

(C)

(D)

(E)

FIGURE 20 Computing the area of a region bounded by a quintic polynomial curve of the form (42). (A) Coefficients of the polynomial, (B) region of integration defined as $\Omega \cap \{\varphi(\boldsymbol{x}) > 0\}$, (C) cubic Hermite curve endpoints for $\epsilon = 10^{-8}$, (D) error in computing area of the region versus ϵ, and (E) error in computing area of the region versus number of curve segments [Colour figure can be viewed at wileyonlinelibrary.com]

where nq is the total number of cubature points, $\{\boldsymbol{x}_i\}_{i=1}^{nq}$ are the cubature points, and $\{w_i\}_{i=1}^{nq}$ are the cubature weights. We combine (13), (14), and (16) to recover an integration rule of this form for a homogeneous function over Ω_e. However, since the integrands for the X-FEM are generally the sum of multiple homogeneous functions of varying degree, we instead choose to remove the portions of the cubature rule that are dependent on the degree of homogeneity of the homogeneous functions. This permits generation of a single cubature rule that is applicable to all the homogeneous terms in the integrand. To separately handle the case of the affine interface and the parametric interface, we split (43)

$$\int_{\Omega_e} h(\boldsymbol{x}) \, d\boldsymbol{x} = I_{\text{affine}} + I_{\text{parametric}}, \tag{44}$$

where I_{affine} is the integral contribution from affine edges and $I_{\text{parametric}}$ is the integral contribution from curved sections described by parametric curves (we refer to these as parametric edges).

Consider a function $h(\boldsymbol{x}) = f_1(\boldsymbol{x}) + f_2(\boldsymbol{x}) + \cdots + f_{nh}(\boldsymbol{x})$ that is the sum of nh homogeneous functions, where the degree of the homogeneous function $f_i(\boldsymbol{x})$ is q_i. Let the boundary be composed of n affine edges and $m - n$ parametric edges. On the affine edges, we can combine (13) and (14) and introduce the terms in $h(\boldsymbol{x})$ to obtain

$$I_{\text{affine}} = \sum_{j=1}^{nh} \frac{1}{2 + q_j} \sum_{i=1}^{n} \frac{b_i}{\|\boldsymbol{a}_i\|} \int_{F_i} f_j(\boldsymbol{x}) \, d\sigma. \tag{45}$$
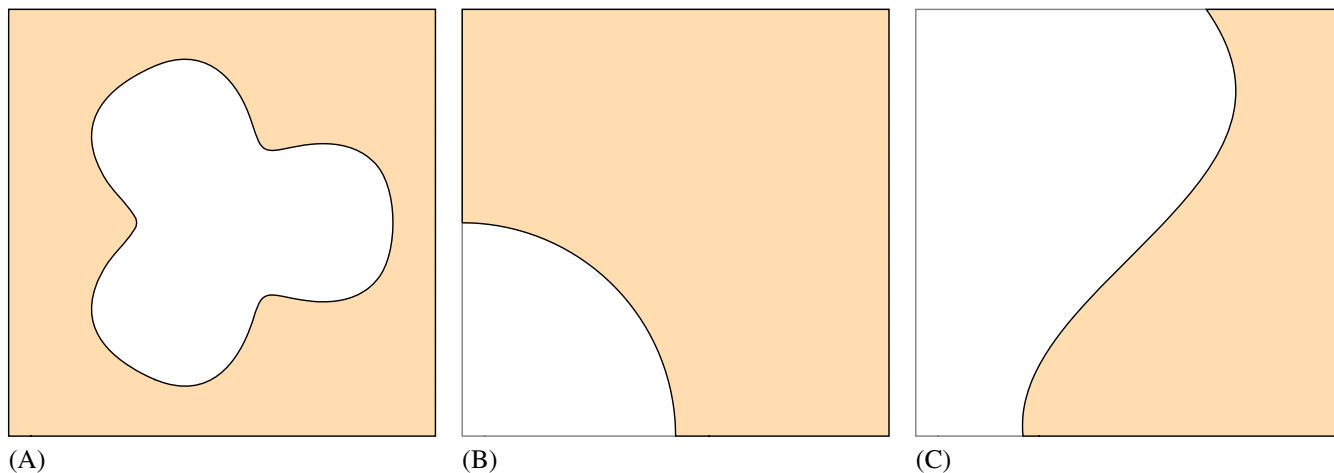
FIGURE 21 Example regions of integration defined as $\Omega \cap \{\varphi(\boldsymbol{x}) > 0\}$. (A) Propeller: a biunit square, $\Omega = [-1, 1]^2$, cut by a level set function defined in polar coordinates, $\varphi(r, \theta) = r + \frac{2}{5}\sin^4(\frac{3}{2}\theta) - \frac{4}{5}$. (B) Circle: a square, $\Omega = [0, 1]^2$, intersected with the level set function $\varphi(\boldsymbol{x}) = \|\boldsymbol{x}\| - 0.5$. (C) Sine wave: a biunit square, $\Omega = [-1, 1]^2$, cut by a low amplitude sinusoidal wave, $\varphi(\boldsymbol{x}) = x - \frac{1}{2}\sin(2y + \frac{1}{3})$ [Colour figure can be viewed at wileyonlinelibrary.com]

TABLE 2 Definitions for Ω and $\varphi(\boldsymbol{x})$ for regions of integration defined by nonpolynomial level set functions

Region	Ω	$\varphi(\boldsymbol{x})$ or $\varphi(r, \theta)$
Propeller	$[-1, 1]^2$	$r + \frac{2}{5}\sin^4\left(\frac{3}{2}\theta\right) - \frac{4}{5}$
Circle	$[0, 1]^2$	$\|\boldsymbol{x}\| - 0.5$
Sine wave	$[-1, 1]^2$	$x - \frac{1}{2}\sin\left(2y + \frac{1}{3}\right)$

FIGURE 22 Computing the area of a square cut by a semicircular hole (see Figure 21B) using the optimization procedure described in Section 2.2. (A) Integration error versus ϵ, and (B) cubic Hermite functions required to satisfy $e(\boldsymbol{m}^*) \leq \epsilon$ in all curve segments [Colour figure can be viewed at wileyonlinelibrary.com]
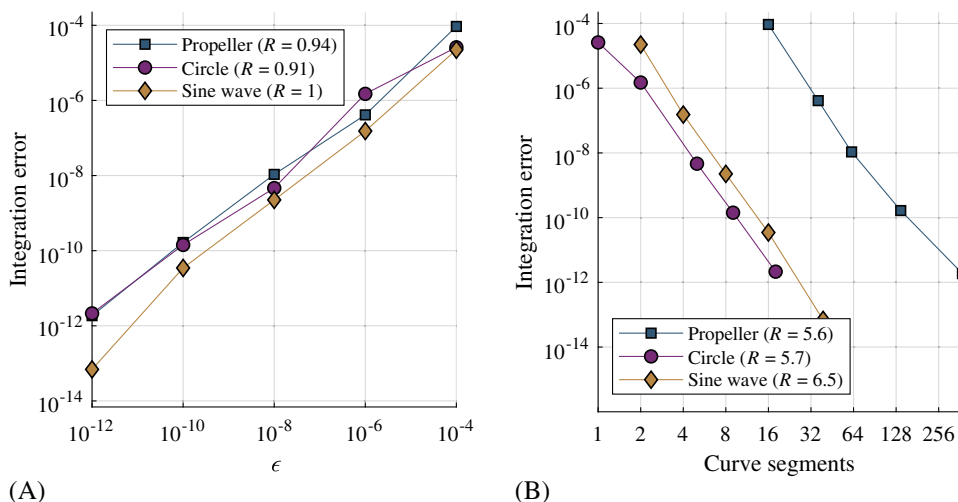
To compute the one-dimensional integral, $\int_{F_i} f_j(\boldsymbol{x})\,d\sigma$, we introduce a Gauss quadrature rule

$$\int_{F_i} f_j(\boldsymbol{x})\,d\sigma \approx \sum_{k=1}^{nq_{1D}} f_j(\boldsymbol{x}_k)\bar{w}_k,$$

where nq_{1D} is the number of quadrature points that is needed to accurately integrate $h(\boldsymbol{x})$. Combining the Gauss rule with (45), we obtain

$$I_{\text{affine}} \approx \sum_{\ell=1}^{nq_{\text{affine}}} \sum_{j=1}^{nh} \frac{1}{2 + q_j} f_j(\boldsymbol{x}_\ell)w_\ell, \tag{46}$$

where ℓ is an index that maps to a different unique values of (i, k) and $w_\ell = \bar{w}_k b_i / \|\boldsymbol{a}_i\|$.

On the $m - n$ parametric edges, (13) and (16) are combined

$$I_{\text{parametric}} = \sum_{j=1}^{nh} \frac{1}{2 + q_j} \sum_{i=1}^{m-n} \int_0^1 \left(c_i(t) \cdot \left(c_i'(t) \times e_3 \right) \right) f_j(c_i(t)) dt. \tag{47}$$

Since different parametric edges may have different integrands, each parametric edge is provided its own quadrature rule. On the ith parametric edge, we introduce a Gauss quadrature rule to compute the one-dimensional integral,

$$\int_0^1 \left(c_i(t) \cdot \left(c_i'(t) \times e_3 \right) \right) f_j(c_i(t)) dt \approx \sum_{k_i=1}^{nq_{1D}} \left(c_i(t_{k_i}) \cdot \left(c_i'(t_{k_i}) \times e_3 \right) \right) f_j \left(c_i(t_{k_i}) \right) \bar{w}_{k_i},$$

where nq_{1D} is the number of quadrature points required to evaluate the one-dimensional integral to sufficient accuracy. Including the quadrature rule in (47) and rearranging terms that appear, we obtain

$$I_{\text{parametric}} \approx \sum_{\ell=1}^{nq_{\text{parametric}}} \sum_{j=1}^{nh} \frac{1}{2 + q_j} f_j(x_\ell) w_\ell, \tag{48}$$

where ℓ maps to a quadrature point/weight on one of the parametric edges, $x_\ell = c_i(t_{k_i})$, and $w_\ell = (c_i(t_{k_i}) \cdot (c_i'(t_{k_i}) \times e_3)) \bar{w}_{k_i}$.

A cubature rule for the element is generated by combining I_{affine} and $I_{\text{parametric}}$, resulting in

$$\int_{\Omega_e} h(x) dx = \sum_{i=1}^{nq} \sum_{j=1}^{nh} \frac{1}{2 + q_j} f_j(x_i) w_i. \tag{49}$$

Positive cubature weights are a desirable feature of an integration rule, since they prevent loss of significant digits due to finite-precision arithmetic. To improve the number of positive weights in the final cubature rule, we choose the domain of integration to be the biunit square centered at the origin. The standard bilinear FE transformation is used to map points in the element domain to the biunit square. Integrating over $[-1, 1]^2$ results in positive weights for cubature points on the boundary of the domain, though cubature weights on curves may be negative depending on the location of the curve with respect to the origin. Additionally, integrating over the biunit square centered at the origin results in better scaling of the homogeneous terms, limiting loss of precision errors caused by positive and negative terms in the homogeneous expansion.

5.3 | Computation of element stiffness matrix and element force vector

In order to use the HNI method over a subdivision of Ω_e, homogeneous expansions of the quantities $B_u(x)$, $B_a(x)$, $N_u(x)$, $N_a(x)$, $\psi(x)$, and $b(x)$ are needed. The number of homogeneous terms in all of these expansions is dependent on the polynomial degree of the spectral FE. For a pth-order spectral element, we have the following homogeneous expansions:

$$\begin{aligned}
B_u(x) &= B_u^{[0]} + B_u^{[1]}(x) + \cdots + B_u^{[2p-1]}(x), \\
B_a(x) &= B_a^{[0]} + B_a^{[1]}(x) + \cdots + B_a^{[4p-1]}(x), \\
N_u(x) &= N_u^{[0]} + N_u^{[1]}(x) + \cdots + N_u^{[2p]}(x), \\
N_a(x) &= N_a^{[0]} + N_a^{[1]}(x) + \cdots + N_a^{[2p]}(x), \\
\psi(x) &= \psi^{[0]} + \psi^{[1]}(x) + \cdots + \psi^{[2p]}(x).
\end{aligned} \tag{50}$$

Inserting these homogeneous expansions into the stiffness matrix and force vector integrands for the hole problem given in (36), we obtain

$$K_e = \int_{\Omega_e} \left(B_u^{[0]} + B_u^{[1]}(x) + \cdots + B_u^{[2p-1]}(x) \right)^T D(x) \left(B_u^{[0]} + B_u^{[1]}(x) + \cdots + B_u^{[2p-1]}(x) \right) dx \tag{51a}$$

and

$$\boldsymbol{f}_e = \int_{\Omega_e} \left(\boldsymbol{N}_u^{[0]} + \boldsymbol{N}_u^{[1]}(\boldsymbol{x}) + \cdots + \boldsymbol{N}_u^{[2p]}(\boldsymbol{x}) \right)^T (\boldsymbol{b}^{[q_1]}(\boldsymbol{x}) + \cdots \boldsymbol{b}^{[q_{nq}]}(\boldsymbol{x})) \, d\boldsymbol{x}, \tag{51b}$$

where $\boldsymbol{b}(\boldsymbol{x})$ is a body force vector field that can be expanded into nq homogeneous functions. The cubature rule in (49) is applied to (51), which yields

$$\boldsymbol{K}_e \approx \sum_{i=1}^{nq} \left(\frac{\boldsymbol{K}_e^{[0]}}{2} + \frac{\boldsymbol{K}_e^{[1]}(\boldsymbol{x}_i)}{3} + \cdots + \frac{\boldsymbol{K}_e^{[4p-2]}(\boldsymbol{x}_i)}{4p} \right) w_i \tag{52a}$$

and

$$\boldsymbol{f}_e \approx \sum_{i=1}^{nq} \left(\frac{\boldsymbol{f}_e^{[q_1]}}{2+q_1}(\boldsymbol{x}) + \cdots + \frac{\boldsymbol{f}_e^{[2p+q_{nq}]}}{2+q_{nq}+2p} \right) w_i, \tag{52b}$$

where $\boldsymbol{K}_e^{[k]}(\boldsymbol{x}) = \sum_{i+j=k} (\boldsymbol{B}_u^{[i]}(\boldsymbol{x}))^T D^{[0]}(\boldsymbol{x}) \boldsymbol{B}_u^{[j]}(\boldsymbol{x})$ and $\boldsymbol{f}_e^{[k]}(\boldsymbol{x}) = \sum_{i+j=k} (\boldsymbol{N}_u^{[i]}(\boldsymbol{x}))^T \boldsymbol{b}^{[j]}(\boldsymbol{x})$. Similar equations are developed for the material interface problem from (39).

6 | NUMERICAL EXAMPLES

Several benchmark problems are chosen to demonstrate the efficacy of the HNI method to solve extended FE problems with holes and material interfaces under plane strain conditions. The extended FE code is developed using Matlab® R2018b. Unless stated otherwise, ghost penalty stabilization and the Jacobi preconditioner are used where applicable. In addition, rates of convergence are computed using linear regression of the three data points from the most refined meshes. Section 6.1 through Section 6.4 are for problems where the X-FEM is used to model holes in the domain. In Sections 6.5 and 6.6, we present several bimaterial problems that are modeled using the X-FEM. These examples are designed to illustrate various aspects of the implementation described in the previous sections of this paper.

6.1 | Uniaxial stress patch test

First, we investigate the effect of the ghost penalty term and the preconditioner through a uniaxial stress patch test. The region $(0, 2) \times (-1, 1)$ is discretized using a 2×2 FE mesh. The problem domain Ω is $(0, 1 + \Delta w) \times (-1, 1)$, resulting in a cut element on the right end of the mesh. A load of magnitude $\sigma_0 = 100$ is applied in the y-direction on the top and bottom edges of Ω. Symmetry boundary conditions about the y-axis are applied at $x = 0$, and the node at the origin is fixed. Material parameters are $E = 1000$ and $\nu = 0.3$. The configuration is illustrated in Figure 23A. The problem is solved with $\Delta w = 0.99, 0.1, 0.01, 0.001, 0.0001$, and 0.00001. Higher-order elements with $p = 1, 2, 3, 4$, and 5 are used. The problem is solved under three scenarios: with no stabilization, with a ghost penalty term, and lastly with ghost penalty and a Jacobi preconditioner. For the ghost penalty term, parametric studies indicate a parameter value of $\gamma = 0.01$ considerably reduces the condition number of the stiffness matrix while having minimal effect on solution accuracy for all values of p and Δw.

We investigate the effect of the ghost penalty term and the ghost penalty with preconditioner on the condition number of the stiffness matrix. The 2-norm condition number provides the exact maximum error magnification in the solution from finite precision inputs; however, since matrix norms are equivalent,[73] convergence behavior of the condition number can be investigated using any matrix norm. Accordingly, condition number is estimated using condest() in Matlab™, which estimates the 1-norm condition based on a technique by Hager.[74] With no stabilization, condition number increases rapidly as $\Delta w \to 0$. The effect worsens as p becomes larger. Condition number peaks at just below $\mathcal{O}(10^{20})$ for $p \geq 2$. With the ghost penalty term, the dependence of Δw on condition number is eliminated, with minimal change in condition number at $\Delta w \leq 10^{-2}$. Condition numbers range from $\mathcal{O}(10^3)$ for $p = 1$ to $\mathcal{O}(10^9)$ for $p = 5$. When the preconditioner is added to the ghost penalty term, condition numbers improve further, ranging from $\mathcal{O}(10^1)$ for $p = 1$ to $\mathcal{O}(10^8)$ for $p = 5$. Detailed results are presented in Figure 23.

6.2 | Plate with a circular hole

Consider an infinite plate with a hole of radius a that is centered at the origin. A far-field uniaxial stress, $\sigma_0 = 1$, is applied in the x-direction. An exact solution for this problem is available in the work of Szabó and Babuška.[75] The displacement
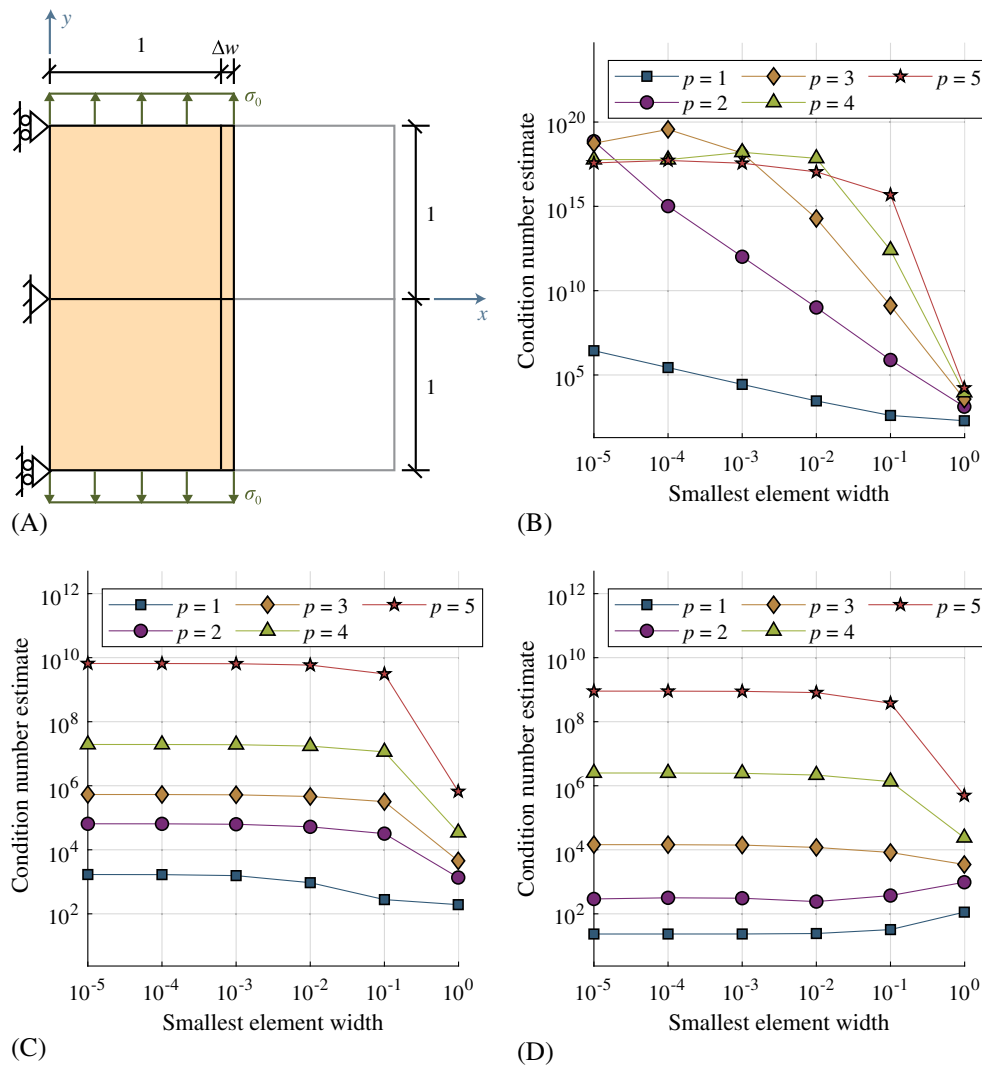
FIGURE 23 Uniaxial stress patch test with a cut edge. (A) Patch geometry, mesh, and boundary conditions, (B) cond (K) for different p and different Δw, (C) cond (K) with a ghost penalty term, and (D) cond (K) with ghost penalty and Jacobi preconditioning. A constant $\gamma = 0.01$ is chosen for all p [Colour figure can be viewed at wileyonlinelibrary.com]

field components in polar coordinates are

$$u_1(r,\theta) = \frac{a}{8\mu}\left[\frac{r}{a}(\kappa+1)\cos\theta + 2\frac{a}{r}((1+\kappa)\cos\theta + \cos 3\theta) - 2\frac{a^3}{r^3}\cos 3\theta\right],$$

$$u_2(r,\theta) = \frac{a}{8\mu}\left[\frac{r}{a}(\kappa-3)\sin\theta + 2\frac{a}{r}((1-\kappa)\sin\theta + \sin 3\theta) - 2\frac{a^3}{r^3}\sin 3\theta\right],$$

where μ is the shear modulus and κ is the Kolosov constant defined as

$$\kappa = \begin{cases} 3 - 4\nu & \text{for plane strain} \\ \frac{3-\nu}{1+\nu} & \text{for plane stress.} \end{cases}$$

The stress field is given by the components

$$\sigma_{11}(r,\theta) = 1 - \frac{a^2}{r^2}\left(\frac{3}{2}\cos 2\theta + \cos 4\theta\right) + \frac{3}{2}\frac{a^4}{r^4}\cos 4\theta,$$

$$\sigma_{22}(r,\theta) = -\frac{a^2}{r^2}\left(\frac{1}{2}\cos 2\theta - \cos 4\theta\right) - \frac{3}{2}\frac{a^4}{r^4}\cos 4\theta, \tag{53}$$

$$\sigma_{12}(r,\theta) = -\frac{a^2}{r^2}\left(\frac{1}{2}\sin 2\theta + \sin 4\theta\right) + \frac{3}{2}\frac{a^4}{r^4}\sin 4\theta.$$
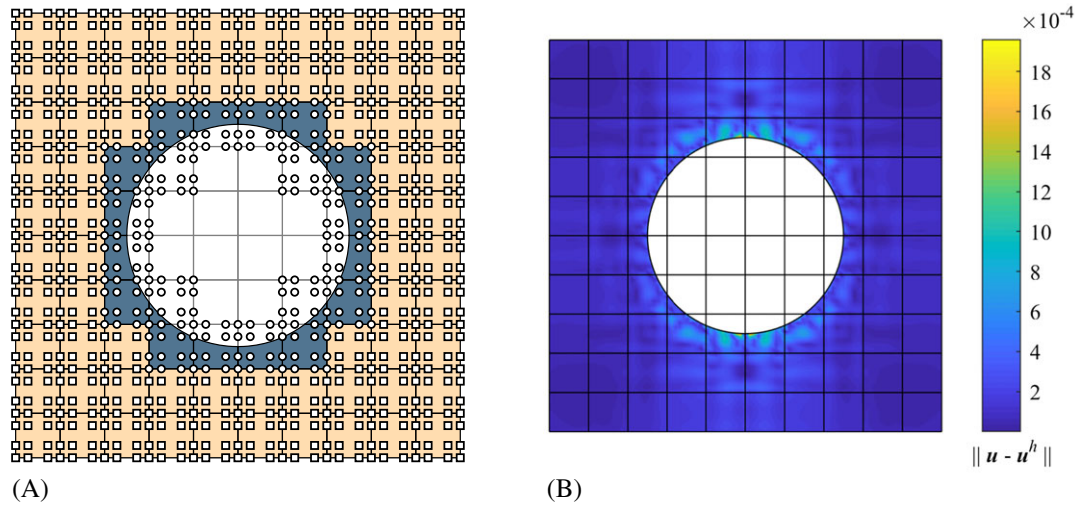
FIGURE 24 Plate with a circular hole problem. (A) 10×10 cubic finite element mesh. Dark shaded (cut) elements use the homogeneous numerical integration scheme to integrate element stiffness matrix. Nodes marked by open squares have entire basis function support whereas those marked by open circles have their basis function support cut by the void, and (B) error in displacement, $e(\boldsymbol{x}) = \|\boldsymbol{u}(x) - \boldsymbol{u}^h(x)\|$, for the mesh in (A)

We model the problem using a finite, biunit plate that occupies the region $\Omega = (-1, 1)^2$. A void, Ω_{hole}, of radius $a = 0.5$ that is centered at the origin is located within Ω. The material constants are $E = 10$ and $\nu = 0.3$, and the exact strain energy in $\Omega \setminus \Omega_{\text{hole}}$ is

$$\mathcal{E}_{\text{SE}} = \frac{13(441068 - 18417\pi)}{24576000},$$

with the value of 0.202706736054886 (15 digits of precision). Cartesian, square elements are used to represent Ω, with the hole modeled using the X-FEM. Traction boundary conditions that are consistent with (53) are applied on the external boundary of the domain. A sample mesh is shown in Figure 24A. This problem is solved using two different methods to represent the boundary Γ_{hole}.

1. Exact representation using rational quadratic Bézier curves.
2. A cubic Hermite curve reconstructed interface using the gradient-augmented level set procedure described in Section 2.2.

Using the exact level set interface avoids the need to reconstruct Γ_{hole}, thereby eliminating a potential source of error caused by inaccurate geometric representation of the void. The Hermite curve reconstruction is done using $\epsilon = 1 \times 10^{-10}$. We observed in numerical experiments that strain energy output is affected by the ghost penalty term at significant digits beyond the exponent of the ghost penalty parameter γ. As a result, rates of convergence degrade when relative error is smaller than γ. Accordingly, we set $\gamma = 1 \times 10^{-10}$, which permits approximately 10 digits of accuracy in the strain energy approximation, while still decreasing the condition number of the stiffness matrix.

Spatial magnitude of displacement error on the mesh shown in Figure 24A is plotted in Figure 24B. As the figure illustrates, displacement error is greater in elements that are cut by the hole. This holds true for the exact hole geometry and the reconstructed hole geometry. To establish the accuracy of the X-FEM with HNI in solving this problem, h- and p-convergence studies are conducted using both methods of representing the circular hole. The results of these studies are presented in Figure 25. Using either the exact hole geometry or a cubic Hermite reconstruction of the hole geometry, optimal $2p$ rates of convergence in strain energy are recovered in h-refinement studies. These rates are obtained using spectral element shape functions of order $p = 1$ to $p = 5$. In p-refinement studies, exponential rates of convergence are obtained using both methods that are used to represent the hole geometry. In the h-refinement studies, matrix condition numbers range from a maximum of $\mathcal{O}(10^5)$ for $p = 1$ to a maximum of $\mathcal{O}(10^{11})$ for $p = 5$. Without ghost penalty and preconditioning, the condition number exceeds $\mathcal{O}(10^{20})$ in some cases. The variation of stiffness matrix conditioning is presented in Figure 26. In Figure 26, results are shown for the exact hole geometry, and in our studies, we obtained similar results when the hole is reconstructed using cubic Hermite curves.
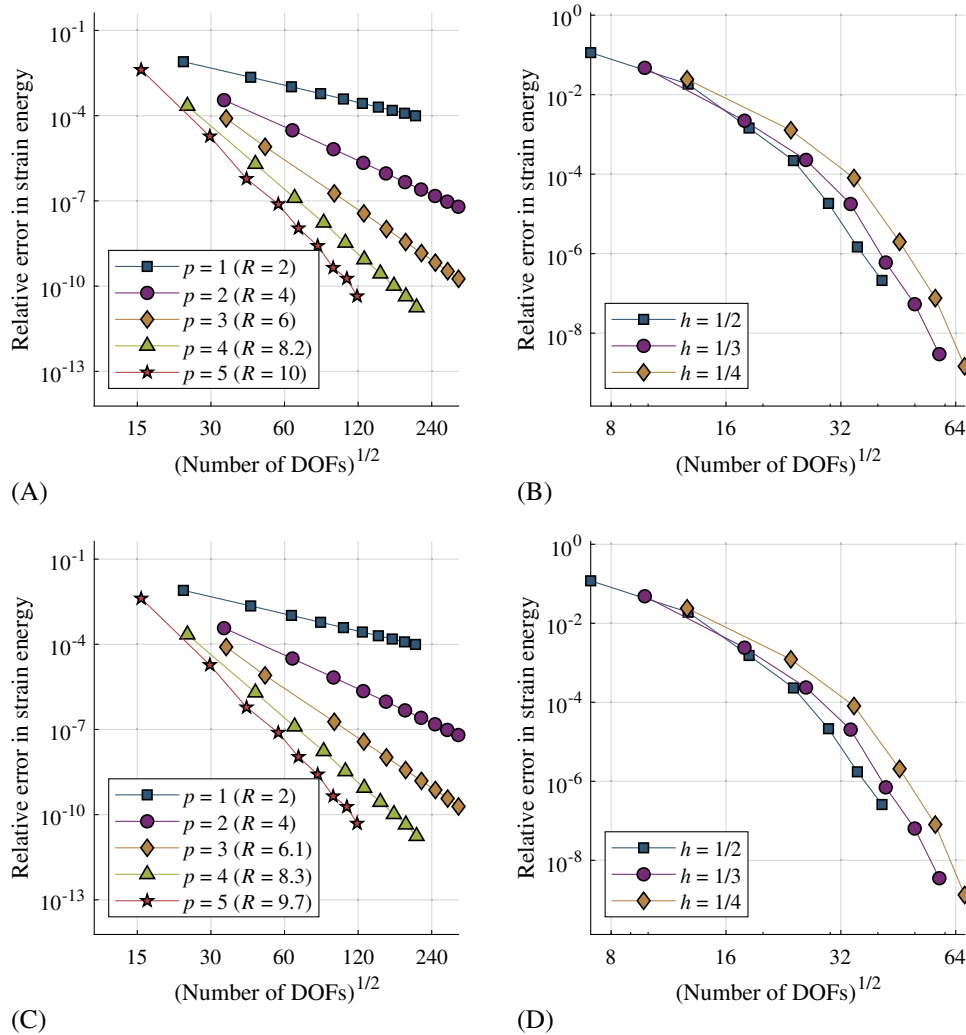
FIGURE 25 Convergence rates in strain energy error for the plate with a circular hole problem. Exact circle geometry: (A) h-refinement and (B) p-refinement ($p = 1, 2 \ldots, 7$). Hermite curve reconstruction of the circle: (C) h-refinement and (D) p-refinement ($p = 1, 2, \ldots, 7$). DOFs, degrees of freedom [Colour figure can be viewed at wileyonlinelibrary.com]

6.3 | Plate with an elliptical hole

Inglis[76] is widely credited as the first to derive the exact elasticity solution for an infinite plate with an elliptical hole under far-field uniaxial tension. This solution has guided some of the earliest results in fracture mechanics, since a sharp crack can be approximated as the limiting case of an ellipse whose aspect ratio approaches zero. Stevenson[77] subsequently realized a simplified solution to the same problem by substituting the Airy (real) potential function with the Kolosov (complex) potential function. This is the solution presented herein. Consider an infinite plate with an elliptical hole that is centered at the origin. The elliptical hole has major axis $2a$ and minor axis $2b$ aligned along the x- and y-directions, respectively. A remote load of magnitude σ_0 is applied at $y = \pm\infty$. A schematic of the boundary-value problem is shown in Figure 27A. The stress field for this problem is determined from[77]

$$\sigma_{11} + \sigma_{22} = \text{Re}[\chi'(z)], \tag{54a}$$

$$\sigma_{11} - \sigma_{22} + 2i\sigma_{12} = -\frac{1}{2}(z\bar{\chi}''(\bar{z}) + \bar{\omega}''(\bar{z})), \tag{54b}$$

where

$$\chi(z) = \sigma_0 c[(1 + e^{2\alpha})\sinh \zeta - e^{2\alpha}\cosh \zeta], \tag{54c}$$

$$\omega(z) = -\sigma_0 c^2 \left[(\cosh 2\alpha + 1)\zeta + \frac{1}{2}e^{2\alpha}\cosh 2(\zeta - \alpha - i\pi) \right], \tag{54d}$$

FIGURE 26 Stiffness matrix condition number for the plate with a hole problem using (A) no stabilization and (B) stabilization using ghost penalty ($\gamma = 1 \times 10^{-10}$ for all analyses) and a Jacobi preconditioner [Colour figure can be viewed at wileyonlinelibrary.com]
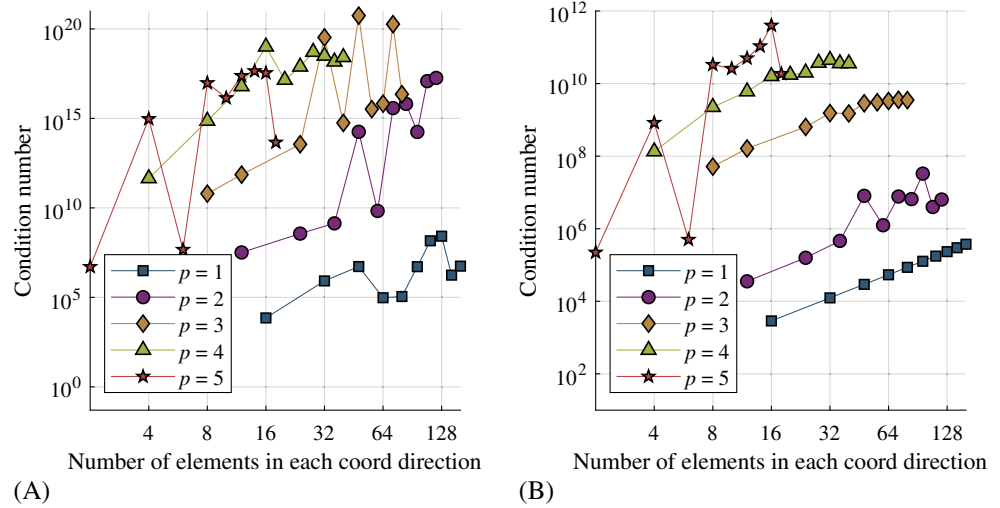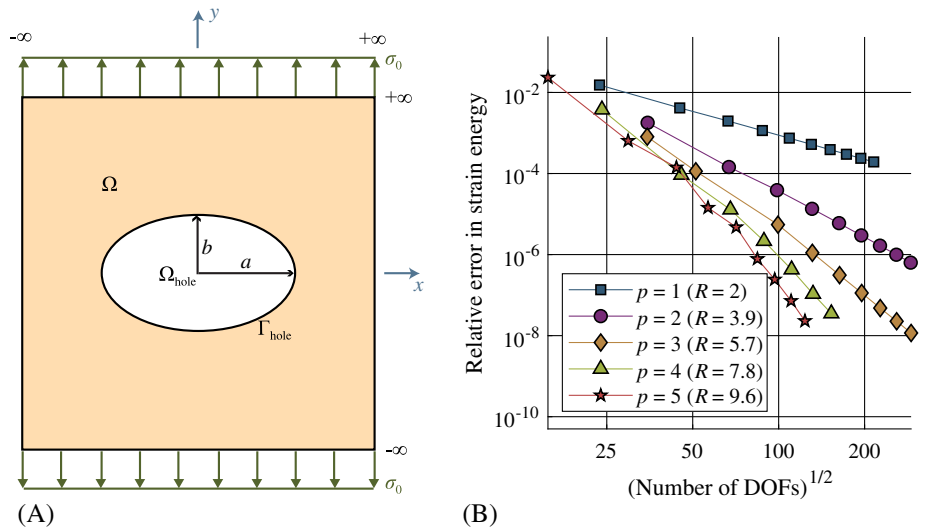

FIGURE 27 Plate with an elliptical hole under far-field uniaxial tension. (A) Schematic of the infinite domain problem, and (B) convergence of strain energy error for the finite plate problem with h-refinement ($p = 1, 2, \ldots, 5$). DOFs, degrees of freedom [Colour figure can be viewed at wileyonlinelibrary.com]

$c = \sqrt{a^2 - b^2}$, $\alpha = \cosh^{-1}(a/c)$, $z = x + iy$, $\zeta = \cosh^{-1}(z/c)$, and a superposed bar denotes the complex conjugate of the indicated complex variable. Computing the complex derivatives in (54) and simplifying, we obtain

$$\frac{\sigma_{11} + \sigma_{22}}{\sigma_0} = \text{Re}\left[\frac{1 + e^{2\alpha}}{\tanh \zeta}\right] - e^{2\alpha}, \tag{55a}$$

$$\frac{\sigma_{11} - \sigma_{22} + 2i\sigma_{12}}{\sigma_0} = \frac{(1 + e^{2\alpha})\cosh\zeta - e^{2\alpha}[\cosh(2\bar{\zeta} - 2\alpha)\sinh\bar{\zeta} + \sinh(2\alpha - \bar{\zeta})] - (1 + \cosh 2\alpha)\cosh\bar{\zeta}}{2\sinh^3\bar{\zeta}}. \tag{55b}$$

Stress components σ_{11} and σ_{22} are computed from the sum and difference, respectively, of (55a) and the real part of (55b). The shear stress component, σ_{12}, is computed from the imaginary part of (55b).

We select the ellipse geometry to be $a = 0.5$ and $b = 0.3$ and solve the elastostatic boundary-value problem over the domain $\Omega = (-1, 1)^2$. The material constants are $E = 1000$ and $\nu = 0.3$, and the applied load is $\sigma_0 = 10$. The exact strain energy (10 digits of precision) is 0.2033773802. In the extended FE computations, the ellipse is modeled exactly using rational Bézier curves. Traction boundary conditions consistent with the exact stress field are applied on the boundary of the domain. The problem is executed at varying levels of mesh refinement for spectral elements of order $p = 1$ to $p = 5$. Convergence of the strain energy error with h-refinement is plotted in Figure 27B. We observe that the asymptotic rates of convergence approach the optimal $2p$ rate predicted by theory. Similar to the circular hole problem in Section 6.2, the results herein are computed using ghost penalty stabilization ($\gamma = 1 \times 10^{-10}$) and Jacobi preconditioning to reduce the condition number of the stiffness matrix.
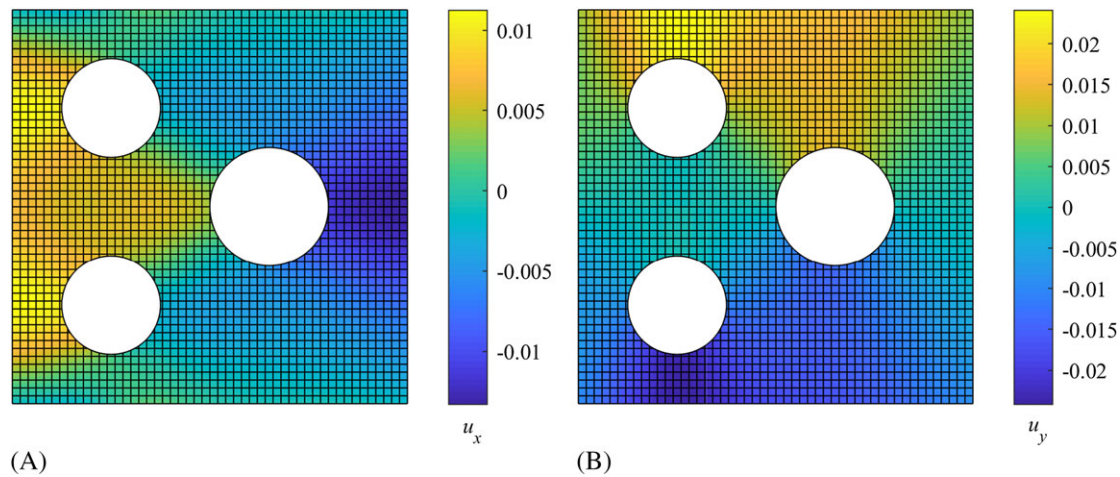
FIGURE 28 Multiple holes described using a single level set function over the domain $\Omega = (-1, 1)^2$. Boundary conditions include uniaxial tension in the y-direction applied at $y = -1$ and $y = 1$. (A) x-displacement field and (B) y-displacement field
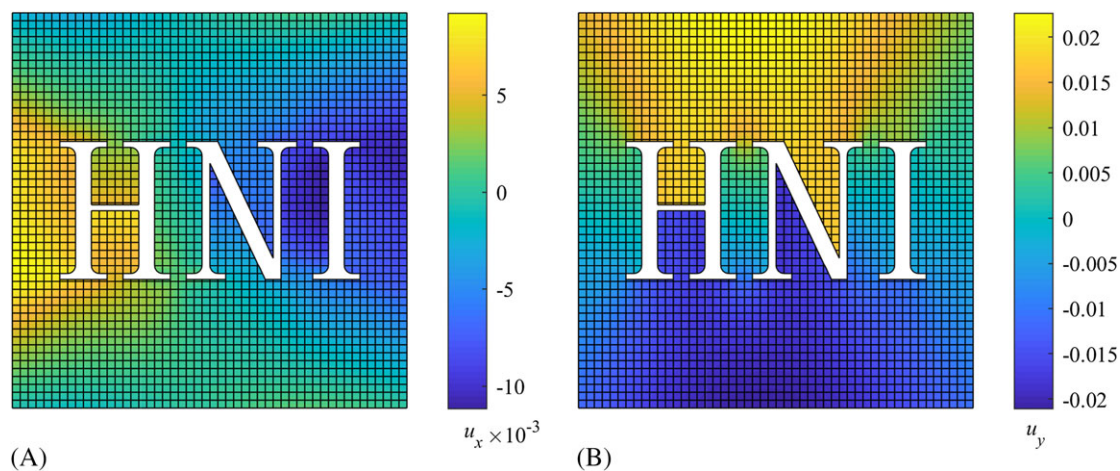

FIGURE 29 Text whose glyphs are defined using quadratic Bézier curves and line segments. Uniaxial tension in the y-direction is applied at $y = -1$ and $y = 1$. (A) x-displacement field and (B) y-displacement field

6.4 | Multiple holes

Using the framework developed in this paper, more complicated problems with multiple voids can be solved. For example, level set functions can define multiple holes, as illustrated in the example in Figure 28. Additionally, multiple Bézier curves can be used to define holes with complicated shapes. For example, glyphs in TrueType™ and OpenType™ fonts are defined using line segments and multiple quadratic and cubic Bézier curves, respectively. The example in Figure 29 demonstrates analysis done on a mesh cut with text whose glyphs are defined using quadratic Bézier curves. The glyphs are represented exactly in the analyses.

6.5 | Bimaterial patch test

Consider a bimaterial linear elastic bar that occupies $\Omega = (0, 1)$, which is composed of two elastic materials with the material interface located at $x = \alpha$. Accordingly, we have $\Omega = \overline{\Omega_1 \cup \Omega_2}$, with $\Omega_1 = (0, \alpha)$ and $\Omega_2 = (\alpha, 1)$. In Ω_1, the material has a Young's modulus of E_1 and the Young's modulus in Ω_2 is E_2. The cross-sectional area of the bar is unity. The bar is fixed at $x = 0$ and is traction-free at the right end. A body force per unit length of magnitude $b(x) = x^m$ ($m \geq 0$)

is applied. The exact solution for the displacement field for this one-dimensional elastostatic boundary-problem is

$$
u(x) = \begin{cases} \frac{1}{E_1(1+m)}\left(x - \frac{x^{2+m}}{2+m}\right) & x \le \alpha \\ \frac{1}{E_2(1+m)}\left(\eta + x - \frac{x^{2+m}}{2+m}\right) & x > \alpha, \end{cases} \tag{56}
$$

where

$$
\eta = \frac{E_2 - E_1}{E_1}\left(\alpha - \frac{\alpha^{2+m}}{2+m}\right).
$$

First, we select $m = 0$, which produces the piecewise quadratic displacement field,

$$
u(x) = \begin{cases} \frac{1}{E_1}\left(x - \frac{x^2}{2}\right) & x \le \alpha \\ \frac{1}{E_2}\left(\eta + x - \frac{x^2}{2}\right) & x > \alpha, \end{cases} \tag{57}
$$

where

$$
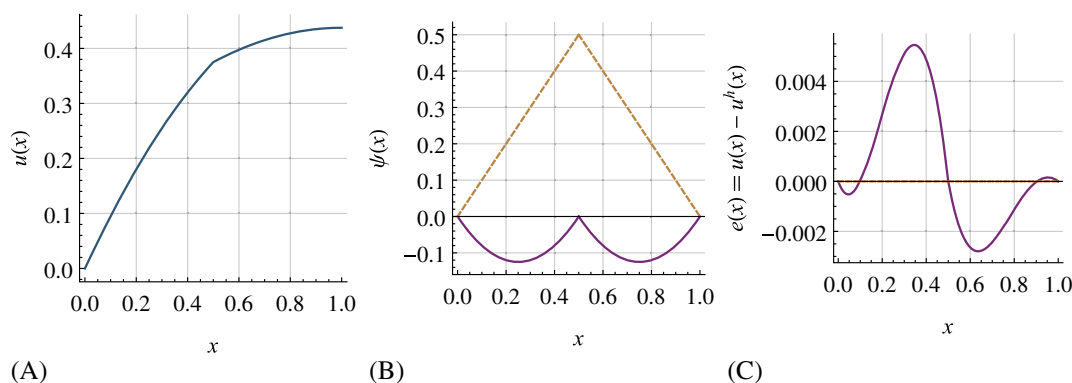\eta = \frac{E_2 - E_1}{E_1}\left(\alpha - \frac{\alpha^2}{2}\right).
$$

FIGURE 30 One-dimensional bimaterial patch test. (A) Exact displacement field from (57). (B) Enrichment functions: modified abs-enrichment is a solid line and the proposed enrichment is a dashed line. (C) Error in the extended finite element displacement field, $e(x) = u(x) - u^h(x)$, using the modified abs-enrichment function. The solution using the proposed enrichment function is exact [Colour figure can be viewed at wileyonlinelibrary.com]
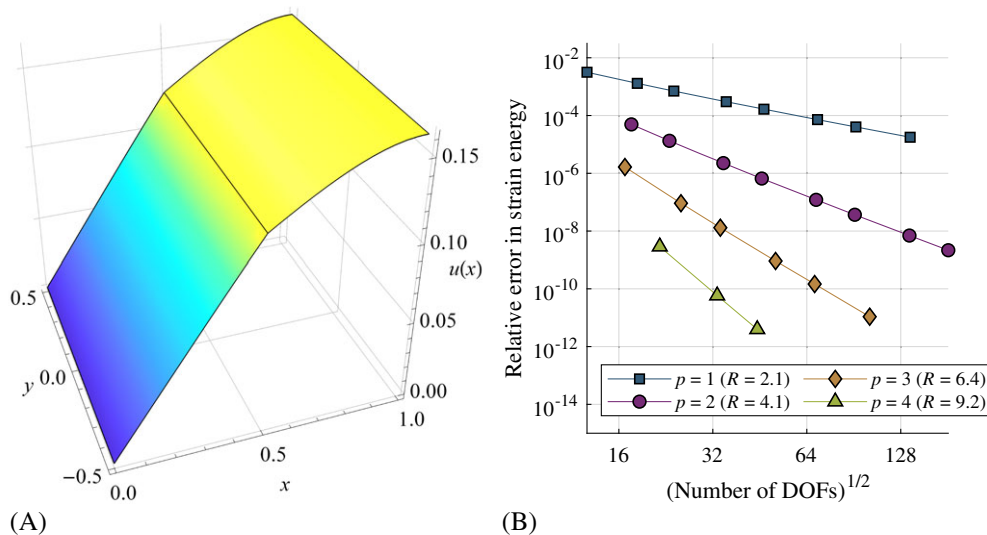
FIGURE 31 Bimaterial boundary-value problem with cubic body force. (A) Exact displacement field from (58), and (B4) h-refinement convergence study in strain energy error using the extended finite element method. DOFs, degrees of freedom [Colour figure can be viewed at wileyonlinelibrary.com]

We choose the quantities $E_1 = 1$, $E_2 = 2$, and $\alpha = 0.5$. The exact displacement field is presented in Figure 30A. For a FE space capable of reproducing two quadratic functions with C^0 continuity, this displacement field should be recovered exactly. With a judiciously chosen interface enrichment function in the X-FEM, it should be possible to construct this space with a single quadratic element. To emphasize the importance of appropriate enrichment, we compare the modified abs-enrichment to the proposed enrichment function (defined in Section 4.3.2). Note the modified abs-enrichment is designed for linear elements—for $p > 1$, the ridge-like shape of this enrichment is not retained. The enrichment functions for this problem are plotted in Figure 30B. Solving the problem using a single quadratic element, we obtain the exact displacement field using the proposed enrichment function. Using the modified abs-enrichment, the exact displacement field cannot be reproduced. These results are depicted in Figure 30C.

Next, we choose $m = 3$, resulting in a piecewise quintic polynomial displacement field

$$u(x) = \begin{cases} \frac{1}{4E_1}\left(x - \frac{x^5}{5}\right) & x \le \alpha \\ \frac{1}{4E_2}\left(\eta + x - \frac{x^5}{5}\right) & x > \alpha, \end{cases} \tag{58}$$

where

$$\eta = \frac{E_2 - E_1}{E_1}\left(\alpha - \frac{\alpha^5}{5}\right).$$

We solve this problem using FEs of order $p = 1$ to $p = 4$ over the two-dimensional domain $\Omega = (0, 1) \times (-0.5, 0.5)$. In Ω, the relevant properties are $E_1 = 1$, $E_2 = 2$, and $\alpha = 0.5$. Since the extended FE space does not span the exact solution, we perform a h-refinement convergence study. In the analyses of this problem, we use the enrichment function proposed
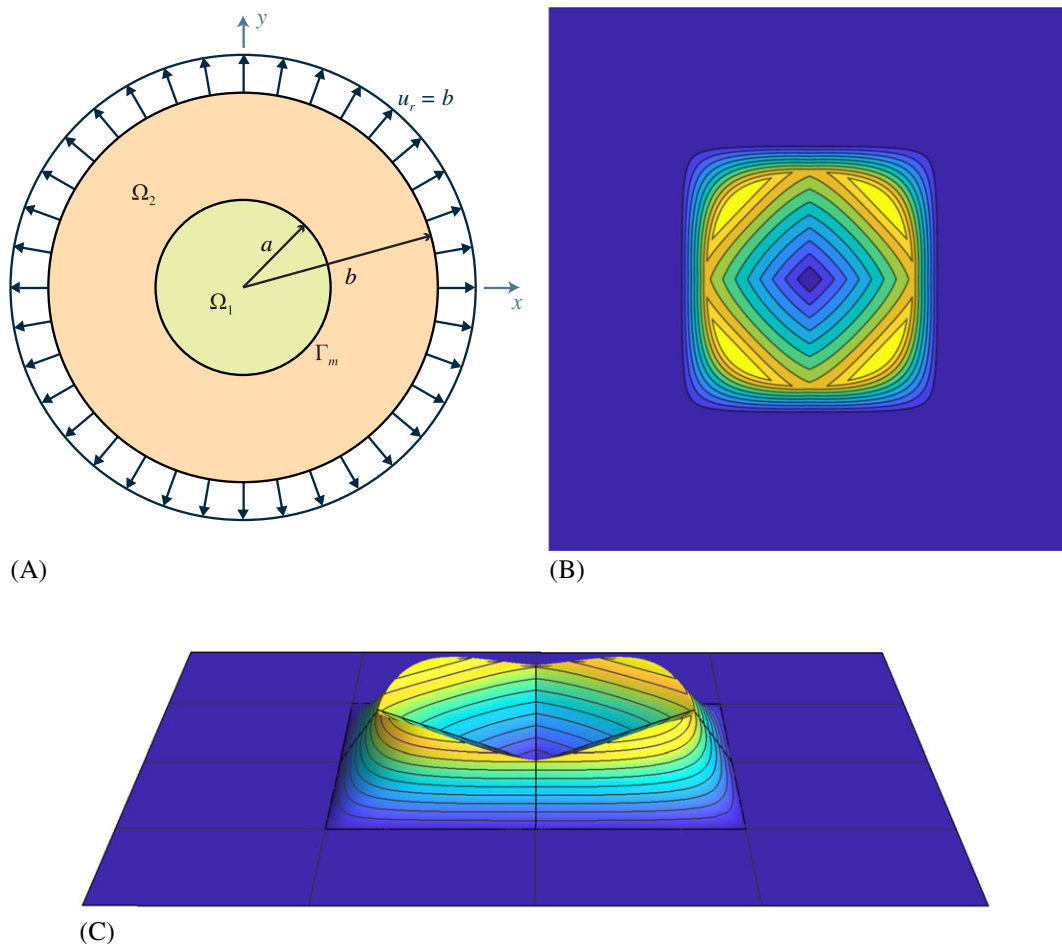

(A)

(B)

(C)

FIGURE 32 Radial displacement boundary conditions for a circular inclusion problem. (A) Schematic, and (B)-(C) bimaterial enrichment function on a 16-element quadratic mesh when $\varphi(\boldsymbol{x})$ is the signed distance function [Colour figure can be viewed at wileyonlinelibrary.com]
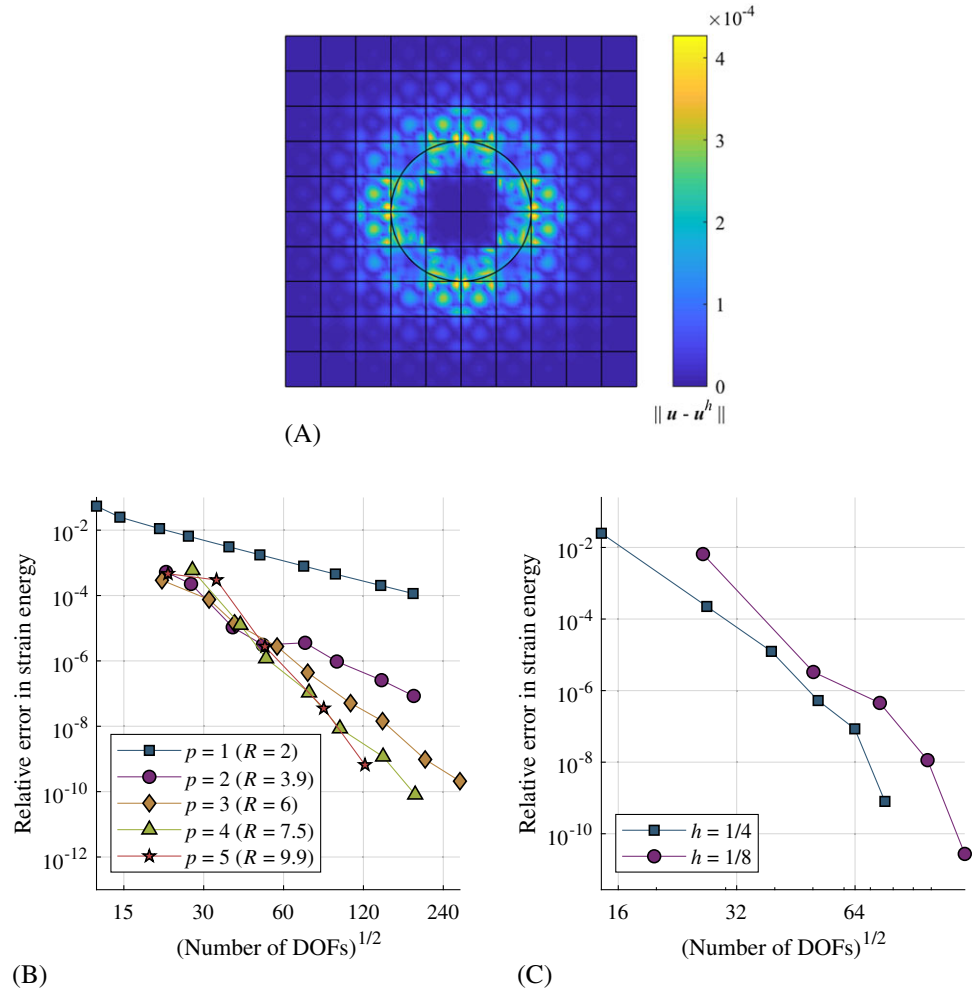
FIGURE 33 Extended finite element solution for the circular inclusion problem. The level set function for the inclusion is the signed distance function. (A) Error in displacement on a 10×10 cubic finite element mesh, (B) relative error in strain energy with h-refinement, and (C) relative error in strain energy with p-refinement ($p = 1, 2, \ldots, 6$ for $h = 1/4$ and $p = 1, 2, \ldots, 5$ for $h = 1/8$. DOFs, degrees of freedom

in (26) and the FE interpolation of nodal values of the level set function to describe the location of the interface. Over the two-dimensional domain, the exact one-dimensional piecewise quintic polynomial displacement field is presented in Figure 31A. For all p, h-refinement studies result in optimal $2p$ rate of convergence in strain energy (see Figure 31B). Condition number is at or below $\mathcal{O}(10^6)$ in all analyses carried out with the Jacobi preconditioner. For the same analysis without preconditioning, condition numbers range from $\mathcal{O}(10^{17})$ to $\mathcal{O}(10^{19})$ in all analyses. However, the strain energy error is identical regardless of whether the preconditioner is used or not.

6.6 | Circular inclusion

In this example, we consider a circular domain, Ω, of radius b composed of two materials and centered at the origin. The domain of the first material, Ω_1, is located in a circular region of radius $a < b$, also centered at the origin. The domain of the second material, Ω_2, makes up the bulk of Ω. The essential boundary condition that is imposed on the outer boundary $r = b$ is a radial displacement of magnitude b. An illustration of the problem is shown in Figure 32A. Due to symmetry, the radial displacement field $u_r(r)$ depends only on r and u_θ is identically zero. This problem was first considered in the work of Sukumar et al,[3] where a solution is also provided. The exact displacement field is

$$u_r(r) = \begin{cases} \left[\left(1 - \frac{b^2}{a^2} \right) \alpha + \frac{b^2}{a^2} \right] r & 0 \leq r \leq a \\ \left(r - \frac{b^2}{r} \right) \alpha + \frac{b^2}{r} & a < r \leq b, \end{cases}$$
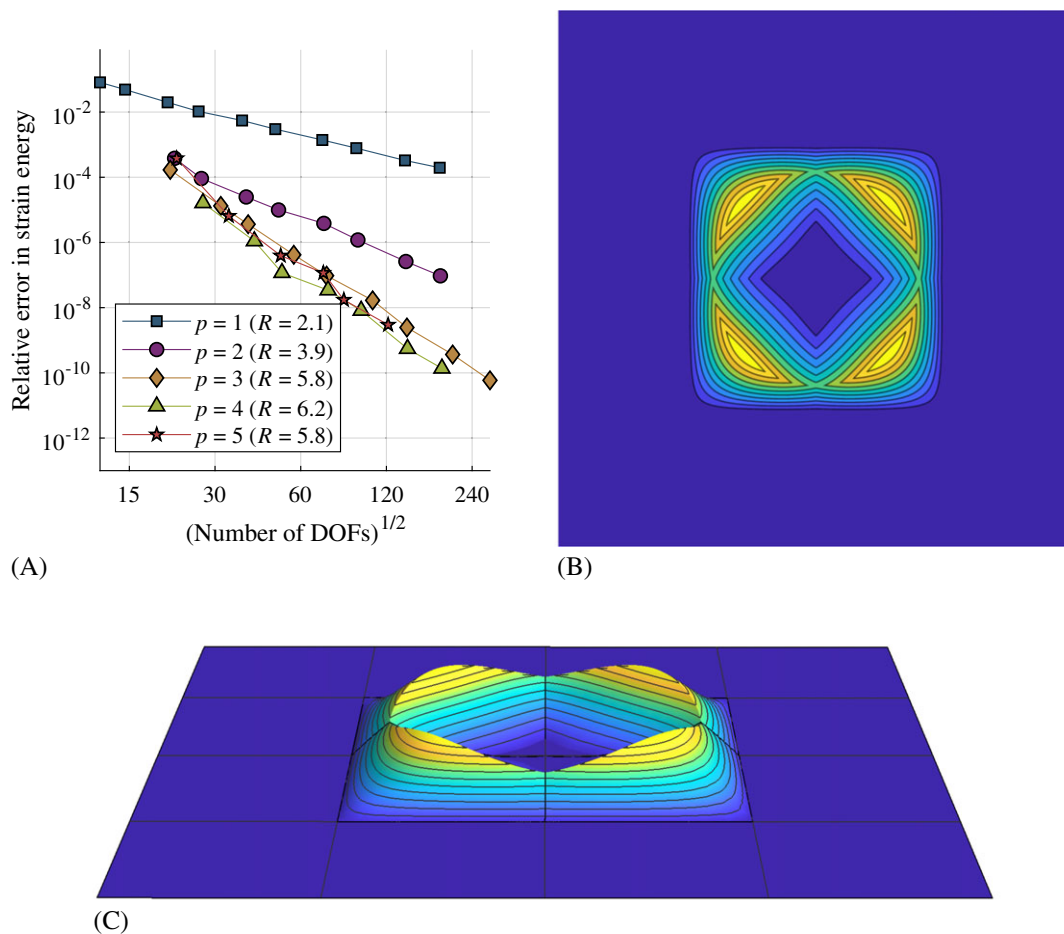
$$u_\theta = 0,$$

(A)

(B)

(C)

FIGURE 34 Extended finite element solution for the circular inclusion problem using a level set function that does not coincide with the distance function. (A) Convergence study of strain energy error with h-refinement. Convergence rates are suboptimal for $p = 4$ and $p = 5$. (B)-(C) Contour and three-dimensional plots of enrichment function on a 4×4 quadratic finite element mesh. DOFs, degrees of freedom [Colour figure can be viewed at wileyonlinelibrary.com]

where

$$\alpha = \frac{(\lambda_1 + \mu_1 + \mu_2)b^2}{(\lambda_2 + \mu_2)a^2 + (\lambda_1 + \mu_1)(b^2 - a^2) + \mu_2 b^2},$$

and λ_1 and μ_1 and λ_2 and μ_2 are the Lamé parameters in Ω_1 and Ω_2, respectively.

This problem is solved with the parameters $E_1 = 1$, $\nu_1 = 0.25$, $E_2 = 10$, $\nu_2 = 0.3$, $a = 0.4$, and $b = 2$ over the domain $\Omega = (-1, 1)^2$. The exact strain energy is

$$\mathcal{E}_{\text{SE}} = \frac{8}{25} \left[(25 - \pi)\alpha^2 \lambda_2 + \pi(25 - 24\alpha)^2(\lambda_1 + \mu_1) + \{25(-4 + 8\alpha - 3\alpha^2) + \pi(625 - 50(\alpha - 1)^2 - 1250\alpha + 624\alpha^2)\}\mu_2 \right],$$

with the value of 74.3856735951026 (15 digits of precision). Exact displacement boundary conditions are applied on $\partial\Omega$. The level set function for this problem is the signed distance function given in (3). This function is recreated through the FE interpolant of its nodal values. The location of the interface is determined through cubic Hermite reconstruction of the level set zero (see Section 2.3). The proposed enrichment function on a 16-element quadratic mesh is illustrated in Figure 32. Evenly spaced isocontours on the plot indicate that the normal derivative of the enrichment function to the interface is nearly a constant.

The displacement error on a 10×10 cubic FE mesh is shown in Figure 33A. As we earlier observed in the circular hole problem, the largest magnitude errors in displacement are concentrated in elements cut by the interface. To assess the capabilities of the X-FEM, the HNI method, and the proposed enrichment function, h- and p-refinement convergence studies in the strain energy error are conducted for this problem. The results of the h-refinement study are presented in Figure 33B. Optimal, or near-optimal $2p$ rates of convergence are obtained using spectral FEs of order $p = 1$ to $p = 5$.

Exponential rates of convergence are obtained in the p-refinement study, as is revealed in Figure 33C. Using a Jacobi preconditioner, the condition number of the stiffness matrix is $\mathcal{O}(10^{10})$ or less in all analyses.

To demonstrate the effect of a level set function that is not the signed distance function, we repeat the analyses with

$$\varphi(\boldsymbol{x}) = \|\boldsymbol{x} - \boldsymbol{x}_c\|^2 - a^2. \tag{59}$$

Similar to the signed distance function in (3), this level set function also exactly defines the location of the material interface; however, it does not coincide with the signed distance function. A consequence is that the enrichment function no longer approximates a smooth ridge function in enriched elements. As established in Section 4.3.3, when the level set function is not a signed distance function, the approximation space no longer includes pth-order polynomials on both sides of the interface. On a 4×4 quadratic FE mesh, the enrichment function is shown in Figure 34. For this enrichment function, the isocontours are not equispaced, and hence, its normal derivative to the interface is not a constant. Error in strain energy with h-refinement is plotted in Figure 34A. Optimal rates of convergence are obtained for $p = 1, 2,$ and 3. However, for $p > 3$, suboptimal rates are recovered. While better asymptotic convergence rates are obtained when the level set function coincides with the signed distance function, notably, sometimes, the error is smaller when using (59), especially on coarse meshes. The reason for this observation becomes apparent upon recognizing that the level set function in (59) is a quadratic polynomial and can therefore be exactly reproduced by the FE basis when $p > 1$. Since this level set function is reproduced exactly by higher-order FEs and the signed distance level set function is not, the error in representing the circle geometry when $p > 1$ is significantly reduced, eliminating a source of error in the analysis results.

7 | CONCLUDING REMARKS

In this paper, we proposed an X-FEM that converges optimally on Cartesian higher-order (spectral) FE meshes for elastostatic problems with curved interfaces. Our focus was on solving the elastostatic boundary-value problems with domains that contained voids (holes) and distinct linear elastic materials (bimaterials). To this end, three important new contributions were realized: improved interface reconstruction techniques using rational Bézier curves and cubic Hermite curves that permitted interface reconstruction to converge to arbitrary order, use of the homogeneous numerical integration (HNI) method for efficient cubature of weak form integrals without the need to partition elements that are cut by curved boundaries, and construction of an enrichment function for material interface problems that accurately captured weak discontinuities on spectral FE meshes. Several examples were presented that demonstrated the capabilities of the method and its ability to recover optimal algebraic and exponential rates of convergence with h- and p-refinement, respectively, for problems with affine and curved interfaces. Even though we only considered Cartesian meshes in this study, we point out that the HNI method is also applicable on higher-order simplicial (Delaunay) meshes with affine facets.

Recent contributions on conformal decomposition methods[31-33] have amply demonstrated the capabilities of a mesh-based approach to solve challenging problems in two dimensions and three dimensions. Nonetheless, the present study provides new pathways for exploration within computational methods on unfitted meshes. The HNI method has several benefits when compared to other competing numerical integration schemes. It reduces integration over a two-dimensional domain to integration over its one-dimensional boundary, thereby avoiding the need for element-partitioning. Since the number of cubature points generally scales with dimension, reducing the dimensionality of the problem can substantially reduce the number of integration points. Reconstructing curved interfaces is also simplified by the HNI scheme, as many different parameterized representations of the curve can be used to build the interface. These parameterizations can be refined arbitrarily and are used directly in the HNI method to provide accurate, robust integration to any desired degree of accuracy. Additionally, complicated intersections of interfaces with an element can be integrated using HNI, since only the boundary of this intersection needs to be reconstructed, rather than the entire domain of integration.

In addition, we introduced an improved enrichment function for use in the X-FEM for material interface problems that accurately captures weak discontinuities. The enrichment function was used for problems in solid mechanics, but it is equally applicable to other phenomena that involve weak discontinuities. While theoretical rates of convergence were obtained using this enrichment function, we anticipate further improvements may be possible through improved selection of DOFs in the enrichment function. For example, DOFs may be chosen to minimize the second derivative of the enrichment function normal to the interface, which may eliminate the need for a relationship between the level set

function and the signed distance function. In addition, forming the enrichment function with Bernstein polynomials may be beneficial, since the Bernstein polynomial basis is nonnegative and possesses the shape-preserving property. Taken together with improvements made possible by the HNI scheme, the new enrichment function provides a way to realize optimal convergence rates for material interface problems on Cartesian higher-order FE meshes.

As part of future work, we can identify several possible topics. Instead of higher-order Lagrange interpolation, use of hierarchical or Bernstein basis functions can potentially deliver additional benefits. On structured meshes, Hermite and B-spline basis functions can be used to solve fourth-order interface problems. Extensions of the approach herein for three-dimensional interface problems on Cartesian meshes (where the HNI scheme remains applicable[78]) and to solve problems with weak discontinuities that arise in two-phase fluid flow, heat conduction, and electrostatics with discontinuous material coefficients are also worthy of pursuit.

ORCID

Eric B. Chin https://orcid.org/0000-0002-0937-2455
N. Sukumar https://orcid.org/0000-0001-6744-7673

REFERENCES

1. Moës N, Dolbow J, Belytschko T. A finite element method for crack growth without remeshing. *Int J Numer Methods Eng*. 1999;46:131-150.
2. Fries T-P, Belytschko T. The extended/generalized finite element method: an overview of the method and its applications. *Int J Numer Methods Eng*. 2010;84:253-304.
3. Sukumar N, Chopp DL, Moës N, Belytschko T. Modeling holes and inclusions by level sets in the extended finite-element method. *Comput Methods Appl Mech Eng*. 2001;190:6183-6200.
4. Osher S, Sethian JA. Fronts propagating with curvature-dependent speed: Algorithms based on Hamilton-Jacobi formulations. *J Comput Phys*. 1988;79(1):12-49.
5. Legay A, Wang HW, Belytschko T. Strong and weak arbitrary discontinuities in spectral finite elements. *Int J Numer Methods Eng*. 2005;64:991-1008.
6. Melenk JM, Babuška I. The partition of unity finite element method: Basic theory and applications. *Comput Methods Appl Mech Eng*. 1996;139:289-314.
7. Chessa J, Wang H, Belytschko T. On the construction of blending elements for local partition of unity enriched finite elements. *Int J Numer Methods Eng*. 2003;57:1015-1038.
8. Fries T-P. A corrected X-FEM approximation without problems in blending elements. *Int J Numer Methods Eng*. 2008;75:503-532.
9. Cheng KW, Fries T-P. Higher-order XFEM for curved strong and weak discontinuities. *Int J Numer Methods Eng*. 2010;82:464-590.
10. Moës N, Cloirec M, Cartraud P, Remacle J-F. A computational approach to handle complex microstructure geometries. *Comput Methods Appl Mech Eng*. 2003;192:3163-3177.
11. Soghrati S, Aragón AM, Duarte CA, Geubelle PH. An interface-enriched generalized fem for problems with discontinuous gradient fields. *Int J Numer Methods Eng*. 2012;89:991-1008.
12. Soghrati S, Duarte CA, Geubelle PH. An adaptive interface-enriched generalized FEM for the treatment of problems with curved interfaces. *Int J Numer Methods Eng*. 2015;102:1352-1370.
13. Dréau K, Chevaugeon N, Moës N. Studied X-FEM enrichment to handle material interfaces with higher order finite element. *Comput Methods Appl Mech Eng*. 2010;199(29-32):1922-1936.
14. Karniadakis GE, Sherwin SJ. *Spectral/hp Element Methods for CFD*. Oxford, UK: Oxford University Press; 1999.
15. Hansbo A, Hansbo P. A finite element method for the simulation of strong and weak discontinuities in solid mechanics. *Comput Methods Appl Mech Eng*. 2004;193(33-35):3523-3540.
16. Burman E, Claus S, Hansbo P, Larson MG, Massing A. CutFEM: Discretizing geometry and partial differential equations. *Int J Numer Methods Eng*. 2015;104(7):472-501.
17. Sticko S, Ludvigsson G, Kreiss G. High order cut finite elements for the elastic wave equation. 2018. https://arxiv.org/abs/1804.00332
18. Düster A, Parvizian J, Yang Z, Rank E. The finite cell method for three-dimensional problems of solid mechanics. *Comput Methods Appl Mech Eng*. 2008;197(45-48):3768-3782.
19. Schillinger D, Düster A, Rank E. The *hp-d*-adaptive finite cell method for geometrically nonlinear problems of solid mechanics. *Int J Numer Methods Eng*. 2012;89:1171-1202.

20. Schillinger D, Ruess M. The finite cell method: a review in the context of higher-order structural analysis of CAD and image-based geometric models. *Arch Comput Methods Eng*. 2015;22(3):391-455.

21. Peskin CS. The immersed boundary method. *Acta Numerica*. 2002;11:479-517.

22. Dettmer WG, Kadapa C, Perić D. A stabilised immersed boundary method on hierarchical b-spline grids. *Comput Methods Appl Mech Eng*. 2016;311:415-437.

23. Glowinski R, Pan T-W, Periaux J. A fictitious domain method for Dirichlet problem and applications. *Comput Methods Appl Mech Eng*. 1994;111:283-303.

24. Burman E, Hansbo P. Fictitious domain finite element methods using cut elements: II. A stabilized Nitsche method. *Appl Numer Math*. 2012;62(4):328-341.

25. Dolbow J, Harari I. An efficient finite element method for embedded interface problems. *Int J Numer Methods Eng*. 2009;78:229-252.

26. Sudhakar Y, Moitinho de Almeida JP, Wall WA. An accurate, robust, and easy-to-implement method for integration over arbitrary polyhedra: application to embedded interface methods. *J Comput Phys*. 2014;273:393-415.

27. Jiang W, Annavarapu C, Dolbow JE, Harari I. A robust Nitsche's formulation for interface problems with spline-based finite elements. *Int J Numer Methods Eng*. 2015;104:676-696.

28. Legrain G, Chevaugeon N, Dréau K. High order X-FEM and levelsets for complex microstructures: uncoupling geometry and approximation. *Comput Methods Appl Mech Eng*. 2012;241-244:172-189.

29. Sala-Lardies E, Fernández-Méndez S, Huerta A. Optimally convergent high-order X-FEM for problems with voids and inclusions. In: Proceedings of the European Congress on Computational Methods in Applied Sciences and Engineering (ECCOMAS 2012); 2012; Vienna, Austria.

30. Noble DR, Newren EP, Lechman JB. A conformal decomposition finite element method for modeling stationary fluid interface problems. *Int J Numer Methods Fluids*. 2010;63:725-742.

31. Lehrenfeld C. High order unfitted finite element methods on level set domains using isoparametric mappings. *Comput Methods Appl Mech Eng*. 2016;300:716-733.

32. Omerović S, Fries T-P. Conformal higher-order remeshing schemes for implicitly defined interface problems. *Int J Numer Methods Eng*. 2017;109:763-789.

33. Roberts SA, Mendoza H, Brunini VE, Noble DR. A verified conformal decomposition finite element method for implicit, many-material geometries. *J Comput Phys*. 2018;375:352-367.

34. Fries T-P. Higher-order conformal decomposition FEM (CDFEM). *Comput Methods Appl Mech Eng*. 2018;328:75-98.

35. Lew AJ, Buscaglia GC. A discontinuous-Galerkin-based immersed boundary method. *Int J Numer Methods Eng*. 2008;76(4):427-454.

36. Gracie R, Wang H, Belytschko T. Blending in the extended finite element method by discontinuous Galerkin and assumed strain methods. *Int J Numer Methods Eng*. 2008;74:1645-1669.

37. Sukumar N, Dolbow JE, Moës N. Extended finite element method in computational fracture mechanics: a retrospective examination. *Int J Fract*. 2015;196:189-206.

38. Ciarlet PG, Raviart P-A. Interpolation theory over curved elements, with applications to finite element methods. *Comput Methods Appl Mech Eng*. 1972;1:217-249.

39. Müller B, Kummer F, Oberlack M. Highly accurate surface and volume integration on implicit domains by means of moment-fitting. *Int J Numer Methods Eng*. 2013;96:512-528.

40. Sudhakar Y, Wall WA. Quadrature schemes for arbitrary convex/concave volumes and integration of weak form in enriched partition of unity methods. *Comput Methods Appl Mech Eng*. 2013;258:39-54.

41. Min C, Gibou F. Geometric integration over irregular domains with application to level-set methods. *J Comput Phys*. 2007;226:1432-1443.

42. Haasemann G, Kästner M, Prüger S, Ulbricht V. Development of a quadratic finite element formulation based on the XFEM and NURBS. *Int J Numer Methods Eng*. 2011;86:598-617.

43. Fries T-P, Omerović S. Higher-order accurate integration of implicit geometries. *Int J Numer Methods Eng*. 2016;106(5):323-371.

44. Fries T-P, Omerović S, Schöllhammer D, Steidl J. Higher-order meshing of implicit geometries—part I: integration and interpolation in cut elements. *Comput Methods Appl Mech Eng*. 2017;313:759-784.

45. Saye RI. High-order quadrature methods for implicitly defined surfaces and volumes in hyperrectangles. *SIAM J Sci Comput*. 2015;37(2):A993-A1019.

46. Fried I. Accuracy and condition of curved (isoparametric) finite elements. *J Sound Vib*. 1973;31(3):345-355.

47. Zienkiewicz OC, Taylor RL. *The finite Element Method: The Basis*. Vol. 1. 5th ed. Oxford, UK: Butterworth Heinemann; 2000.

48. Sevilla R, Fernández-Méndez S, Huerta A. Comparison of high-order curved finite elements. *Int J Numer Methods Eng*. 2011;87:719-734.

49. Sevilla R, Fernández-Méndez S, Huerta A. NURBS-enhanced finite element method (NEFEM). *Arch Comput Methods Eng*. 2011;18:441-484.

50. Chin EB, Lasserre JB, Sukumar N. Numerical integration of homogeneous functions on convex and nonconvex polygons and polyhedra. *Comput Mech*. 2015;56(6):967-981.

51. Chin EB, Lasserre JB, Sukumar N. Modeling crack discontinuities without element-partitioning in the extended finite element method. *Int J Numer Methods Eng*. 2017;110(11):1021-1048.

52. Burman E. Ghost penalty. *Comptes Rendus Math*. 2010;348(21-22):1217-1220.

53. Beirão da Veiga L, Russo A, Vacca G. The virtual element method with curved edges. *ESAIM Math Model Numer Anal*. 2019;53:375-404.

54. Laursen TA, Puso MA, Sanders J. Mortar contact formulations for deformable-deformable contact: past contributions and new extensions for enriched and embedded interface formulations. *Comput Methods Appl Mech Eng*. 2012;205-208:3-15.

55. Hughes TJR, Cottrell JA, Bazilevs Y. Isogeometric analysis: CAD, finite elements, NURBS, exact geometry and mesh refinement. *Comput Methods Appl Mech Eng*. 2005;194(39-41):4135-4195.

56. Nave J-C, Rosales RR, Seibold B. A gradient-augmented level set method with an optimally local, coherent advection scheme. *J Comput Phys*. 2010;229(10):3802-3827.

57. Farin GE. *Curves and Surfaces For Computer-Aided Geometric Design: A Practical Guide*. 4th ed. New York, NY: Academic Press; 1996.

58. Cox D, Little J, O'Shea D. *Ideals, Varieties, and Algorithms*. New York, NY: Springer; 2007.

59. Sederberg TW, Chen F. Implicitization using moving curves and surfaces. In: Cook R, ed. *Proceedings of the 22nd Annual Conference on Computer Graphics and Interactive Techniques SIGGRAPH '95*. New York, NY: ACM; 1995:301-308.

60. Sederberg T, Goldman R, Du H. Implicitizing rational curves by the method of moving algebraic curves. *J Symb Comput*. 1997;23:153-175.

61. Benowitz BA, Waisman H. A spline-based enrichment function for arbitrary inclusions in extended finite element method with applications to finite deformations. *Int J Numer Methods Eng*. 2013;95:361-386.

62. Farouki RT. *Pythagorean-Hodograph Curves: Algebra and Geometry Inseparable*. Berlin, Germany: Springer; 2008.

63. de Boor C. *A Practical Guide to Splines*. Berlin, Germany: Springer; 1978.

64. Dokken T. Approximate implicitization. In: Lyche T, Schumaker LL, eds. *Mathematical Methods for Curves and Surfaces: Oslo 2000*. Nashville, TN: Vanderbilt University; 2001:81-102.

65. Jüttler Bert, Chalmovianský P. Approximate parameterization by planar rational curves. In: Proceedings of the 20th Spring Conference on Computer Graphics; 2004; Budmerice, Slovakia.

66. Rosenbrock HH. An automatic method for finding the greatest or least value of a function. *Comput J*. 1960;3(3):175-184.

67. Saye RI. High-order methods for computing distances to implicitly defined surfaces. *Comm App Math Comp Sci*. 2014;9(1):107-142.

68. Lasserre JB. Integration on a convex polytope. *Proc Am Math Soc*. 1998;126(8):2433-2441.

69. Daux C, Moës N, Dolbow J, Sukumar N, Belytschko T. Arbitrary branched and intersecting cracks with the extended finite element method. *Int J Numer Methods Eng*. 2000;48(12):1741-1760.

70. Babuska I, Banerjee U, Kergrene K. Strongly stable generalized finite element method: Application to interface problems. *Comput Methods Appl Mech Eng*. 2017;327:58-92.

71. de Prenter F, Verhoosel CV, van Zwieten GJ, van Brummelen EH. Condition number analysis and preconditioning of the finite cell method. *Comput Methods Appl Mech Eng*. 2017;316:297-327.

72. Lehrenfeld C, Reusken A. Optimal preconditioners for Nitsche-XFEM discretizations of interface problems. *Numerische Mathematik*. 2017;135(2):313-332.

73. Stone BJ. Best possible ratios of certain matrix norms. *Numerische Mathematik*. 1962;4:114-116.

74. Hager WW. Condition estimates. *SIAM J Sci Stat Comput*. 1984;5(2):311-316.

75. Szabó B, Babuska I. *Finite Element Analysis*. New York, NY: Wiley; 1991.

76. Inglis CE. Stresses in a plate due to the presence of cracks and sharp corners. *Trans Inst Nav Archit*. 1913;55:219-241.

77. Stevenson AC. Complex potentials in two-dimensional elasticity. *Proc R Soc Lond A Math Phys Sci*. 1945;184(997):129-179.

78. Liu C, Prévost JH, Sukumar N. Modeling piecewise planar fault discontinuities without element-partitioning in 3D reservoir-geomechanical models. *Int J Numer Anal Methods Geomech*. 2019;43(2):530-543.